CAVITATION ASSOCIATED LOW-FREQUENCY FLUCTUATION

by

Shengcai Li

Self-guided Research Thesis

submitted to

Department of Engineering, University of Warwick, U. K.

for

Degree of Doctor of Philosophy

February 1990

SUMMARY

This self-guided thesis presents the research results of the *Cavitation Associated Low-frequency Fluctuation*, i. e. one part of the long-term research project on *Statistical Characteristics of Cavitation Bubble Collapse Pulses, Associated Low-frequency Fluctuations and Flow Noise* which was initiated and carried out by the author in USA, China and UK successively over last 9 years.

The background and the objectives of the long-term project is introduced in the thesis through a broad review of the development of the cavitation research in the fields relevant to the project.

Then, the observed phenomenon of Cavitation Associated Low-frequency Fluctuation in the venturi cavitating flow of the University of Michigan (USA) is explained in detail.

A one-dimensional linear physical model based on the theorem of the interaction between the cavitation cloud of the homogeneous liquid-vapour/gas mixture and the surrounding liquid portion in the flow system is proposed to describe the mechanism of the phenomenon. The appearance of this low-frequency fluctuation is an association nature of the cavitating flow, which could be regarded as an alternatively indirect indicator of cavitation inception especially in such sort of cavitating flow systems. When the natural frequencies for both the cavitation cloud and the surrounding liquid portion coincide, the low-frequency pressure fluctuation component reaches its maximum, which is defined as *Cavitation Resonance*. A numerical verification of the frequency response characteristics, using the hydraulic impedance approach, of this venturi system is presented as well.

The knowledge of the cavitation associated low-frequency fluctuation acquired from the study of the venturi cavitating flow has been used to analyze the phenomenon of the pressure fluctuations associated with the cavitating flows in the hydraulic machinery systems such as the HL-160-25 (Francis) Hydraulic Turbine System (draft-tube cavitating flow). The results are also briefly presented.

PREFACE

The cavitation phenomenon involved in hydraulic machinery has been strongly holding the author's interest. In 1960's, the author as an university student at Peking Institute of Water Resources (China) started the research on the cavitation problem of hydraulic turbine which was a specially arranged 3-year research project. It included: the investigation into the possible approach for the improvement of the machine's cavitation performance; the theoretical analysis (using the approach of successively conformable transformation), the experimental simulation (by means of the hydro-electric simulate) and the numerical verification of the double-raw cascade flows. As the result, a runner structure of double-row cascade (i.e. flap structure) was proposed by the author to improve the cavitation performance of hydraulic turbines/pumps. The above work formed author's Graduation Thesis (1964, PhD equivalent; but without the title of PhD due to the absence of the degree structure within China at that time). Later on, the concept of using flap structure to improve cavitation performance has been proved by the model test on a axial flow pump in early 1980's and by the Norwegian (Kvaerner Brug A/S) made Francis turbines (unit capacity 150 MW) for the Lubuge Power Station (China) in late 1980's.

No matter how much effort has been put into the improvement of the cavitation performance of the machines for avoiding the occurrence of cavitation, the cavitation still occurs very often in hydraulic machinery due to various causes such as the off-optimum operations, minor errors of design/manufacture/repair or some special purposes/requirements (e.g. the cavitation performance/erosion tests on model/prototype machines). The cavitation and its effects seem to be unavoidable in the hydraulic machinery. Therefore, the investigation of the characteristics of cavitation/cavitating flows must be put in the same important position as the research work for avoiding their occurrence. But due to the complexity of the phenomenon, cavitation is still not well understood despite about 100 years of research. Usually, the cavitation phenomenon has following features.

1) It is a collective behaviour of the all bubbles involved.

2) It often occurs under a dynamic flow conditions, i. e. the ambient flow conditions (velocity, preasure and their gradients/variations) would have strong influences on the behaviour of cavitation, and vice versa. Therefore, there must be some sort of interaction existing between the cavitation region (or cavitation cloud) and the surrounding liquid portion.

3) It is a highly stochastic behaviour even under very carefully controlled conditions.

An investigation of the cavitation behaviour taking into account the above features through some suitable approach would make a significant improvement of our knowledge of cavitation phenomenon. Having realized this fact, in 1981, the author as a Visiting Scientist working at the Cavitation and Multiphase Flow Laboratory (University of Michigan, USA) initiated the long-term research project *Statistical Characteristics of Cavitation Bubble Collapse Pulses, Associated Low-frequency Fluctuations and Flow Noise*. After the two year research, this project has been continued in the Hydraulic Machinery Laboratory (North China Institute of Water Conservancy and Power, China) of which I am in charge.

Since 1989, I have been invited as a SERC (Science and Engineering Research Council, U. K.) Principal Research Fellow to help set up cavitation research, which closely follows my above long-term research work, at the Department of Engineering (University of Warwick, U.K.). Meanwhile, considering the need for an official title of PhD in my international activities, I decided to take the opportunity of being at the Department to write part of my previous findings of the long-term project in PhD thesis form (by self guidance) for obtaining the PhD title. My above request was kindly understood and approved by the University Higher Degree Committee, and the special arrangement was thus offered accordingly. This self-guided thesis titled *Cavitation Associated Low-frequency Fluctuation* is thus submitted for the Degree of Doctor of Philosophy. Therefore, I would like to express my special thanks to the Department and the University for their understanding and the special arrangement.

Li, Shengcai
Professor of Hydraulic Machinery
Coventry, United Kingdom, Feb., 1990

Table of Contents

ACKNOWLEDGMENT

The work presented in this thesis is part of the author's long-term research project on *Statistical Characteristics of Cavitation Bubble Collapse Pulses, Associated Low-frequency Fluctuations and Flow Noise*. This long-term project has been carried out subsequently in the University of Michigan (USA), the North China Institute of Water Conservancy and Power (China), and the University of Warwick (UK) under following research funds:

National Science Foundation Grant No. ENG 75-2315 (USA)

Internal University of Michigan Funds (USA)

National Research Grant No. 87022190 of Water and Power (China)

Internal Research fund, Department of Power Engineering, North China Institute of Water Conservancy and Power (China)

SERC Principal Research Fellowship Grant (UK)

Civil Engineering Research Fund, Dept. of Engineering, University of Warwick (UK)

I would like to give my deepest thanks to all the parties above for their significantly financial supports; and also to express my sincere thanks to:

My Chinese colleagues, Mr. D. X. Chen, Mr. J. Z. Bai, Mr. H. F. Zhou, Mr. Z. C. Pan and Mr. Z. Y. Pei of the Hydraulic Machinery Lab (NCIWCP, China), for their assistance in exercising the cavitation test on HL-160-25 model runner;

My British colleague, Dr. A. P. Boldy of the Engineering Department (University of Warwick, U.K.), for polishing the English language of the final version of the thesis.

The figures mostly in the chapter of Introduction have come from a variety of sources. In each case the acknowledgment appears as a parenthetical reference keyed by

the name(s) of the original author(s) in the figure caption. Those which originate directly from my previous project and technical reports are not so referenced.

DECLARATION

I declare that:

A. This thesis presents one part of the results from my own long-term research project on *Statistical Characteristics of Cavitation Bubble Collapse Pulses, Associated Low-frequency Fluctuations and Flow Noise* which was initiated by me in 1981 and thenceforth has been carried out by me over last 9 years. Although at one time some others as the co-operators joined the long-term project, I as the chief investigator throughout the course of the research have set up the objectives of the research; guided its direction and determined the methods adopted in the research; undertaken the major job of the actual research work such as the design of the experiment, conducting the experiment, programming and computation, and writing the publications.

B. The work presented in the thesis, i.e. the mechanism proposed for the phenomenon of cavitation associated low-frequency fluctuations and its application to the study of cavitating flows in the hydraulic machinery systems, was originally developed from my own idea and achieved by me as the chief investigator and the other co-operators; and these results have been incorporated in several publications, of which I am the first author, such as *Statistical Characteristics of Cavitation Bubble Collapse Pulses, Associated Low-frequency Fluctuations and Flow Noise* (J. Hyd. Research, Vol.24, 1986, No.2) and *Statistical Considerations on Pressure Pulses from a Cavitating Venturi* (Proc. Instn. Mech. Engrs. Vol.200, No.C6).

C. This thesis submitted for the degree of Doctor of Philosophy is accomplished entirely by my own self-guidance without any supervision from any body. The work presented in it has never been submitted previously in support for an application for any degree or qualification in any other academic institution.

NOMENCLATURE

A = cross-section area of conduit

A_{throat} = cross-section area of throat

$\bar{a}$ = average amplitude over the frequency range of the spectrum

a_f = amplitude of the fluctuation

a_v = guide vane opening

b_v = height of guide vane

$\bar{b}_v$ = relative height of guide vane

C = capacitance of the liquid in the pipe; capacitance of cavity

C_Q = velocity distribution coefficient

C_r = correction coefficient for circulation evaluation

C_v = volumetric coefficient

C' = cavity compliance

$c; c_l$ = sound speed in liquid/water

c_∞ = sound speed at infinity

D = diameter of conduit

D_1 = diameter of turbine runner

D_c = diameter of cavitated vortex rope

D_g = thermal diffusivity in gas

D_l = thermal diffusivity in liquid

d_c = small perturbation of the diameter D_c of the cavitated vortex rope

E = expectation of statistical distribution; elastic modulus

E_∞ = acoustic energy emitted from a simple acoustic sphere

$E_{collapse}$ = acoustic energy emitted during bubble collapse

E_{growth} = acoustic energy emitted during bubble growth

E_{pot} = total potential energy of a collapsing bubble

ε = volume dilation, $\varepsilon=\varepsilon_1+\varepsilon_2+\varepsilon_3$; thickness of conduit wall

$\vec{F}$ = vector of mass force

$F(\omega)$ = power spectrum of random pulse train

$F_{av}(\omega)$ = power spectrum for the bubbles with the average radius

F_1, F_2, F_3 = frequency bands of the fluctuations in the draft tube of the HL-160-25 turbine

F_f = characteristic frequency of the low-frequency fluctuation

f = Darcy-Weisbach factor

f_{bubble} = natural frequency of air bubble

f_{cav} = first harmonic frequency of cavitation cloud

f_f = fluctuation frequency

f_{hq} = first harmonic frequency of the series pipeline

f_{max} = maximum frequency of the harmonic components

f_s = sampling frequency

G_1 = dimensionless driving frequency

G_2 = dimensionless parameter in respect of thermal diffusivity in gas

$g(\omega z)$ = complex spectrum (Fourier Transform) of the function describing the waveform of the n th pulse

H = hydraulic head

$\overline{H}$ = equilibrium hydraulic head

H_a = atmosphere pressure at the site (in terms of hydraulic head)

$\overline{H}_o$ = head drop across the orifice for mean flow rate

H_s = suction head of turbine

H_v = vapour pressure in terms of hydraulic head

HB = Brinell hardness

h' = small oscillation of hydraulic head

I_{cav} = power of cavitation pulses

I_{ero} = power operative in the erosion process

IP = incubation period

K = complex quantity describing the all thermal effects associated with the small-amplitude gas-bubble oscillations

K_e = equivalent bulk modulus of the elasticity of the liquid in the container

K_l = elasticity modulus of liquid

k = polytropic exponent; coefficient characterizing the linear relation between the amplitude ε_n and the time parameter τ_n of n th pulse

L = latent heat of evaporation; inertance of the liquid in the pipe

L_{cav} = cavitation cloud length

L_n = n th pipe length

M = molecular weight of gas; Mach number

M_{max} = maximum of Mach number

$MDPR$ = mean depth of penetration rate

$MDPR_{max}$ = maximum mean depth of penetration rate

m = number of pipes in series

N = number of sampling points

n'_1 = unit speed of turbine

n_s = specific speed of turbine

P = pressure

PM = the slope of the pump characteristic curve at the operating point

p = pressure

p_c = cut-off pressure

p_g = gas pressure

$p_{g,max}$ = maximum of gas pressure

p_i = internal pressure of bubble

$p_{i,eq}$ = equivalent internal pressure of bubble

p_m = amplitude of collapse pulse

p_{max} = maximum value of pressure p

p_{min} = minimum throat pressure

p_r = reference pressure

p_v = vapour pressure

$p(R)$ = the pressure at the wall of the bubble

p_∞ = the pressure at infinity

Q = initial partial pressure of gas content in the bubble; flow rate

$\overline{Q}$ = equilibrium flow rate

Q'_1 = unit discharge of turbine

Q_o = zero-swirling discharge rate

q' = small oscillation of flow rate

R = radius of cavity/bubble; linearized resistance per unit length of pipe; radius of the straight part of the draft tube

$R_{e,j}$ = Reynolds number at the venturi throat

R_g = universal gas constant

R_i = initial radius from which bubble starts collapsing

R_{max} = maximum value of radius

R_{min} = minimum value of radius

R_o = initial radius of bubble

r = radial distance

S – wave speed in the liquid considering the properties of the conduit wall

S_{cm} = sound speed in cavitation cloud (liquid-vapour/gas mixture)

S_g = sound speed in liquid-gas mixture

s = complex frequency

s_i = initial value of complex frequency s

Δs = correction to the complex frequency s

T = temperature; dominant time interval; time interval between successive sampling points

$T_{g,max}$ = maximum of gas temperature

T_o = initial gas temperature

TS = ultimate tensile strength

T_∞ = absolute temperature at infinite

TM = the slope of turbine H-Q performance curve at the operating point

$\overline{\Delta T}$ = average time interval

t = time

t_n = time at which the n th stochastic event appears

U = the radical component of the velocity of the bubble wall

u – radical component of velocity

V = wall-velocity of bubble

V_{cav} = cavity volume

$\bar{V}$ = mean value of the liquid in the container

V_{throat} = throat velocity

v = velocity vector

$W_\tau(x)$ = differential distribution function of the time parameter τ

$W_\mu(t), W_\mu(x), W(\mu)$ = statistical distribution function of the time intervals

W_I = statistical distribution of the amplitude density

$W_M(X)$ = statistical distribution of the required times for completing M number of collapsing bubbles

Z = hydraulic impedance

Z_c = characteristic impedance

z = relative volume of bubble, $z=(\frac{R}{R_0})^3$; axial coordinate of draft tube

α = void fraction

β = relative radius of bubble, $\beta=\frac{R}{R_0}$; damping constant; empirical exponent in respect of the acoustic energy emitted from collapsing bubble; diffusive angle of draft tube

$\beta_{acoustic}$ = acoustic component of damping constant

$\beta_{thermal}$ = thermal component of damping constant

$\beta_{viscous}$ = viscous component of damping constant

Γ = circulation of vortex rope

γ = adiabatic exponent; propagation constant

δx = step length of frequency scan

ε = small dimensionless amplitude of perturbation

$\varepsilon_1, \varepsilon_2, \varepsilon_3$ = principal normal strains

η = dimensionless pressure amplitude used for the model of the nonlinear gas-bubble oscillations

η_e = cavitation erosion efficiency

η_o = hydraulic efficiency of hydraulic turbine at zero-swirling operating condition

Θ_n = characteristic function of the stochastic variable of time interval between two successive pulses

λ_g = wave length of sound in gas

μ = dynamic viscosity

μ_{th} = effective " thermal " viscosity

ν_n = random variable with mean value of zero, describing the stochastic feature of event occurrences

ρ = water density

ρ_{cav} = density of cavitation cloud

ρ_g = gas density

ρ_l = liquid density

ρ_{mix} = mixture density

$\rho_{v,eq}(T)$ = equilibrium vapour density at temperature T

ρ_∞ = density at infinity

σ = surface tension; square root of variance; cavitation number

σ_c = cavitation number

σ_{in} = cavitation number for inception

σ_p = installation cavitation number of turbine

τ = time for a complete collapse; time constant of collapse pulse

τ_w = shear stress

Φ = velocity potential

$\Delta\phi$ = small perturbation of velocity potential

ϕ_{vol} = additional velocity potential caused by the volumetric variation of the cavitated vortex rope

ω = angular frequency

ω_m = angular frequency of mth harmonic

ω_n = natural frequency of bubble; rated angular speed of turbine

ω_{sp} = angular frequency of the " Synchronous Pressure Excitation " (i.e. rotation of vortex rope)

LIST OF FIGURES AND TABLES

CHAPTER 1

CHAPTER 2

CHAPTER 3

1. INTRODUCTION

This chapter is organized as follows. The discovery of cavitation phenomenon and its research development, especially the major achievements contributing to the basic knowledge of cavitation (such as the bubble dynamics) and relevant to the author's research on the long-term project *Statistical Characteristics of Cavitation Bubble Collapse Pulses, Associated Low-frequency Fluctuations and Flow Noise* (such as the acoustic emission of single bubble collapse, acoustic emission of cavitation multi-bubble collapses etc.), are reviewed.

The reasons are apparent. Firstly, the topic of *Cavitation Associated Low-frequency Fluctuations* is only one part of the results from the long term project. Secondly, the objective of the long-term project is to view the cavitation as the stochastic multi-bubble behaviour considering the mutual influences between bubbles and between the micro-attribution (growth, collapse, acoustic emission etc.) of cavitation and the macro-attribution (pressure fluctuation, instability etc.) of cavitation cloud/flow field. Therefore, a broad review of the relevant fields is thus made so that the background and the initiative of this research on *Cavitation Associated Low-frequency Fluctuation* can be well understood.

1.1. Discovery of Cavitation Phenomenon

The word *CAVITATION* was originally coined by R. E. Froude [1], but the phenomenon was suggested by Euler in 1754. The definition of cavitation phenomenon can be briefly described as local *boiling*, resulting in the formation of bubbles and other vapour regions within the liquid as a result of pressure reduction (rather than increase of temperature, as is usually the case with boiling) to or below the liquid vapour pressure [2]. Cavitation is distinguished from boiling in the sense that the former is induced by the lowering of hydrodynamic pressure, whereas the latter is caused by the raising of vapour pressure to some value in excess of the hydrodynamic pressure [1]. But the two phenomena are related. Cavitation inception and boiling can be compared in terms of the

vapour-bubble dynamics of sub-cooled and super-heated liquids [5]. Sometimes, it would be difficult, especially for cavitation in liquids other than cold water, to make a clear distinction between the two types of phenomena.

In 1893, the first important engineering occurrence of cavitation was discovered and investigated by Charles Parsons due to the failure of the propeller on a British high speed warship [2]. In 1895, Parsons established the first water-tunnel used for cavitation research, and discovered the relationship between cavitation and its damage on the propeller [3]. The first analysis of a problem in cavitation bubble dynamics was performed by L. Rayleigh in 1917, who solved the problem of the collapse of an empty cavity in a large mass of liquid [4]. The above two historical events have underlain the cavitation research theoretically and experimentally. Since then, more than ten thousand research articles and several technical books on cavitation have been published. Nevertheless, our understanding of cavitation and its effects is still very limited.

Since Rayleigh, enormous work has been undertaken on single bubble dynamics which considered the liquid compressibility, viscosity, surface tension, and even the behaviour of the content in the bubble. But, it should be realized that at present it is not yet possible to relate all of the special features of experimentally observed cavitation phenomena with the available experimental and theoretical work on single gas or vapour bubbles. Although it is generally agreed that cavitation damage, white noise, sonoluminescence, chemical reactions, and other features of cavitation are associated with violent bubble motion, at present not only a quantitative understanding of these phenomena is lacking but sometimes even the physical mechanisms through which they take place are obscure [4]. Firstly, the understanding of single bubble itself is still not sufficient, especially for the collapse of vapour bubble in which thermal effect plays a significant role, its modeling is much more difficult than the analysis of the growth. Besides, the nonspherical collapse adds exceeding complexity to the analysis of its behaviour. Therefore, there is still no entirely satisfactory mechanism of single bubble

behaviour available. Secondly, the actual cavitation phenomenon is a multi-bubble behaviour, i. e., a collective behaviour of all bubbles involved. Due to many factors, the nature and behaviour of each bubble appears differently, or say, stochastically. Subsequently, the cavitation events induced by those bubbles must exhibit the stochasticity as well. Therefore, even if we had a perfect single bubble model, it would still be impossible to fully understand the actual cavitation phenomenon and its effects such as cavitation erosion and cavitation pulse spectrum. There are several factors contributing to the stochasticity. Some of them are well known, e. g., the original nuclei, from which the bubbles develop and grow, display a stochastic distributions in terms of both the magnitude (i. e., the radius of nucleus, contents in the nucleus) and the spatial position. These stochastical properties will provide the successive events of bubble behaviour such as the growth and collapse with strong stochasticity. In the second half of this century, especially the last decade, with the applications of advanced observation techniques such as high speed holographic motion picture [6], the actual multi-bubble cavitation phenomenon can be investigated to some extent. Besides, the simulation technology of multi-bubble collapses using disc-shaped bubbles under controlled conditions [7] and others are all helpful to the understanding of the mutual influences between bubbles, or say, the multi-bubble behaviour. All these preliminary results show that the actual cavitation is much more complicated than that described by the single bubble theory. Thirdly, the behaviour of multi-bubbles in a practical flow system is further affected by the interaction between the cavitation region (cloud) and the surrounding liquid even including the response of the whole flow system as has been investigated in this research. Because, once cavitation occurs, the continuity of liquid phase is interrupted and replaced by the cavity volume, subsequently, the original flow pattern is modified and the dynamic interaction between the liquid and its boundary is altered. Usually, the presence of cavitation increases the overall resistance to the flow although, under some conditions in the early state of cavitation development, there may be a measurable decrease. The

effect of cavitation on the guidance of the liquid by the boundary surface is to limit or lessen the force that can be applied to the liquid by the surface [7]. Additionally, the cavitation appears to be a highly unsteady phenomenon even though the external flow was originally steady [1], sometimes, the cavitation has the nature of a periodic process. Therefore, some sort of unsteady dynamic effect will be thus introduced into the surrounding liquid (even in the whole flow system) due to the formation of cavitation. On the other hand, as the cavitation process (i. e., the behaviour of bubbles) is strongly dominated by the flow conditions (such as the pressure/velocity fields, pressure/velocity gradients and their time-dependent variations), the above modification of the flow pattern induced by cavitation will thus inversely affect the cavitation itself, i. e., an interaction or mutual influence between cavitation and surrounding liquid portion/flow system results, which adds further complexity to the cavitation phenomenon. All three factors mentioned above make our understanding of cavitation mechanism very limited and even obscure in some fields.

From the view point of engineering design, there are basically two questions about cavitation which must be answered. Firstly, will cavitation occur in a particular engineering practice? Secondly, if the cavitation is unavoidable, can a given design still function properly? To answer these two challenging problems, extensive new approaches, considering more factors of cavitation nature such as the stochasticity rather than the single bubble theory, are being introduced into contemporary research of cavitation. As one of these efforts, the long term project on *Statistical Characteristics of Cavitation Bubble Collapse Pulses, Associated Low-frequency Fluctuations and Flow Noise*, or abbreviated as *Statistic Cavitation Study* in this thesis, was thus initiated by the author in 1981.

1.2. Development of Cavitation Research

1.2.1. Rayleigh's Analysis

The analysis for the collapse of an empty cavity in an infinite field of liquid was performed by L. Rayleigh in 1917 [8]. Actually, in 1859, W. Besant already formulated the problem in the following physical model: " an infinite mass of homogeneous incompressible fluid acted upon by no forces is at rest, and a spherical portion of the fluid is suddenly annihilated; it is required to find the instantaneous alteration of pressure at any point of the mass, and the time in which the cavity will be filled up, the pressure at an infinite distance being supposed to remain constant. ". Besant used a straight forward application of momentum and continuity equations. That is (refer to Figure 1-1)

$$\frac{\partial u}{\partial t}+u\frac{\partial u}{\partial r}=-\frac{1}{\rho}\frac{\partial p}{\partial r} \tag{1.2-1}$$

$$\frac{\partial}{\partial r}(r^2u)=0 \tag{1.2-2}$$

where:

u =radial component of velocity at any radial distance r ($>R$, the radius of cavity wall)

p =pressure at distance r and time t

Thus, the velocity of the cavity wall at time t will be

$$U=\dot{R}=\frac{dR}{dt} \tag{1.2-3}$$

But, Besant did not elaborate upon his solution and apply it to the cavitation case as did Rayleigh later. In 1917, Rayleigh quoted Besant's above formulation, then he solved this problem in a different way using the energy approach.

Rayleigh assumed a spherically symmetrical flow field, which is an irrotational flow. Therefore, it has the velocity potential Φ, defined by

$$\Phi=\frac{UR^2}{r} \tag{1.2-4}$$

And the velocity $u(r,t)$ at any t and distance r has the relation with cavity-wall velocity U

as follow

$$\frac{u(r,t)}{U}=\frac{R^2}{r^2} \tag{1.2-5}$$

or

$$u(r,t)=\frac{\dot{R}R^2}{r^2} \tag{1.2-6}$$

Substituting (1.2-6) in to Eq. (1.2-1) yields

$$\frac{R^2\ddot{R}}{r^2}+\frac{2R\dot{R}}{r^2}-\frac{2\dot{R}^2R^4}{r^5}=-\frac{1}{\rho}\frac{\partial p}{\partial r} \tag{1.2-7}$$

Integrating (1.2-7) from r to ∞ in respect of r, following relation results,

$$\frac{R^2\ddot{R}}{r}+\frac{2R\dot{R}^2}{r}-\frac{\dot{R}^2R^4}{2r^4}=-\frac{1}{\rho}(p_\infty-p) \tag{1.2-8}$$

On the wall of the cavity, $r=R$, $p=p(R)$, and (1.2-8) becomes the well known Rayleigh equation or Rayleigh-Besant equation,

$$R\ddot{R}+\frac{3}{2}\dot{R}^2=\frac{1}{\rho}(p(R)-p_\infty) \tag{1.2-9}$$

Thus, using the general Bernoulli equation, the pressure $p(r,t)$ in the liquid is readily found as

$$p(r,t)=p_\infty+\frac{R}{r}\left[p(R)-p_\infty\right]+\frac{1}{2}\rho\frac{R}{r}\dot{R}^2\left[1-\left[\frac{R}{r}\right]^3\right] \tag{1.2-10}$$

From Rayleigh's analysis, the substantial nature of cavitation bubble behaviour, such as why the collapse of cavitation bubble induces extremely high pressure in the liquid, and the time of bubble collapse, has been firstly explored theoretically.

The kinetic energy, $(KE)_{liq}$, of the entire liquid at time t can be obtained by integrating the kinetic energy of a concentric fluid shell of thickness dr and density ρ,

$$(KE)_{liq}=\frac{\rho}{2}\int_R^\infty u^2 4\pi r^2 dr=2\pi\rho U^2R^3 \tag{1.2-11}$$

The work done on the entire fluid as the cavity is collapsing from the initial radius R_0 to R is a product of the pressure p_∞ at the infinity and the change in volume of the cavity since zero pressure at the cavity wall is assumed. That is

$$\frac{4\pi p_\infty}{3}(R_0^3-R^3) \tag{1.2-12}$$

Equating Eq.(1.2-11) to Eq.(1.2-12) yields

$$U^2=\frac{2p_\infty}{3\rho}\left[\frac{R_0^3}{R^3}-1\right] \tag{1.2-13}$$

If $\beta=\frac{R}{R_0}$ and substitute $\frac{dR}{dt}$ for U, performing integration for Eq.(1.2-13) gives the time t required for a cavity to collapse from R_0 to R:

$$t=\left[\frac{3\rho}{2p_\infty}\right]^{\frac{1}{2}}\int_R^0\frac{R^{\frac{3}{2}}dR}{\left(R_0^3-R^3\right)^{\frac{1}{2}}}=R_0\left[\frac{3\rho}{2p_\infty}\right]^{\frac{1}{2}}\int_\beta^0\frac{\beta^{\frac{3}{2}}d\beta}{(1-\beta^3)^{\frac{1}{2}}} \tag{1.2-14}$$

If $\beta=0$, the time τ for a complete collapse can be evaluated from Eq.(1.2-14),

$$\tau=0.9146R_0\left[\frac{\rho}{p_\infty}\right]^{\frac{1}{2}} \tag{1.2-15}$$

A complete collapse for an empty bubble based on Eq.(1.2-14) is shown in Figure 1-2.

Due to the assumption of a empty cavity, equation (1.2-13) shows that the velocity U would increases to infinite when R reduces to zero. To avoid this, Rayleigh calculated a cavity filled with the gas which behaved isothermally. Thus, the work done as given by Eq.(1.2-12) is equal to the sum of the kinetic energy of the entire liquid expressed by Eq.(1.2-11) and the work of the gas compression, which equals $4\pi QR_0^3\ln(\frac{R_0}{R})$, where Q is the initial gas pressure. That is

$$U^2=\frac{2p_\infty}{3\rho}\left[\frac{R_0^3}{R^3}-1\right]-\frac{2Q}{\rho}\frac{R_0^3}{R^3}\ln\frac{R_0}{R} \tag{1.2-16}$$

and $U=0$ when

$$p_\infty\frac{z-1}{z}-Q\ln z=0, \tag{1.2-17}$$

here, $z=\frac{R_0^3}{R^3}$. This means that for any real (i. e., positive) value of Q, U comes again to zero before complete collapse, and if $Q>p_\infty$ the first movement of the boundary is outward. The boundary oscillates between two positions, of which one is the initial.

The pressure field in the liquid surrounding the collapsing empty bubble of zero pressure was calculated by Rayleigh as well. Letting

$$Z=\frac{1}{z}=\left[\frac{R_0}{R}\right]^3$$

and with $r \gg R$, the general equation of pressure, $p(r,t)$, is

$$p(r,t)=p_\infty+p_\infty\left[\frac{R}{3r}(Z-4)-\frac{R^4}{3r^4}(Z-1)\right] \tag{1.2-18}$$

And, the maximum value for $p(t)$ is $p_{max}(r,t)$,

$$p_{max}(t)=p_\infty+p_\infty\left[\frac{(Z-4)^{\frac{4}{3}}}{4^{\frac{1}{3}}(Z-1)^{\frac{1}{3}}}\right] \tag{1.2-19}$$

appearing at

$$r(t)=R\left(\frac{4Z-4}{Z-4}\right)^{\frac{1}{3}}$$

The corresponding pressure distribution in the liquid according to Eq.(1.2-18) is shown in Fig.1-3.

Rayleigh's above work has be regarded as an important milestone for the cavitation research in the sense of:

A. The collapsing procedure of an empty spherical bubble and the induced pressure distribution have been described in a concisely analytical form;

B. Although Rayleigh's analysis was based on some approximations, such as incompressible and inviscous liquid, constant pressure p_∞ and negligence of surface tension etc., the resolution explains the substance of bubble collapsing very well, not only qualitatively but also quantitatively. The variation of bubble size during collapsing, as shown in Fig.1-2, calculated by Rayleigh theory coincides very well with the measured curve (from photographs such as done by Knapp et'al 1970); collapsing quicker by about 10 % than the measured. The pressure profile during the collapsing (shown in Fig.1-3) answers the following questions clearly: why the violent pressure will be induced during bubble collapsing; when and whereabouts it appears. And, the oscillation of the bubble boundary following the collapsing as described by Eq.(1.2-17) also gives a very good picture and explanation of the bubble rebouncing although the decay effect is neglected due to the assumptions of inviscous liquid and no energy dissipation.

Rayleigh's analyses have formed the most important basic of cavitation research especially for single bubble dynamics.

1.2.2. Single Bubble Dynamics

Instead of assuming an empty bubble collapsing, most of the progress in understanding the single bubble behaviour has been achieved by considering the dynamic equilibrium of a spherical bubble containing vapour and non-condensible gas in a variably ambient pressure field of a liquid with viscosity and surface tension.

If the bubble is static, the interior pressure p_i can be expressed as

$$p_i = p_v + p_g = p(R) + \frac{2\sigma}{R}$$

where:

p_v=vapour pressure

p_g=gas pressure

σ=surface tension

That is, the introduction of surface tension makes the interior pressure in static condition greater than the external pressure of bubble-wall.

The viscosity also induces further pressure difference. In general, viscosity appears in two terms of the Navier-Stokes form of the momentum equation as follows,

$$\rho \frac{d\vec{v}}{dt} = \rho \vec{F} - \nabla p + \mu \Delta \vec{v} + \frac{1}{3}\mu \nabla div \vec{v} \qquad (1.2\text{-}20)$$

where:

$\vec{v}$=velocity vector

μ=dynamic viscosity

The terms containing viscosity will disappear for an irrotational motion of an incompressible liquid ($div\vec{v}=0$ for an incompressible liquid; $\Delta\vec{v}=\nabla^2(\nabla\phi)=\nabla(\nabla^2\phi)=0$ for an irrotational motion). However, Poritsky [9] pointed out that the viscosity mainly affects the motion of interface (i. e., the wall movement). The principal normal pressure p_1, p_2, p_3 have the

relations with the principal normal rate of strains $\frac{\partial \varepsilon_1}{\partial t}, \frac{\partial \varepsilon_2}{\partial t}, \frac{\partial \varepsilon_3}{\partial t}$ as follows

$$p_1 = p - 2\mu \frac{\partial \varepsilon_1}{\partial t} + \frac{2}{3}\mu \frac{\partial \varepsilon}{\partial t}$$

$$p_2 = p - 2\mu \frac{\partial \varepsilon_2}{\partial t} + \frac{2}{3}\mu \frac{\partial \varepsilon}{\partial t}$$

$$p_3 = p - 2\mu \frac{\partial \varepsilon_3}{\partial t} + \frac{2}{3}\mu \frac{\partial \varepsilon}{\partial t}$$

where:

p =mean pressure

$$p = \frac{(p_1 + p_2 + p_3)}{3}$$

ε =volume dilation

$$\varepsilon = \varepsilon_1 + \varepsilon_2 + \varepsilon_3$$

In the problem of the symmetrical motion of a spherical bubble, the rate of strain $\frac{\partial \varepsilon_1}{\partial t}$ becomes

$$\frac{\partial \varepsilon_1}{\partial t} = -2\frac{\frac{dR}{dt}}{R}$$

because the radial direction is a principal axis. Thus, the pressure $p(R)$ at the bubble wall in the liquid can be expressed as follows

$$p(R) = p_v - 4\mu \frac{\frac{dR}{dt}}{R} - \frac{2}{3}\mu \frac{\partial \varepsilon}{\partial t}$$

For incompressible liquid, i. e., $\frac{\partial \varepsilon}{\partial t} = 0$,

$$p(R) = p_v - 4\mu \frac{\frac{dR}{dt}}{R} \qquad (1.2\text{-}21)$$

or, with surface tension,

$$p(R) = p_v - 4\mu \frac{\frac{dR}{dt}}{R} - \frac{2\sigma}{R} \qquad (1.2\text{-}22)$$

From Eq.(1.2-21), it can be seen that the viscosity has the highest effect in the early stages of bubble growth and near collapse due to the maximum values of $\frac{dR}{dt}$. Poritsky's treatment modified the Rayleigh Equation resulting in a generalized Rayleigh Equation,

$$R\ddot{R}+\frac{3}{2}(\dot{R})^2=\frac{1}{\rho}\left(p_i-p_\infty-\frac{2\sigma}{R}-\frac{4\mu}{R}\dot{R}\right) \tag{1.2-23}$$

Here, the pressure at the bubble wall, p_i, may be a function of the time, and the pressure at infinite, p_∞, may also be a function of time.

Shu, S. S. [10] theoretically proved that bubble motion without surface tension leads to an infinite collapsing time if the parameter

$$\mu'=\frac{4\mu}{R_0\left[\rho(p_\infty-p_i)\right]^{\frac{1}{2}}}$$

exceeds a critical value, i. e., $\mu'\geq 0.46$, where R_0 is the initial radius of bubble. However, as a matter of fact, the time of collapsing can always be shown to be finite if the effect of the surface tension is included.

The influences of viscosity and surface tension on the growth and collapse of bubble according to Eq.(1.2-23) can be seen from Figs. 1-4 and 1-5, in which R_0 is the initial radius of bubble and σ' is the other parameter describing the property of surface tension,

$$\sigma'=\frac{\sigma}{R_0\left[p_\infty-p_i\right]^{\frac{1}{2}}}$$

As to the problem of the bubble content, the modern investigation of bubble dynamics arranges itself under two basic categories: One is the *Gas Bubble Dynamics* in which the bubble interior consists mostly of the permanent gas. The other is the *Vapour Bubble Dynamics* in which the bubble interior is composed almost entirely of the vapour of the surrounding liquid. The vapour bubble dynamics can be further divided into the vapour-bubble dynamics in a *subcooled liquid* and the vapour-bubble dynamics in a *superheated liquid* [4]. The former is the case in which the vapour density is so small that the bubble motion is dominated by the inertia of the liquid not the latent heat flow. The liquid may be said to be *cold*, and the liquid is usually called cavitation liquid. This case corresponds to most cavitation situations appearing in the hydraulic engineering practices, such as the cavitation in hydraulic machinery, in which the cavitation develops because the dynamic pressure drops to or below the vapour pressure. The superheated liquid is one in which

the vapour bubble motion is controlled by the latent heat flow rather than the liquid inertia, e. g., the boiling.

Gas Bubble Dynamics

It is assumed that the medium filling the cavity is basically a permanent, noncondensable gas and all the effects of the vapour present in the bubble is neglected due to the small partial pressure of the vapour (compared with the gas pressure).

For the analysis of the small-amplitude oscillation of gas bubble, the linearization method is adopted, which has been summarized by Plesset and Prosperetti [4]. Usually, the small-amplitude radial oscillation is induced when the gas bubble is immersed in a sound field of a wavelength large compared with the bubble radius. Such a driving pressure perturbation can be approximated as

$$p_\infty(t)=P_\infty(1+\varepsilon\cos\omega t) \tag{1.2-24}$$

where:

P_∞=average ambient pressure

ω=angular frequency of driving pressure or sound frequency

ε=small dimensionless amplitude of perturbation, $|\varepsilon| \ll 1$

Thus, the bubble radius can be expressed as

$$R(t)=R_0(1+x(t)) \tag{1.2-25}$$

where:

$x(t)$=a small quantity of order ε, $|x(t)| \ll 1$

R_0=equilibrium radius

$$R_0=\frac{2\sigma}{p_{i,eq}-P_\infty}$$

$p_{i,eq}$=average internal pressure or the internal pressure at equilibrium

The internal pressure $p_i(t)$ is linearized about its equilibrium pressure $p_{i,eq}$ as follows

$$p_i(t)=p_{i,eq}+\left[\frac{\partial p_i}{\partial x}\right]_{x=0,\dot{x}=0}x(t)+\left[\frac{\partial p_i}{\partial \dot{x}}\right]_{x=0,\dot{x}=0}\dot{x}(t)+\cdots \tag{1.2-26}$$

Thus, if $\alpha=\frac{P_a}{\rho R_0}$, the generalized Rayleigh equation becomes of the damped harmonic-oscillation form

$$\ddot{x}+2\beta\dot{x}+\omega_0^2 x=-\varepsilon\alpha e^{i\omega t} \tag{1.2-27}$$

And, some characteristic parameters of bubble oscillation can be determined. The damping constant β is given as

$$\beta=\frac{2\mu_l}{\rho R_0^2}-\frac{1}{2\rho}\left[\frac{\partial p_l}{\partial x}\right]_{x=0,\dot{x}=0} \tag{1.2-28}$$

The natural frequency of bubble oscillation is ω_0,

$$\omega_0^2=-\frac{1}{\rho}\left[\frac{\partial p_l}{\partial x}\right]_{x=0,\dot{x}=0}-\frac{2\sigma}{\rho R_0^3} \tag{1.2-29}$$

If the gas follows a polytropic law of compression, i. e.,

$$p_l=p_{l,eq}\left[\frac{R_0}{R}\right]^{3k} \tag{1.2-30}$$

where:

k =polytropic exponent

the natural frequency of bubble could be simplified as

$$\omega_0^2=3k\frac{p_{l,eq}}{\rho R_0^2}-\frac{2\sigma}{\rho R_0^3} \tag{1.2-31}$$

Using the linearized formulation with the assumption that the external pressure is the superposition of the contributions of the driving sound field and the acoustic radiation from the bubble and taking into account the thermal effects by introducing an additional effective " thermal " viscosity μ_{th}, Prosperetti [50] obtained the damped harmonic oscillation equation (1.2-27) in the following form,

$$\ddot{x}+(4\frac{\mu_l+\mu_{th}}{\rho_l R_0^2}+\frac{\frac{\omega R_0}{c}}{1+(\frac{\omega R_0}{c})^2}\omega)\dot{x}+(3k\frac{p_{l,eq}}{\rho_l R_0^2}-\frac{2\sigma}{\rho_l R_0^3}+\frac{(\frac{\omega R_0}{c})^2}{1+(\frac{\omega R_0}{c})^2}\omega^2)x=-\varepsilon\alpha e^{i\omega t}$$

where:

c =sound speed in liquid

ρ_l=liquid density

Thus, the natural frequency is

$$\omega_0^2=3k\left(\frac{p_{l,eq}}{\rho_l R_o^2}\right)-\frac{2\sigma}{\rho_l R_o^3}+\frac{\left(\frac{\omega R_o}{c}\right)^2}{1+\left(\frac{\omega R_o}{c}\right)^2}\omega^2$$

and the viscous, thermal and acoustic damping constants can be respectively identified as

$$\beta_{viscous}=\frac{2\mu}{\rho_l R_o^2}$$

$$\beta_{thermal}=\frac{2\mu_{th}}{\rho_l R_o^2}$$

$$\beta_{acoustic}=\frac{\omega\frac{\omega R_o}{c}}{2\left[1+\left(\frac{\omega R_o}{c}\right)^2\right]}$$

The dependence of the damping constant β ($=\beta_{viscous}+\beta_{thermal}+\beta_{acoustic}$) on the driving frequency can be seen clearly. Except for extremely small bubbles as mentioned above, the low-frequency damping is mainly controlled by thermal effect, and the high-frequency damping by acoustic effects. An example of forced oscillation of an air bubble in water for two different equilibrium radius, R_0=10^{-3} and 10^{-4} cm respectively, are shown in Figure 1-6, in which the circle denotes the resonant frequency of bubble.

As to the relation of the damping constant β with the bubble size R_o, Figure 1-7 shows the results of Chapman and Plesset [51] demonstrating the logarithmic decrement $\Lambda=\frac{2\pi\beta}{\omega_0}$ of an air bubble in water, which is based on the physical model of the free oscillations of a gas bubble taking into account the surface tension, viscosity, thermal conduction in the gas, and acoustic radiation. The acoustic contribution which did not appear in Eq.(1.2-28) is here approximated as

$$\beta_{acoustic}=\frac{1}{2}\omega\frac{\frac{\omega R_0}{c}}{1+\left(\frac{\omega R_0}{c}\right)^2}\simeq\frac{1}{2}\left(\frac{\omega R_0}{c}\right)\omega$$

In the range of R_0=10^{-1} ~ 4×10^{-4} cm, the thermal component $\beta_{thermal}$, represented by the second term $\frac{1}{2\rho}\left[\frac{\partial p_l}{\partial x}\right]_{x=0,t=0}$ in Eq.(1.2-28), dominates over the viscous and acoustic con-

tributions to the energy dissipation. From Figure 1-7, it is also can be seen that for extremely small bubbles, such as $R_0<1.5\times10^{-4}$ cm, viscosity plays a very important role in energy dissipation.

The dependence of the effective polytropic exponents k on the driving frequency ω of the pressure perturbation was also demonstrated by Prosperetti [50] as

$$k=\frac{1}{3}\left(\frac{\omega^2\rho_L R_0^2}{P_{L\infty}}\right)\mathrm{Re}\,K$$

where:

K =complex quantity describing all the thermal effects associated with the gas bubble, which is a function of ω, R_0 and the properties of the liquid and the gas [50]

If G_1 is designated as the dimensionless driving frequency,

$$G_1=\frac{MD_g\omega}{\gamma R_g T_\infty}$$

where:

M =molecular weight of gas

D_g =thermal diffusivity of gas

R_g =universal gas constant

T_∞ =absolute temperature of the liquid at a distance from the bubble

γ=adiabatic exponent, $\gamma=\frac{7}{5}$ for diatomic gas

And, G_2 denotes a dimensionless parameter in respect of thermal diffusivity of gas,

$$G_2=\frac{R_0^2\omega}{D_g}$$

Then, the relation of the polytropic exponent k with the frequency ω can be expressed in terms of G_1 and G_2,

$$k=\frac{1}{3}\gamma G_1 G_2\,\mathrm{Re}\,K$$

Figure 1-8 shows how the effective polytropic exponent k for the small-amplitude forced oscillations of a gas bubble depends on the driving frequency in terms of G_1 and G_2. There are basically three length scales involved in this problem, bubble radius R_0, the wavelength (λ_g) of sound in gas

$$\lambda_g = \frac{2\pi(\frac{\gamma R_g T_\infty}{M})^{\frac{1}{2}}}{\omega}$$

and the thermal penetration depth in the gas $L_{th}=(D_g/\omega)^{\frac{1}{2}}$. Thus, it can be obtained that

$$G_1 \propto \left[\frac{L_{th}}{\lambda_g}\right]^2; \quad G_2 \propto \left[\frac{R_0}{L_{th}}\right]^2$$

This result explains the gas-bubble behaviour quite well. If $(G_1G_2)^{\frac{1}{2}}$, i. e., $\frac{R_0}{\lambda_g}$, is very small, the pressure within the bubble is spatially uniform. If the oscillations are so slow that a significant temperature gradient within the gas of bubble can not be built up, i. e., $G_2<1$, an isothermal behaviour will result. If the driving frequency is so fast that the gas is thermally insulated from the surrounding liquid, an adiabatic gas behaviour can be observed.

For the general case of gas bubble oscillation in an oscillating pressure field, i. e., the dimensionless pressure amplitude is not necessarily small, the foregoing linearized approach can no more be used. Due to the complexity of the non-linear effect, the investigations were mostly done through the numerical approach. Noltingk and Neppiras [13] have made an important contribution, in the early stage, showing the apparently explosive behaviour of the gas-bubble oscillations with the assumptions of isothermal behaviour ($k=1$) and non-viscosity. The behaviour sometimes presents a very fast growth followed by a violent collapse to very small radius during a single period of the driving pressure oscillation. Following Noltingk-Neppiras guide, much subsequent work has been done. Figure 1-9 shows the result from Borotnikova and Soloukin [53], demonstrating that the explosive behaviour appears after several periods of driving force oscillation when bubbles are driven below or above resonance frequencies respectively.

Assuming the polytropic gas behaviour and neglecting the thermal and acoustic energy dissipation, the forced oscillations of a spherical gas bubble in an incompressible, viscous liquid can be expressed in the following nonlinear ordinary differential equation [13], which is sometimes called the RPNNP (Rayleigh, Plesset, Noltingk-Neppiras and Poritsky)-bubble model,

$$\begin{cases} R\ddot{R}+\frac{3}{2}(\dot{R})^2=\frac{1}{\rho}\left[p_g\left[\frac{R_0}{R}\right]^{3k}+p_v-P_\infty-\frac{2\sigma}{R}-4\mu\frac{\dot{R}}{R}-p(t)\right] \\ p_g=\frac{2\sigma}{R_0}+P_\infty-p_v \end{cases} \tag{1.2-32}$$

where:

p_v=vapour pressure remaining basically constant

For the numerical computation, $p(t)$ is often expressed in the sinusoidal form,

$$p(t)=-\eta P_\infty \cos\omega t$$

where:

η=dimensionless pressure amplitude, which is not necessarily small

ω=angular frequency which should not exceed certain value to ensure that the wavelength of the external pressure oscillation is much larger than the bubble radius and the value of the pressure $p(t)$ at the bubble-wall can be treated as uniform

In the 1970's, Lauterborn [52] undertook an extensive numerical work on the solution of Eq.(1.2-32). He calculated three cases of the gas-bubble oscillations for $R_0=10^{-3}$, 10^{-4} and 10^{-5} cm respectively. The normalized " amplitude "

$$\frac{R_{max}-R_0}{R_0}$$

where:

R_{max}=maximum value of the radius during the steady oscillations

was plotted against the normalized frequency $\frac{\omega}{\omega_0}$, where ω_0 denotes the linearized resonant frequency obtained from the Eq.(1.2-31). The result for an air bubble of $R_0=10^{-3}$

cm in water at $20^0 C$ (ρ=0.998 $g\ cm^{-3}$, μ=0.01 $g\ cm^{-1}\ sec^{-1}$, σ=72.5 $dyn\ cm^{-1}$) under a static pressure P_∞=1 bar for several values of the pressure amplitude are shown in Figure 1-10. The fractions on the resonance peaks denote the order of the resonance, i. e., $\frac{n}{m}$ indicates that the period of the bubble oscillation is m times of the driving-pressure period and n times of the bubble free-oscillation period ($=\frac{2\pi}{\omega_0}$). The variation of the resonances shown in Figure 1-10 illustrates very clearly how the nonlinear effects of large pressure oscillation affect the characteristics of bubble oscillations, e.g. the Spring Softening effect of the nonlinear system that the resonance peak of the buble oscillations is gradually leaning towards the lower frequency region with the increase of the driving-pressure amplitude.

In Figure 1-10, it is also shown that some discontinuities appear on the steady-state response curves due to the instability of the small-amplitude oscillation in a frequency region in which the response curve is multivalued. The subharmonic bubble oscillation behaviour is also observed in Figure 1-10, which is denoted by the fraction of $\frac{1}{2}$ at the peak at the frequency of $\frac{\omega}{\omega_0}$=2.

Cavitation Bubbles

Dominated by the dynamic pressure effect, a bubble composed mainly of vapour (which usually originates from small gas nucleus) grows to many times of its initial size so fast that the mass-diffusion effect can be neglected, and the gas content plays an unimportant role in the dynamics except near the end of the collapse. According to the importance of the thermal effect, this sort of bubble can be further divided into two categories: *Cavitation Bubbles* and *Boiling Bubbles*. Plesset and Prosperetti [4] have given an explanation about these two sorts of bubbles. If a bubble in water grows to a radius R in a time of t, the amount of thermal energy required to fill the bubble with vapour in thermodynamic equilibrium with the water is

$$\frac{4}{3}\pi R^3 L \rho_{v,eq}(T)$$

where:

L=latent heat of evaporation

$\rho_{v,eq}(T)$=equilibrium vapour density at water temperature T

This energy is acquired through a drop ΔT in temperature of the surrounding liquid layer of thickness of the order of the diffusion length $(D_l t)^{\frac{1}{2}}$, where $D_l = \frac{k}{\rho c_l}$ is the thermal diffusivity in the liquid. Therefore, the heat energy supplied is

$$4\pi R^2 (D_l t)^{\frac{1}{2}} \rho c_l \Delta T$$

Equating the above two energy expression, the temperature drop ΔT can be evaluated as follows

$$\Delta T \simeq \frac{1}{3} \frac{R \rho_{v,eq}(T) L}{(D_l t)^{\frac{1}{2}} \rho c_l} \tag{1.2-33}$$

To show the influence of water temperature T on vapour bubble behaviour, two extreme examples are examined by Plesset and Prosperetti [4]. For water at $15^{\circ}C$, with R=0.1 cm, $t=10^{-3}$ sec, $\rho_{v,eq}=1.3\times10^{-3} g\ cm^{-3}$, ΔT can be evaluated as $\simeq 0.2^{\circ}C$. This temperature drop causes a reduction of the equilibrium vapour pressure only of the order of 1%, therefore has little effect on the bubble growth. Whereas for the water with the temperature of $100^{\circ}C$, the equilibrium vapour density $\rho_{v,eq}(100^{\circ}C)$ becomes about 46 times its value at $15^{\circ}C$, i. e.,

$$\rho_{v,eq}(100^{\circ}C) = 46 \times \rho_{v,eq}(15^{\circ}C)$$

resulting a large temperature drop,

$$\Delta T = 13^{\circ}C$$

which corresponds to a vapour pressure reduction of $\Delta p_v \simeq 50\%$. Subsequently, the bubble needs a larger growth time to the same radius, i. e., the thermal effect (rather than the inertial effect) controls growth. The distinction between above extreme cases is caused by the strong temperature dependence of the equilibrium vapour density $\rho_{v,eq}(T)$ and the

corresponding change rate of the equilibrium vapour pressure $p_{v,eq}(T)$ with the temperature. The first case is usually referred as *Cavitation Bubble*, and the second as *Boiling Bubble*. Similarly, for collapse process, the internal pressure of a cavitation bubble will remain basically constant until the final stage of the collapse, whereas for boiling bubble, the vapour pressure will play a much greater role. The dynamics of the cavitation bubble is further briefly introduced as follows.

For the cavitation bubble, the approximations are made that the internal pressure $p_v(t)$ is considered as $p_v(t)=p_v(t)$=constant, the ambient pressure is $p_\infty(t)$=constant, and the viscous effect is neglected.

Substituting

$$R\ddot{R}+\frac{3}{2}\dot{R}^2=\frac{1}{2}\frac{1}{R^3\dot{R}}\frac{d}{dt}(R^3\dot{R}^2)$$

into the following generalized Rayleigh equation

$$R\ddot{R}+\frac{3}{2}\dot{R}^2=\frac{1}{\rho}\left[p_v-p_\infty-\frac{2\sigma}{R}\right]$$

it can be integrated, yielding the following solution for bubble growth:

$$\dot{R}^2=\left[\frac{R_0}{R}\right]^3\dot{R}_0^2+\frac{2}{3}\frac{p_v-p_\infty}{\rho}\left[1-\left[\frac{R_0}{R}\right]^3\right]-\frac{2\sigma}{\rho R}\left[1-\left[\frac{R_0}{R}\right]^2\right] \qquad (1.2\text{-}34)$$

where:

R_0=initial radius for the growth

The above result (Eq.1.2-34) gives important information of cavitation bubble behaviour as follows.

If the initial pressure, p_v, is greater than the ambient pressure p_∞, the wall velocity, $\dot{R}$, will approach an asymptotic value when the bubble grows to a fairly large size. That is, if $p_v>p_\infty$ and when $R\gg R_0$,

$$\dot{R}\to\left[\frac{2}{3}\frac{p_v-p_\infty}{\rho}\right]^{\frac{1}{2}}$$

This velocity limitation means that all the work performed by the pressure forces, p_v and p_∞ is transformed into the kinetic energy of the flow.

If $p_v < p_\infty$ and the surface tension is neglected, the bubble will stop growing when it reaches a maximum radius, R_{max},

$$R_{max}=\left[1+\frac{1}{2}\rho\dot{R}_0^2(p_\infty-p_v)^{-1}\right]R_0$$

For the bubble collapse, a similar solution of the generalized Rayleigh equation can be obtained,

$$\dot{R}^2=\frac{2}{3}\frac{p_\infty-p_v}{\rho}\left[\left(\frac{R_0}{R}\right)^3-1\right]+\frac{2\sigma}{\rho R}\left[\left(\frac{R_i}{R}\right)^2-1\right] \qquad (1.2\text{-}35)$$

where:

R_i =initial radius from which bubble starts collapsing and at which initial wall velocity equals zero

If the surface tension is neglected, the time required for the complete collapse can be computed from Eq.1.2-35,

$$t_c=\frac{\Gamma(\frac{5}{6})}{\Gamma(\frac{1}{3})}(\frac{3\pi\rho}{2(p_\infty-p_v)})^{\frac{1}{2}}R_i=0.915(\frac{\rho}{p_\infty-p_v})^{\frac{1}{2}}R_i$$

This result is also obtained by Rayleigh.

A paradox could be derived from Eq.(1.2-35) that at the final stage of the collapse the wall velocity, $\dot{R}$, would approach infinite. That is, when $R\to 0$, $\dot{R}\to\infty$. The reasons for this paradox are as follow. Firstly, the assumption of incompressibility of liquid is no longer correct when the collapse comes to the final stage (i.e. the bubble-wall velocity becomes comparable with the sound speed in the water), which gives a over-evaluated wall-velocity. Secondly, the approximation of the internal pressure $p_i=p_v$=constant deviates far from the physical behaviour at $R\to 0$ when the gas existing in the bubble is no more negligible and plays a more important role in retarding the collapsing than the vapour whose pressure is assumed constant during the whole process of collapsing. Finally, the assumption of the spherically symmetric collapse is unsuitable during the final collapsing stage. These three effects will be respectively further explained in the following part of this section.

Effect of Liquid Compressibility

When the collapsing velocity at the final stage of collapse is large enough to compare with the sound speed in liquid, the compressibility of liquid becomes important and functions in both retarding the collapse velocity and changing the collapsing energy into the acoustic energy emitted outwards in the liquid.

Trilling's work [11] considering the liquid compressibility for a gas filled bubble collapse is based on the following assumptions. The liquid with a linear relation between pressure and density is assumed and the velocities are small compared with the sound speed. Then, he used the following acoustic equation as the governing equation for the diverging spherical waves

$$\left[\frac{\partial}{\partial t}+c\frac{\partial}{\partial r}\right] r\Phi=0$$

where:

Φ=velocity potential

c=sound speed in liquid

This implies that the quantity $r\Phi$ is propagated through the liquid with sonic velocity c. So, his approach is regarded as an acoustic method with first-order correction for compressibility of liquid. Since the shocks are weak ($\frac{\Delta P}{P}=0.1$), he also follows the treatment that the velocity behind the reflected spherical shock is small compared with the velocity ahead of it and that the gas behind the reflected shock is at sensibly constant density. Based on the above approach, Trilling treated the adiabatic collapse and rebound of a bubble filled with nonconducting nonviscous perfect gas.

To improve the above acoustic approach, Gilmore [12] used the Kirkwood-Bethe approach, i. e., the pressure perturbation propagates at the velocity which is equal to the sum of the sound velocity c and the local liquid particle velocity u. Thus, Gilmore used the characteristic line, along which the momentum and continuity equations are simultaneously solved, traced by a point moving at the velocity $u+c$ instead of c. Gilmore

calculated a bubble collapsing in water under a constant pressure difference, $p_\infty - p_v = 0.517$ atm. The result is shown in Figure 1-11, which is compared with the Rayleigh's incompressible solution and Herring/Trillings' first-order compressible/acoustic approach. In the Figure, Rayleigh's result is an incompressible solution for an empty cavity, Schneider's result is obtained through the numerical integration to solve the partial differential equations for compressible flows. It has been revealed [3] that when the Mach number ($M = \frac{|U|}{c}$) is above 0.3, the effect of liquid compressibility becomes remarkably important; when relative radius, $\frac{R}{R_0}$, reaches to the value of 0.1, the bubble-wall collapsing velocity calculated through Gilmore's compressible approach is only 40% of that evaluated by classical hypothesis (Rayleigh theory). In Scheider's numerical computation, he used the incompressible solution at $\frac{R}{R_0} = 0.08$, which was obviously too high, as the initial condition. This is presumably the cause introducing the discrepancy at the range of $\frac{R}{R_0} = 0.08 - 0.02$ with the Gilmore's analytical result as shown in Fig.1-11.

Gilmore's analysis neglected the effect of the variation of the gas content on the bubble behaviour, which has the functions of retarding collapse and reducing maximum collapsing velocity (it will be discussed in following part of this section). The calculation performed by Ross [3] show that only in the rare case in which the partial pressure of gas content Q is lower than 1% of the surrounding pressure P_∞, i. e., $\frac{Q}{P_\infty} < 0.01$, the above effect of the liquid compressibility just becomes significant and not negligible. However, it is just the liquid compressibility that enables the bubble collapsing energy to be partially changed into the acoustic energy emitting outwards in the liquid.

Effect of Gas Content in Bubble

As has been noticed that although the gas content in a cavitation bubble is usually very small compared with the vapour content, it does play a very important role at the final stage of collapse. The physical behaviour of it at the final collapse is that with the

increase of the partial pressure of gas, the kinetic energy of collapsing is partially being changed into the potential energy, in pressure energy form, of the compressed gas resulting in retarding the collapse velocity (which vanishes at a finite minimum radius of the bubble instead of a complete collapse); subsequently, the reserved potential energy in compressed gas during the collapse course will causes the successive rebounding and oscillation.

A typical procedure of the collapse and successive rebound of a partially gas filled bubble is shown in Figure 1-12, in which the volume of the cavity on first *rebound* is about 65% of that of the initial bubble, that is, the total loss of mechanical energy for the first period is about 35% of the total energy due to the dissipation as a shock wave in liquid, viscous friction, entropy increase through the nonreversible processes in the gas or vapour. But, many investigators' calculations [7] show that for the common case in which the cavitation occurs in a liquid of low vapour pressure and low dissolved gas content, the total amount of mass contained in the cavity is capable of storing only a small fraction of the total energy. Practically, the major part of the collapse energy must therefore be stored in the compression of the surrounding liquid. But, if either the vapour pressure or the gas content in the bubble is high enough, a considerable part of collapse energy would be stored in the potential energy form by the bubble content and the collapse pressure would also be reduced accordingly.

L. Rayleigh is the first person who realized the important role of gas content in retarding collapse especially for the final stage. He assumed an isothermal process and derived the wall-velocity of collapsing bubble-wall, i. e. Eq.(1.2-16),

$$\dot{R}^2=\frac{2}{3}\frac{P_\infty}{\rho}\left[\frac{R_0^3}{R^3}-1\right]-\frac{2Q}{\rho}\frac{R_0^3}{R^3}\ln\frac{R_0}{R}$$

where:

Q=initial partial pressure of gas in bubble

R_0=initial bubble radius

From Eq.(1.2-16), the minimum value of radius R_{min} is approximated as

$$R_{min}=R_0 e^{-\frac{P_-}{3Q}} \tag{1.2-36}$$

and the corresponding maximum pressure of gas content, $p_{g,max}$, is

$$p_{g,max}=Q\left(\frac{R_0}{R_{min}}\right)^3=P_-\left(\frac{Q}{P_-}\right)e^{\frac{P_-}{Q}} \tag{1.2-37}$$

It should be noticed that if the ratio of gas partial pressure Q to infinite pressure P_- becomes too small, for say 2%, the peak value of p_g would be over-estimated too much. If $\frac{Q}{P_-}$=2%, $p_{g,max}$ would be over-evaluated as $P_-\times10^{20}$ which is obviously unpractical and unacceptable [3].

Noltingk and Neppiras [13] improved Rayleigh's work by assuming an adiabatic process of gas content instead of the assumption of isothermal process which is much closer to the actual gas behaviour especially during the final stage of collapse. The Noltingk - Neppiras approach is demonstrated by Ross [3] in a more accurate way as follows:

Remaining the assumption of an incompressible and inviscous liquid, the generalized Rayleigh equation takes following form

$$R\ddot{R}+\frac{3}{2}\dot{R}^2=\frac{P_-}{\rho}\left[1+\frac{Q}{P_-}\left(\frac{R_0}{R}\right)^{3\gamma}\right]$$

where:

Q=initial partial pressure of gas content, i.e. gas pressure at $R=R_0$

γ=adiabatic exponent

Using the identity

$$R\ddot{R}^2+\frac{3}{2}\dot{R}^2=\frac{1}{2R^2R}\frac{d}{dt}\left[R^3\dot{R}^3\right]$$

the collapsing velocity and acceleration of the bubble-wall can be respectively calculated as

$$\dot{R}^2=\frac{2}{3}\frac{P_-}{\rho}\left(\frac{R_0}{R}\right)^3\left[1-\left(\frac{R}{R_0}\right)^3+\frac{Q}{P_-(\gamma-1)}\times\left(1-\frac{1}{\gamma-1}\left(\frac{R_0}{R}\right)^{3(\gamma-1)}\right)\right] \tag{1.2-38}$$

and

$$\ddot{R}=\frac{P_{\infty}R_0^3}{\rho R^3}\left[1+\frac{Q}{P_{\infty}(\gamma-1)}-\frac{Q\gamma}{P_{\infty}(\gamma-1)}\left(\frac{R_0}{R}\right)^{3(\gamma-1)}\right]$$

The minimum radius is

$$R_{min}=R_0\left(\frac{Q}{P_{\infty}(\gamma-1)}\right)^{\frac{1}{3(\gamma-1)}}\left(1+\frac{Q}{P_{\infty}(\gamma-1)}\right)^{\frac{-1}{3(\gamma-1)}}$$

and, the maximum partial pressure of gas at $R=R_{min}$ is

$$P_{g,max}=Q\left(\frac{P_{\infty}(\gamma-1)}{Q}\right)^{\frac{\gamma}{\gamma-1}}\left(1+\frac{Q}{P_{\infty}(\gamma-1)}\right)^{\frac{\gamma}{\gamma-1}}$$

Ross [3] calculated the minimum of the radius R_{min} against the gas content $\frac{Q}{P_{\infty}}$ for two different gases with adiabatic exponents of $\gamma=1.4$ and $\gamma=\frac{4}{3}$ respectively (shown in Figure 1-13).

The maximum gas temperature (Kelvin scale ^{o}K) based on the adiabatic process is

$$T_{g,max}=T_0\frac{P_{g,max}}{Q}\left(\frac{R_{min}}{R_0}\right)^3=T_0\left(\frac{P_{\infty}(\gamma-1)}{Q}\right)\left(1+\frac{Q}{P_{\infty}(\gamma-1)}\right)$$

where:

T_0=initial gas temperature, i. e., temperature at $R=R_0$, (^{o}K)

Due to the assumption of incompressible liquid, the Noltingk-Neppiras theorem would also over-estimate the temperature and the collapsing velocity. For example, if $Q<0.1P_{\infty}$, the maximum temperature of gas content $T_{g,max}$(^{o}K) would exceed one thousand Kelvin.

From Eq.(1.2-38), the maximum velocity of bubble-wall during collapse is

$$\left(\dot{R}\right)^2_{max}=\frac{2P_{\infty}(\gamma-1)}{3\rho\gamma}\left(\frac{P_{\infty}(\gamma-1)}{Q\gamma}\right)^{\frac{1}{\gamma}}\left(1+\frac{Q\gamma}{P_{\infty}(\gamma-1)}\right)^{\frac{\gamma}{\gamma-1}} \qquad (1.2\text{-}39)$$

Thus, the maximum Mach number M_{max} can be evaluated

$$M_{max}=\left[\frac{2P_{\infty}}{3\rho c^2}\left(\frac{\gamma-1}{\gamma}\right)\right]^{\frac{1}{2}}\left(\frac{P_{\infty}(\gamma-1)}{Q\gamma}\right)^{\frac{1}{2(\gamma-1)}}\left(1+\frac{Q\gamma}{P_{\infty}(\gamma-1)}\right)^{\frac{\gamma}{2(\gamma-1)}}$$

It has been pointed by Ross [3] that for the cases of $\frac{R_{min}}{R_0}<0.25$, i. e., corresponding to $\frac{Q}{P_{\infty}}<10\%$, the value of M_{max} has basically nothing to do with the value of γ, which could

be approximately expressed in terms of the ratio of R_{min} to R_0 as follows

$$M_{max}=\left[0.015\frac{R_0}{R_{min}}\right]^{\frac{3}{2}}\left(P_{\infty A}\right)^{\frac{1}{2}} \tag{1.2-40}$$

where:

$P_{\infty A}$=surrounding pressure expressed in the unit of atmosphere

Through the investigation of the relation of M_{max} with $\frac{Q}{P_\infty}$, Ross [3] found that the validity of the assumption of a incompressible liquid mainly depends on the values of $P_{\infty A}$ and $\frac{Q}{P_\infty}$. For $P_{\infty A}$=1, the validity still remains even when the value of $\frac{Q}{P_\infty}$ reduces down to 1%; whereas for $P_{\infty A}$=10, $\frac{Q}{P_\infty}$>4% is required. For most of the practical cavitation problems, these requirements are met except for some extreme cases in which the gas content is very low. Therefore, the incompressibility assumption is practically acceptable.

As has been mentioned before, the function of compressibility is retarding collapsing, resulting in both the increase of the minimum radius R_{min} and the reductions of the maximum collapsing pressure and temperature. Hickling and Plesset [14] made an analysis of a gas bubble collapsing in a compressible liquid using the Gilmore's approach. It was found that for a given gas, the minimum radius R_{min} depends firstly on the ratio of the gas pressure Q to the collapsing pressure P_∞, then secondly on the value of P_∞. Their results are compared with those from Noltink-Neppiras' incompressible approach, shown in Table 1-1. It has been shown again that if the ratio of $\frac{Q}{P_\infty}$ is greater than 1%, the incompressible results agree quite well with the compressible ones.

Nonspherical Collapsing

All the foregoing analyses assumed the spherical collapsing. But, due to the effects of pressure gradient, solid boundary and interface instability etc., the actual bubble shape (especially during the final collapse and successive rebound) are often distorted, i. e., in

a nonspherical shape.

There are basically two categories of departures from the smooth spherical shape.

One is the general deformation of the bubble shape, i. e., the shape just becomes flattened as the bubble collapses in the wall proximity and in the flow field with certain pressure gradient. Usually, the flattened side is at the higher pressure side in the pressure field and/or the off-side to the solid boundary. Sometimes, the flattened side will continue to dimple and to penetrate into and through the cavity, and to form a jet, which is called micro-jet.

This nonspherical behaviour and the formation of jet was firstly assumed by Kornfeld and Suvarov [42] as early as in 1940's. But, it was about 20 years later that this phenomenon was firstly clearly observed and its mechanism was theoretically explained using the second perturbation approach by Naude and Ellis [15]. From their analytical fluiddynamic analysis (neglecting gravity and assuming the constant pressure within the hemispherical cavity attached to the solid boundary during collapsing), a jet velocity in the order of 10^2–10^3 feet/sec was predicted. According to the spherical collapse hypothesis, the maximum collapsing pressure of a typical bubble near solid boundary is only about 100 bar which is unlikely to cause damage except for very soft aluminimum. Whereas, the nonspherical collapse hypothesis, i. e., the formation of high speed micro-jet, gives a very good explanation why the collapse of a bubble near the solid boundary can cause the damage to the material.

The numerical solutions of the motion equation for the nonspherical collapse were obtained by Plesset-Chapman [43] in 1969 and by Mitchell-Hammitt [44] in 1970. The former, which was based on the assumption of an incompressible nonviscous liquid, numerically reproduced the nonspherical collapse and the jet formation of the initially spherical vapour cavity collapsing in the solid boundary proximity; whereas the latter, which assumed an incompressible viscous liquid with pressure gradient, numerically demonstrated the flattening and consequently the jet formation of the initially spherical

cavity due to the asymmetric influence of pressure gradient.

The second sort of nonspherical deformation is the appearance of the irregular surface at the interface between gas/vapour and liquid. Usually, this is the case of the rebounding bubbles. The formation of the rough surface due to the instabilities of interface and the sphere (at the end of the collapse) will disintegrate into a number of smaller bubbles of various sizes and closely neighbouring centres. Plesset has given a detailed discussion on the instability of the plane and curvature interfaces based on Taylor's theoretical analysis. He concludes that when wall radius R becomes very small, the surface distortion amplitude oscillates at increasing frequency and amplitude, i. e., increasing instability. Therefore, for the collapsing bubble and the rebounding bubble, the distortions are mostly likely to occur at the final stage of collapse and the beginning of the rebound.

1.2.3. Acoustic Emission of Single Bubble

The acoustic emission from the cavitation bubble could be well approximated by the acoustic model where the bubble is treated as a simple sound radiator which has a spherical shape and pulsates in volume producing the acoustic wave transmitting outwards. This approximation is quite close to the actually physical phenomenon because the scale of the acoustic source, i. e., the bubble, is very small compared with the wavelength.

Acoustic Energy

Acconling to sound theory, the emitted acoustic energy E_{ac} from a simple acoustic sphere could be expressed in terms of the volumetric acceleration $\ddot{V}$ as well as the acoustic pressure $p(t)$, i. e.,

$$E_{ac}=4\pi r^2\int_0^t \frac{p^2(t)}{\rho c}dt=\frac{\rho}{4\pi c}\int_0^t \ddot{V}^2(t)dt=\frac{\rho}{4\pi c}\int_{R(0)}^{R(t)}\frac{\ddot{V}^2}{R}dR$$

Considering

$$\dot{V}=4\pi(2RR^2+R^2\dot{R})$$

E_{ac} takes following form

$$E_{ac}=\frac{4\pi\rho}{c}\int_{R(0)}^{R_{min}}\frac{(2RR^2+R^2\dot{R})^2}{R}dR$$

The total potential energy E_{pot} for a collapsing bubble with the initial radius R_0 (i. e., the maximum radius of a growing bubble from the gas nucleus) is

$$E_{pot}=\frac{4}{3}\pi R^3 P_\infty$$

where:

P_∞=surrounding pressure under which the bubble collapses

The acoustic energy emitted during bubble growth, $E_{growth\ ac}$, is very small compared with the potential energy E_{pot}. Usually,

$$\frac{E_{growth\ ac}}{E_{pot}}=\frac{8}{3}\left(\frac{2P_\infty}{3\rho c^2}\right)^{\frac{1}{2}}<1\%$$

Therefore, the acoustic emission during bubble growth phase is negligible.

The acoustic emission mainly occurs at the collapse stage. The approach evaluating the acoustic energy is suggested [3] based on that the volumetric (bubble-wall) acceleration is approximately calculated by Rayleigh's theory and the minimum radius R_{min} is determined by Noltingk-Neppiras theory. Thus,

$$\frac{E_{collapse\ ac}}{E_{pot}}=\frac{-1}{6}\left(\frac{2P_\infty}{3\rho c^2}\right)^{\frac{1}{2}}\int_1^{x_{min}}\frac{1-8x+16x^2}{x(1-x^2)^{\frac{1}{2}}}dx$$

where:

$$x=\frac{R}{R_0}$$

$$x_{min}=\frac{R_{min}}{R_0}$$

If $\frac{\rho}{P_\infty}<10\%$, considering the maximum velocity of bubble-wall evaluated by Eq.(1.2-40),

$$\frac{E_{collapse\ ac}}{E_{pot}}\approx\frac{1}{3}\left(\frac{2P_\infty}{3\rho c^2}\right)^{\frac{1}{2}}\left(\frac{R_0}{R_{min}}\right)^{\frac{3}{2}}=M_{max} \qquad (1.2\text{-}41)$$

This gives a simple and clear way to evaluate the bubble-collapsing acoustic energy in terms of maximum Mach number M_{max}. That is, if $\frac{P_v}{P_\infty}$<10% (i. e., the gas partial pressure is much less than the collapsing pressure P_∞), the portion of the energy changed into the acoustic energy in the total potential energy is approximately equal to the value of M_{max}, which is proportional to $(\frac{R_0}{R_{min}})^{\frac{3}{2}}$ and $P_\infty^{\frac{1}{2}}$ according to Eq.(1.2-40).

But, due to the effect of compressibility of liquid, the acoustic energy determined by above approach is over-estimated especially for the case of $\frac{P_v}{P_\infty}$<1% where the compressibility is not negligible and plays the function of retarding collapse as has been explained before. Some correction has been proposed [3] to improve it as shown in Figure 1-14, which is indicated by the solid curves. As an alternative approach, Zhang and the author [16] derived following formula, by introducing the $\frac{P_v}{P_\infty}$—X_{max} relation and an empirical index β, to take account of the effects of gas content (i. e., $\frac{P_v}{P_\infty}$) and liquid compressibility

$$\frac{E_{collapse\ ac}}{E_{pot}} = \frac{1}{27}\left(\frac{2P_\infty}{\rho c^2}\right)^{\frac{1}{7}}\left(\frac{P_v}{Q}\right)^{\beta}$$

where:

β=empirical index in range of $0<\beta<\frac{3}{2}$

Based on the author proposed statistical approach, which has been used throughout the long term project *Statistic Cavitation Study*, the value of β was approximately determined as

$$\beta=\frac{1}{3}$$

1.2.4. Acoustic Emission of Cavitation Bubbles

The cavitation bubbles should be treated as the multi-bubble with random parameters rather than the single bubble.

Il'ichev and Lesunovskii [17], Morozov [18] applied the *Random Pulse Train* model to the cavitation bubble acoustics. They all treated the pulses generated by the individual bubbles as random events.

In Il'ichev and Lesunovskii approach, they assumed that the event appears at a dominating periodic time interval with a stochastic distribution of zero mean value. That is, the n-th event (pulse) will appear at the time t_n

$$t_n = nT + v_n$$

where:

T=dominant time interval, at which the probability of event appearance reaches maximum

v_n=random variable with mean value of zero, describing the stochastic feature of event occurrence; and $v_n \le \frac{T}{2}$

The waveform of the pulse is also assumed as identical. Thus, the resultant spectrum reveals the feature that it is always composed of a series of strong components with frequencies of $f = \frac{n}{T}$. The physical meaning of Il'ichev-Lesunovskii assumption of a dominant period is that the cavitation bubbles collapse in a flow field which has a strong periodic pressure component. This is often observed in cavitation phenomenon which will be discussed in more detail in this chapter and following chapters.

Morozov proposed an *Generalized (Aperiodic) Random Pulse Train* model to simulate the more general situation that the cavitation bubbles collapse at a random time interval with stochastic distributions of amplitudes and durations [18].

He assumed a damping cosine curve as the approximation of the collapse pulse,

$$p(t) = p_m e^{-\frac{t}{\tau}} \cos \omega t$$

The spectrum curve of this single bubble collapse will decreases in high-frequency range at a rate of 6 dB/octave, whereas the decay in low-frequency range depends on the relation between ω and $\frac{1}{\tau}$.

For the sake of convenience, the waveform of a single bubble could be further approximated as

$$p(t)=p_m \cdot e^{\frac{-t}{\tau}}$$

The proportionality relation of the pulse amplitude (p_m) and time parameters (τ) with the maximum radius of bubble (R_{max}) is also assumed by Morozov. The individual pulse is treated as an independent event, i. e., the parameters of the pulse are independent random variables.

Using this physical model, the power spectrum $F(\omega)$ of the general random pulse train can be reduced as

$$F(\omega)=\frac{2}{T}\left\{K(\omega)+2R_e\left[\frac{|Q(\omega)|^2\Theta_\mu(\omega)}{1-\Theta_\mu(\omega)}\right]\right\} \qquad (1.2\text{-}42)$$

where:

$K(\omega)=k^2\int_{-\infty}^{+\infty}x^4|g(\omega x)|^2\cdot W_\tau(x)dx$

k =coefficient characterizing the linear relation between the amplitude e_n and the time parameter τ_n of n-th pulse, i. e., $e_n=k\tau_n$

$g(\omega x)$=complex spectrum (Fourier Transform) of the function describing the waveform of the n-th pulse.

$W_\tau(x)$=differential distribution function of the time parameter τ

$Q(\omega)=\int_{-\infty}^{+\infty}kx^2g(\omega x)W_\tau(x)dx$

$\Theta_\mu(\omega)$=characteristic function of the stochastic variable μ (i. e., time interval between two successive pulses), $\Theta_\mu(\omega)=E\left\{e^{-i\omega\mu}\right\}=\int_{-\infty}^{+\infty}W_\mu(x)e^{-i\omega x}dx$

Thus, the characteristics of the power spectrum of this general random pulse train model depends entirely on the following three stochastic factors; or in other words, the features of the power spectrum reflect the statistical characteristics of the random pulse process in respect of following three aspects.

A The spectrum $g(\omega\tau_e)$ of the individual bubble collapse pulse.

B The stochastic distribution function W_τ for the time parameter τ. Because there is a linear relation between the amplitude ε and the time parameter τ, i. e., $\varepsilon=k\tau$, and the amplitude ε is proportional to the maximum radius R_{max}, therefore, W_τ also represents the statistical distribution function of stochastic variable R_{max}, i. e., the distribution of bubble size (this is due to the mathematical theorem that if a linear relation exists between two stochastic variables, their statistical distribution functions will be geometrically similar).

C The characteristic function $\Theta_\mu(\omega)$ of the time interval μ.

It is obvious that the above three factors are distinctively different for different cavitation types and cavitation regimes. Therefore, the general expression (1.2-42) for the random pulse train model can be used to analyze the statistical features of some special cases of cavitation as follows.

Poisson Process

This is the case that the cavitation bubbles collapse in such a way that they can be entirely considered independent of each other, i. e., the statistical distribution function $W_\mu(t)$ of the time intervals has an exponential form,

$$W_\mu(t)=\frac{1}{T}e^{-\frac{t}{T}}$$

where:

T =expectation value of the stochastic variable of time interval.

The random process of the bubble-collapsing impulses with this statistical characteristics of the time interval variable is called *Poisson Process*. This is often the case that there is not the dominant periodic pressure perturbation in the flow field associated with which the cavitation bubbles collapse. Figure 1-15 shows a statistical distribution of the time interval acquired from a particular cavitation noise experiment, which agrees quite well with the Poisson process curve.

In 1969, Morozov [18] investigated this case. Considering the characteristic function Θ_x for the time interval variable with the exponential distribution

$$\Theta_x = \frac{1}{[1-i\omega T]},$$

the power spectrum of Eq.(1.2-42) can be reduced as

$$F(\omega)=\frac{2}{T}K(\omega)=\frac{2}{T}k^2\int x^4|g(\omega x)|^2W_x(x)dx \tag{1.2-43}$$

If all bubbles are identical, i. e., the same maximum radius R_{max}, thus the pulses will have the same amplitude and waveform according to the proportionality of amplitude p_m and time parameters τ with the maximum radius R_{max}. The power spectrum of the random pulse train calculated from Eq.(1.2-43) will coincide with that of the single pulse (correct to a multiplicative constant).

If the bubble maximum radius R_{max} is a stochastic variable and its value has an uniformly statistical distribution in the range of 0 to R_0. Accordingly, the distribution of τ will be uniform from the value of 0 to τ_0. The power spectrum of this stochastic pulse process can be reduced from Eq.(1.2-43) as

$$F(\omega)=\frac{2}{T}k^2\left[\frac{\tau_0^2}{5\omega^2}-\frac{1}{3\omega^4}+\frac{1}{\tau_0^2\omega^6}-\frac{1}{\tau_0^2\omega^7}\tan^{-1}\omega\tau_0\right] \tag{1.2-44}$$

For the collapse of the bubbles with the radius equal to the average value, i.e. $R=R_{av}(=\frac{R_0}{2})$ and $\tau=\tau_{av}(=\frac{1}{2}\tau_0)$, the power spectrum will be

$$F_{av}(\omega)=\frac{k^2\tau_{av}^2}{\tau_{av}^2\omega^2+1}\cdot\frac{2}{T} \tag{1.2-45}$$

Thus, the ratio, $\frac{F(\omega)}{F_{av}(\omega)}$, of the power spectrum for the bubbles with uniformly distributed radius to that for the bubbles with the value of radius R_{av} ($=\frac{R_0}{2}$), corresponding $\tau_{av}=\frac{\tau_0}{2}$, shows that

$$\lim_{\omega\to\infty}\frac{F(\omega)}{F_{av}(\omega)}=\frac{16}{7}$$

i. e., $F(\omega)_{\omega=\infty}$ is higher than $F_{av}(\omega)_{\omega=\infty}$ by 3.5 dB; when ω increases to higher level,

$$\frac{F(\omega)}{F_{av}(\omega)} \to \frac{4}{5},$$

i.e., the level of $F(\omega)$ is close to that of $F_{av}(\omega)$.

From above analysis, it could be concluded that the power spectrum for the bubble collapse of Poisson process with uniformly distributed radius from $R_{max}=0 \to R_0$, even the variance range of R_{max} is quite large, could be approximated (with an acceptable accuracy) by the power spectrum for the bubbles with the value of radius equal to R_{av} ($=\frac{R_0}{2}$).

Periodic Process

Due to various reasons, the Random Pulse Train of Poisson Process is not always the case of cavitation bubble collapse. One of the reasons is that due to the mutual influence between bubbles, the collapses and subsequent pulse emissions of the bubbles would not be entirely independent of each other. The second reason is that the mutual influence between the bubble behaviour (i. e., micro-attribution of cavitation) and the collect behaviour of the cavitation cloud (macro-attribution) and/or the flow system, as mentioned before, will give some sort of periodic nature to the bubble behaviour if there is a strong periodic fluctuation component in the cavitation cloud and/or the flow system which associates with the bubble collapses.

To take into account the influence of this periodic component, the Random Pulse Train has been modified by Morozov [18] in such a way that the stochastic variable of time interval has a normal distribution with the variation σ. Thus, when $\sigma \to 0$, the Random Pulse Train becomes an entirely periodic train with the pulses appear at the time interval exactly equal to the mean value. Therefore, the value of σ can be regarded as an index indicating the periodicity level of the random bubble-pulses.

For convenience, Morozov analyses such a random pulse train that it has identical pulses corresponding to the bubble size of average radius.

Considering the characteristic function, $\Theta_x(\omega)$, for the time interval variable with the normal distribution

$$\Theta_x(\omega)=\exp\{iT\omega-(\frac{\sigma^2\omega^2}{2})\}$$

the corresponding power spectrum can be reduced as

$$F(\omega)=\frac{2\pi\lambda}{T}\cdot\tau^2|g(\omega\tau)|^2(1+\beta) \qquad (1.2\text{-}46)$$

where:

$$\beta=\frac{\cos T\omega-e^{-\frac{\sigma^2\omega^2}{2}}}{ch\frac{\sigma^2\omega^2}{2}-\cos T\omega}$$

T =average time interval

ε_m =amplitude equal to the average value

When $\sigma\omega\gg\frac{1}{\sigma}$, $(1+\beta)\to 1$. It means that the power spectrum will coincide with that of the single bubble pulse (correct to a multiplicative constant). When $\sigma\omega\to 0$, $(1+\beta)\to\left[\frac{\sigma}{T}\right]^2$.

The ratio of $F(\omega)$ to the single-bubble power spectrum (multiplied by the average number of pulses per unit time, i. e., $n|g(\omega)|^2$), is drawn against the frequency $T\omega$ as shown in Figure 1-16. These curves represent the effect of periodicity on the similarity of both spectra. The common feature of these curves is that they all have the peak values at the frequencies of ω_m

$$\omega_m=\frac{2\pi m}{T}\ ;\ m=1,2,3,\cdots$$

It should be noticed that when the value of $\frac{\sigma}{T}$ reduces, i. e., the level of periodicity strengthens, the value of the first peak, i. e., the value of $\left[\frac{F(\omega)}{n|g(\omega)|^2}\right]_{\omega=\omega_1}$ increases. However, even for the value of $\frac{\sigma}{T}$ down to 0.2, the magnitude of the first peak is only about 4 dB (curve 1 in Figure 1-16). Curve 2 is for $\frac{\sigma}{T}=0.1$.

If the stochastic variable of the time interval meets Rayleigh's distribution, i. e.,

$$W(\mu)=\left[\frac{\mu}{v^2}\right]\exp\left[\frac{-\mu^2}{2v^2}\right]$$

where:

$v>0$

Thus, a linear relation between the expectation E and the square root of variance σ exists,

$$E=\left[\frac{\pi}{4-\pi}\right]^{\frac{1}{2}}\cdot\sigma$$

This case corresponds to

$$\frac{\sigma}{T}=0.525$$

The curve 3 (Figure 1-16) representing this case shows that there is no peak value at $\omega=\omega_1$; for $\omega\gg\frac{2\pi}{T}$, $F(\omega)$ is 3 dB higher than $n|g(\omega)|^2$; for $\omega\to 0$, $F(\omega)$ is 5 dB lower than $n|g(\omega)|^2$.

As a conclusion, it can be drawn from Morozov's analysis that the spectrum of Random Pulse Train can be approximated, correct to a multiplicative constant, by the corresponding single bubble-pulse spectrum if one of following conditions is met:

A The stochastic variable of time interval is an independent variable with an exponential distribution, i. e., it is a Poisson Process.

B The variable of time interval has the nature of stationary random process with the periodicity of certain degree, and the value of $\frac{\sigma}{T}$ is relatively large.

Author's Analysis

Actually, the distribution of bubble radius is not uniform as has been assumed by Morozov. The bubble are developed from the initial nuclei whose radius distribution has the form of power function. To consider this factor, the author has analyzed, in collaboration with Zhang, the characteristics of the power spectrum of the Random Pulse Train model (as one part of the long term project *Statistic Cavitation Study*) under following conditions:

A It is a stationary random process.

B The stochastic variable of time interval obeys the exponential distribution, i. e. the Poisson process.

C The diameter of the initial gas nuclei which grow up and become the cavitation bubbles has the statistical distribution of power function.

D A cut-off value of pulse amplitude (p_c) is introduced to screen those pulses which amplitudes are high enough to contribute to cavitation damage.

The statistical distribution of the amplitude density, w_i, for this random pulse train model was thus derived [16]. The results (Figure 1-17) show that for the range of high amplitude, the amplitude density distribution curve coincides quite well with the measured pulse height spectra from cavitating venturi test (University of Michigan) and the both curves have the same function form (power function) as well.

1.2.5. Mutual Influences Between Bubbles — Multi-bubble Behaviour

The cavitation actually is a multi-bubble behaviour rather than the single bubble behaviour. With the advance in modern technologies such as high speed data sampling, high speed cine holography, experimental simulation of multi-bubble collapse the investigation into the multi-bubble behaviour has been made possible and become one of the most interesting fields for cavitation researchers in late 1970's and 1980's.

In 1969, Tulin [45] theoretically analysed the formation of the ultra-jet on a wedge cavity being impinged by a weak shock wave, which predicted that an ultra bubble-jet would form when a bubble collapses under the affection of a weak shock wave emitted from the neighbouring bubble collapse. In 1980, Hansson and Morch [46] have studied the dynamics of cavity clusters for cylindrical and hemispherical collapses respectively. In 1986, Tomita, Shima and Sugiv reported their numerical and experimental studies on the bubble shock wave interaction [19]. Dear and Field used the two-dimensional gelatin configuration to simulate the multi-bubble collapses [20].

The results of these researches show that the mutual influences mainly take place in the form of the shock wave interaction. The main points can be summarized as follow.

A. The procedure of bubble collapse would be affected by the shock waves emitted from the adjacent collapsing bubble.

Usually the collapsing procedure is accelerated by the shock wave. Through theoretical analysis, Fujikawa et'al [54] found that the collapses of two adjacent bubbles in a compressible liquid would be more intensive than that of the single bubble.

Through the numerical analysis of the symmetrical collapse of a bubble under the shock waves with different waveforms. Shima et'al [19] found that the accelerating effect on the collapse depends on both the waveform and the initial bubble radius R_0. If the shock wave has finite energy there exists a maximum of the impulsive collapse pressure, p_{max}. In Figure 1-18, the curve of $p_{max} \sim R_0$ is drawn against the waveform of the shock waves which are shown in the bottom of the figure. The analytical expressions for the waveforms of the triangular- and exponential decay waves are respectively:

$$\begin{cases} p_\infty(t)=p_{\infty,0} \ ; \ t\le 0, t_p\le t \\ p_\infty(t)=p_{\infty,0}+p_s\dfrac{t}{t_p} \ ; \ 0\le t\le t_p \\ p_\infty(t)=p_{\infty,0}+p_s\left(\dfrac{t_q-t}{t_q-t_p}\right) \ ; \ t_p\le t\le t_q \end{cases}$$

$$\begin{cases} p_\infty(t)=p_{\infty,0} \ ; \ t<0 \\ p_\infty(t)=p_{\infty,0}+p_s\exp\left(-\dfrac{p_s t}{F_t}\right) \ ; \ 0\le t \end{cases}$$

It is readily seen that the interaction effect results in a maximum value of p_m at certain radius R_m for the case of finite-energy shock waves. With the increase of shock-wave duration , i.e. the increases of F_t or t_p respectively, the value of R_m increases and the maximum becomes higher. In short, the interaction is strengthening while the shock-wave energy increases which corresponds to the case that the adjacent collapsing bubble is

closer to and/ or emitting a stronger impulsive pressure.

B. The bubble affected by the interaction would collapse more asymmetrically.

It is experimentally found that the nonspherical motion of a collapsing bubble would be stimulated by the shock wave interaction. Usually, the side of bubble impinged by the shock wave would firstly flatten, then forms a micro-jet toward the opposite bubble-wall and finally penetrates it. Figure 1-19 shows the collapses of an air bubble (a) and a hydrogen bubble (b) under the shock waves from below (case (a)) and from right side (case (b)). The flattening and the micro-jet formation are clearly seen [19].

C. Chain Reaction Effect.

It is further found through the two-dimensional simulation of multi-bubble collapses by the gelatin figuration technology that there would be two sorts of interactions between bubbles if the cavities are spaced in some certain arrays [20].

Figure 1-20 shows the interaction of the shock waves, S , propagating upwards with a horizontal row of three cavities. The reflected waves from the cavities are identified by the arrows in frame No.2, and they overlap between cavities labelled T in frame No.3. The micro-jets are well induced by the shock wave and the jets in outer cavities are formed in a slightly divergent directions which is a general effect for the cavities with this array arrangement. The further simulations show that the closer the cavities are spaced the greater the interaction effects from the neighbouring cavities, which agrees well with other investigators' analytical and numerical analyses mentioned above.

If the three cavities are arranged in a vertical column with the shock wave, S , traveling upwards as shown in Figure 1-21, the micro-jet labelled J can be clearly seen in frame No.2. After the entire collapse (frame No.3) which is induced by the shock wave, the first cavity rebounds forming a rebound shock wave S' . The second cavity shielded from the initial shock wave S and slightly lateral compressed, starts to collapse and to produce a micro-jet when the rebound shock wave S' reaches its lower cavity-wall (frames No.4, 5 and 6).The third cavity collapses in the same way induced by the

collapse and rebound of the second cavity . Thus, the effect of the *Chain Reaction* results under this particular conditions of shock wavelength, bubble radius and spacing.

Therefore, the interaction between adjacent bubbles in a row collapsed at same time as shown in Figure 1-20 could be regarded as one basic sort of shock wave interaction which reflects the mutual influence of adjacent collapsing bubbles on each other's collapse. The second one, i.e. the chain reaction, represents a particular mutual influence of the collapsing bubble with the successive collapse of the adjacent bubble.

Some investigation even shows that if the array is arranged in a hemispherical cloud, as analysed by Hansson and Morch [46], there will be a focusingly collapsing, resulting in an increasing collapse energy and pressure at the centre of the cloud.

It should be thus concluded that the behaviour of cavitition bubbles is strongly affected by the neighbouring bubbles through the shock wave interaction effect.

1.2.6. Cavitation Erosion

Erosion is one of the most important effects of cavitation and has been intensively investigated. But so far, the mechanism of the damage to the material exposed to cavitation is still not fully understood.

However, as to the cavitation power contributing to cavitation erosion, it is commonly agreed that the damage is mainly caused by the enormous pressure induced by the violent motion of the bubble adjacent to the material. There are four kinds of impulsive pressures impinging successively on the surface of material during the collapse [19].

A. The impulsive pressure pulse developing in the liquid nearby the bubble wall.

B. The impact pressure from a liquid micro-jet formed inside the main bubble.

C. The impulsive pressure resulting from the interaction between the outward radial flow followed by the jet impact and the bubble surface contracting on solid surface.

D. The impact pressure from the rebound shock wave from the torus-like main bubble.

On the other hand, the reaction, i.e. the resistance of the material to the cavitation impulsive pressure, varies dramatically from material to material due to the different damage mechanisms which depend mainly on the surface texture, form and the material crystal structure etc. For example, the erosion mechanism of cast iron, which is quite different from those of usual ferrous alloys such as carbon steel etc, depends on both the notch action of graphite and the notch sensitivity of the matrix [21]. However, the approximate correlations between the resistant capability of material to cavitation erosion and the single property of material have been found for some common-use materials through extensively experimental investigations. But so far, there is still no a satisfactory unified formula available.

Typical Erosion Procedure

Figure 1-22 shows a typical erosion procedure called *S-shaped* curve, which can be observed in some cases depending on the properties of material, and the type , regime and intensity of cavitation etc. Usually, after an initially very small weight loss in some cases, there is a period called the incubation period (I P) during which only relatively little material is removed. Then after a certain transition period, it reaches a maximum rate of weight loss. Some investigators divide it into four stages for vibratory cavitation erosion of carbon steel [22]: A. initial period; B. incubation period; C. transition period; D. stationary period which produces the maximum mean depth of penetration rate ($MDPR_{max}$).

Some investigators [23] define the IP as the time required to obtain mean depth of penetration (MDP) of 0.1×10^{-3} in (2.54μ m). Their tests carried on the Venturi and Vibratory facilities for five common engineering materials (2024-T-4, soft 1100-0 aluminum, 1018 carbon steel, 316 stainless steel and 3% C cast iron) show that the IP increases with the hardness except for cast iron which is presumably due to the different erosion mechanism. Similarly, the maximum value of mean depth of penetration rate, $MDPR_{max}$ decreases with increased material hardness except for cast iron. It has been found that the

water temperature can strongly influence the values of $MDPR_{max}$ and IP. Under certain test condition, there is a maximum damage temperature at which the value of $MDPR_{max}$ reaches maximum. The maximum temperature for their tests (1 bar suppression pressure, tap water) is about 160°F.

Nearly all materials, even the hardest and strongest, can be damaged by cavitation. It is also found that the highly resilient materials such as the elastomer etc. have excellent resistance compared with metals, due to the "spoiling" of the collapse and jet-formation. However, general speaking, the harder the material, the more the resistance.

The approximate relations, except for cast iron, of erosion parameters $MDPR_{max}$ (or $MDPR_{\perp}$ representing the resistance capability to erosion), IP with the Hardness HB (Brinell Hardness) have be found by He-Hammitt experiments [23], to have the following forms,

$$MDPR_{\perp} = a\ HB^{n}$$

$$IP = a\ HB^{n}$$

The values of the exponents n have been experimentally determined for these materials as well.

The resistance parameters are also reasonably suggested to be correlated with the ultimate resilience, UR, due to their dimensional consistency. The failure energy per unit volume for brittle fracture can be represented by the ultimate resilience UR,

$$UR = \frac{TS^2}{2E}$$

where:

TS =ultimate tensile strength

E =elastic modulus

Then the following correlation is suggested

$$MDPR_{\perp} = a\ UR^{n}$$

Here, the value of exponent n is theoretically expected to be unity. The values (Table 1-

3) found from Venturi tests by He and Hammitt is about 1.15 very close to the theoretical expectation except for some materials. The correlation between incubation period IP and maximum erosion rate $MDPR_{max}$ is also found for some materials

$$MDPR_{max} = a\ IP^{n}$$

Here, the values of exponent n are experimentally found as 0.93 and 0.95 for vibratory and venturi results respectively, which are very close to the theoretically expected value (n = 1). Of course, these values, derived from their particular tests, might not be generally valid.

Cavitation Erosion Prediction

Due to the demands for more reliable machine performance and for more power intensity in some particular applications such as the liquid-propellent rocket pumps, the conventional prediction approach using the experience with the similar machine to indicate the suitability of a new machine is no longer satisfactory, and a quantitative prediction is thus required.

As the basic mechanism of cavitation damage to the material is still not well understood, no existing physical model can directly guide the establishment of the prediction approach. However, it is possible to establish the prediction approach alternatively by evaluating some easily and quickly measurable attributions of the cavitation then correlating these measured data with the measured damage parameters. The cavitation noise seems to be one of these suitable attributions. Thus, since 1970's, some meaningful contributions based on above principle have been done by P. A. Lush and S. P. Hutton [47], F. G. Hammitt [27] etc., producing some useful correlations between cavitation noise level and damage rate for some particular applications (pump, venturi etc.). However, due to the complexity of the problem, at present a generalized accurate correlation has not been obtained.

One of these early approaches is to establish the correlation between the measured

area of the bubble-collapse pressure spectrum and the measured damage rate ***MDPR***. The best fit relation is obtained in following form

$$MDPR = c\,(spectrum\ area)^{\frac{1}{n}}$$

where:

c =empirical constant

n =exponents, n=5 for high-intensity tests; n=1 for lower-intensity tests

A term of *Cavitation Erosion Efficiency*, η_c, is also defined as the ratio of the power operative in the erosion process (I_{ero}) to the power of cavitation bubble collapsing impulses (I_{cav}). According to many investigations, the power involved in damage, I_{ero} , can be expressed in terms of an ultimate resilience UR if the failures are of a brittle (rather than a ductile) nature. Thus,

$$\eta_c = \frac{I_{ero}}{I_{cav}}$$

where:

I_{ero} =the power operative in the erosion process, which is proportional to $MDPR_{max} \cdot UR$

In 1982, M. K. De and F. G. Hammitt [48] proposed an improved approach for the venturi test. The acoustic energy E emitted from bubble collapse is evaluated by

$$E = \frac{1}{\rho c}\int_0^{\tau} p^2(t)\,dt$$

Then the distribution curve of acoustic energy emitted from cavitation bubble collapses can be obtained

$$N = N(E)$$

where:

N =number of bubbles emitting the acoustic energy equal or great than E

Thus, the acoustic power of cavitation I_{cav}, i. e., the average acoustic energy per unit area per unit time during the test period T_s, can be calculated

$$I_{cm}=\frac{1}{T_s}\sum_{E_c}^{E_m}E\frac{dN(E)}{dE}$$

where:

E_c =cut off value of E

E_m =maximum value of E during T_s

The value of η_c can be achieved,

$$\eta_c=\frac{MDPR_{max}\cdot UR}{\frac{1}{T_s}\sum_{E_c}^{E_m}E\frac{dN(E)}{dE}}$$

The values of η_c for various materials in U-M (University of Michigan, USA) venturi test are shown in Table 1-4.

Therefore, the accurate evaluation of the acoustic power of cavitation becomes a vital step towards the successful prediction of cavitation erosion. As one of the efforts, the author has analytically analysed, in collabration with Zhang, some stochastic characteristics of the cavitation acoustic power concerning the erosion [16]. The analysis is based on the assumptions that the distribution function of the nuclius radii has a power function and the waveform of the collapsing impulsive pressure is approximated as the first pulsation of the collapsing impulse with the decay of exponential form. The results show that the statistical distribution of the acoustic energy emitted from collapsing bubbles has the form of power function. For a given acoustic energy distribution and a certain test time period, the total acoustic energy depends on the number of collapsing bubbles M. Therefore, the damage to the material depends on the total number of collapsing bubbles M, which is also a stochastic variable. If the time interval between successive events (collapsing pulses) is assumed to obey the exponential law, i. e., Poisson process (independent stochastic process), the distribution, $W_M(X)$, of the required time period for completing M number of collapsing bubbles should have a gamma distribution form, i. e.,

$$W_M(X)=\frac{\lambda^M}{\Gamma(M)}X^{M-1}e^{-\lambda X},\ (X>0)$$

where:

$\lambda^{-1}=\overline{\Delta T}$

$\overline{\Delta T}$ =average time interval

The above equation shows that when the value of M increase, the distribution curve of $W_M(x)$ spreads more widely with a smaller peak at $X=\frac{M-1}{\lambda}=M\cdot\overline{\Delta T}$ as shown in Figure 1-23. This explains quite well the fact that the cavitation damage test results, if not treated statistically, are always quite scattered even under carefully controlled test conditions.

1.3. Cavitation Caused Pressure Pulsation

The huge-amplitude pressure pulsations of relatively low frequencies are often observed in a flow system when cavitation appears especially for some cavitation regimes. It is one of the cavitation effects identified much later than the discovery of cavitation phenomenon. One example of this phenomenon is the pressure pulsations observed by Oba et'al [49] in an orifice cavitating flow in 1982.

In 1981, the author et'al [24] investigated this phenomenon on University of Michigan cavitating venturi, as one part of the long term project *Statistic Cavitation Study*, and found that it is some sort of the interaction between the cavitation cloud and the surrounding flow field. As has been mentioned, in addition to the mutual influence between cavitation bubbles themselves, there is also the mutual influence between the collective of the bubbles (i. e., cavitation cloud) and the flow field. That is, the behaviour of the cavitation bubbles is dominated by the properties of the surrounding flow field such as its pressure variations in respect of time and spatial position, the flow velocity etc.; whereas, the existence of the cavitation bubbles and their collect properties (such as the high elasticity of the cloud) would inversely give a strong influence on the nature of the flow field such as the induced pressure oscillation, instability of flow and increased resistance of flow.

1.3.1. Description of Phenomenon

A typical example of cavitation caused pressure pulsation is the huge pressure oscillation in the draft tube of some hydraulic turbines suffering from the vortex core cavitation [25,26]. The mode, basic frequency and its harmonics of this pulsation vary with the operation conditions such as unit speed n_1', unit discharge Q_1' and cavitation number σ. Usually, when cavitation appears, a low-frequency pulsation pressure component occurs. Due to the complexity of the cavitation cloud in the draft tube --- its three dimensional shape (sometimes a spiral rope, sometimes an axially symmetric vortex core, ...) and its complex motion form (rotation, swirling etc.), the pulsation also presents a complex

appearance in respect of frequency, mode and stability, which inversely exhibits a complex influence on the bubble behaviour such as the intensity of collapse, periodicity of growth and collapse. For some extreme cases, the frequencies of the pulsation coincide with the natural frequencies of the machine house structure and/or whole flow system. Thus, a resonance results producing structure vibration even power oscillation.

This phenomenon is often observed at other cavitating flow systems as well, such as venturi- and orifice flows and transverse flow past a cylinder.

1.3.2. Investigation Origin --- Author's Understanding of Cavitation

Through the foregoing review of cavitation in various fields relevant to the subject, the author's viewpoint of the cavitation phenomenon, which underlies the long-term research project and guides its research direction, can be briefly summarized as follows.

Micro Attribution of Cavitation

The individual bubble behaviour (nucleation, growth, collapse, nonsymmetrical collapse, micro-jet, rebound, shock wave emission, and their mutual influences such as shock wave interaction, chain reaction etc.) has been categorized as *Micro Attribution of Cavitation* by the author [24] due to its micro scale in respect of time and spatial dimensions.

The pressure pulsations emitted from these micro behaviours have their own distinctive features in the waveform and the stochasticity accordingly. Subsequently, so do their acoustic power spectra.

Macro Attribution of Cavitation

Once cavitation occurs there are many bubbles appearing rather than a single bubble and the liquid becomes a bubbly (vapour/gas-liquid two phase) medium. The properties of the medium is thus changed and usually a Cavitation Cloud is formed. The new properties of the bubbly medium or the cavitation cloud (such as the low wave propagation

speed) actually reflect the collective behaviour of the bubbles. Therefore, the phenomenon associated with cavitation cloud such as the low-frequency fluctuation has been named as *Macro Attribution of Cavitation* by the author [24]. Thus, the waveform and the stochasticity of the (macro) pressure fluctuations and their power spectra are all have their own distinctive features in contrast with those of the micro pressure pulsations (such as the collapsing pulses etc.).

Mutual Influences

There are basically two sorts of mutual influences involved in cavitation phenomenon.

A Mutual influence between bubble-bubble (shock wave interaction), bubble-solid boundary, i. e., the mutual interactions in the (micro) scale of the bubble size.

B Mutual influence between the collective behaviour of bubbles and the flow field, i. e., the mutual interaction in the macro scale.

Stochasticity

The occurrence of cavitation usually introduces some sort of local or system pressure oscillation, i.e., two-phase transient flow (in the form of stable oscillation) into the flow system. The cavitation bubbles in such a cavitating transient flow should be considered as stochastic multi-bubbles due to two factors [24]: one is the stochastic distribution of the original bubble parameters such as the nucleus spectrum etc.; the other is the mutual influences of bubble-bubble, bubble-boundary and bubbles-flow field, which all have the stochastic natures. Thus, the resultant stochasticity of bubbles presents in following three aspects:

A The diameter of the nucleus, the speed of growth and collapse, nonsphericity of collapse and the intensity of the resultant impulsive wave, all being stochastic variables for different bubbles.

B The position where the same event occurs for different bubbles being a stochastic variable.

C At a given position, the time of occurrence of the same event for different bubbles being a stochastic variable.

Classification of Cavitation Pulsations

All the pressure pulsations involved in cavitating flow, such as the macro- and micro pulsations and the flow noise (sometimes called white noise), should be further categorized according to their own distinctive features in terms of the waveform and stochasticity, which reflect their substantially physical natures. It has been realized that this classification would give a further insight into the cavitation phenomenon in respect of the pressure pulsations. This work has been carried out by the author et'al [24] on the University of Michigan cavitating venturi and some results have been obtained. The overall pressure pulsations involved in venturi cavitating flow consist of three basic components according to their waveform features and statistical characteristics. Their appearances and intensities have strong correlations with the flow conditions and cavtation regimes. They are:

A Basic flow noise.

Besides the usual turbulent noise, there are other factors such as the effect of finite number of impeller or casing blades (driving pump) etc. contributing to the overall flow noise. These can be treated as background white noise.

B Cavitation pulses --- Micro pulsations.

Formation, development, collapse and oscillation of entrained bubbles (primarily collapse) all cause these pressure pulses, which are referred as *Cavitation Bubble Pulses*.

C Low-frequency (pressure) fluctuations --- Macro pulsations.

These are the pulsations caused by the collective properties of cavitation bubbles. i. e., cavitation cloud, rather than the individual bubble behaviour. These fluctuations usually appear in the cavitation cloud and/or whole flow system and always have spatially large scale and relatively low frequencies in contrast with the cavitation bubble pulses.

The *Cavitation Associated Fluctuations* categorized as C above is thus investigated based on the author's understandings of cavitation.

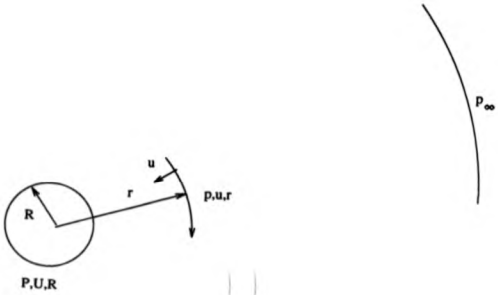

Figure 1-1 Rayleigh Analysis

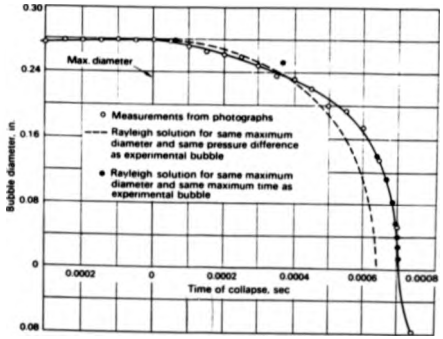

Figure 1-2. Rayleigh Analysis: Collapsing Time for an Empty Bubble

[Knapp and Hollander]

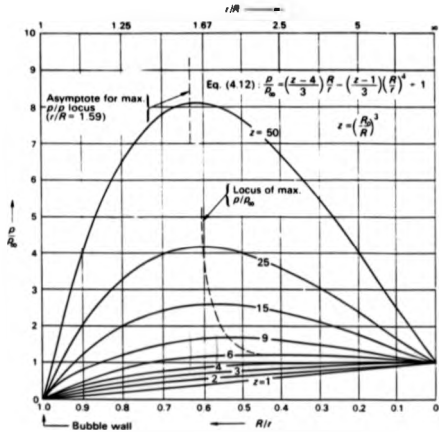

Figure 1-3. Rayleigh Analysis: Pressure Distribution in the Liquid Surrounding a Collapsing Empty Bubble

[Knapp, Daily and Hammitt]

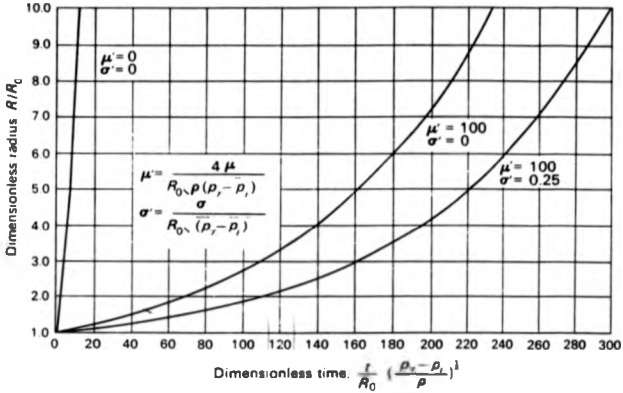

Figure 1-4. Growth of a Spherical Bubble in an Incompressible Liquid with and without Viscosity and Surface Tension

[Poritsky]

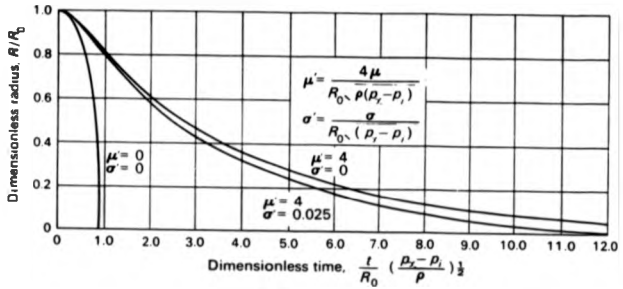

Figure 1-5. Collapse of a Spherical Bubble in an Incompressible Liquid with and without Surface Tension

[Poritsky]

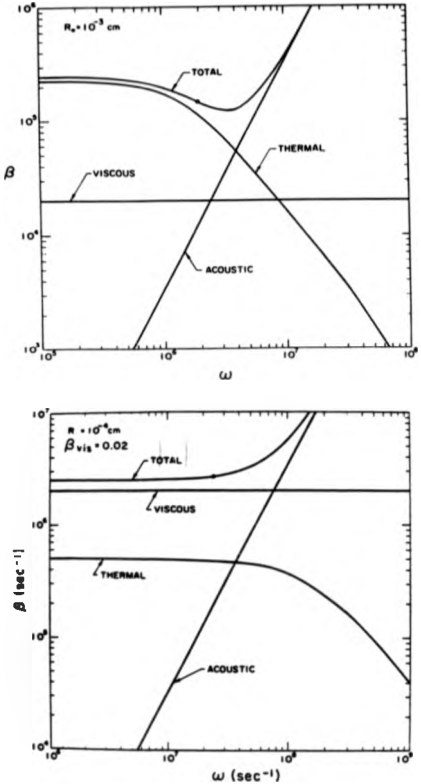

Figure 1-6. Damping Constant β for Small-amplitude Oscillation of Air Bubble in Water as a Function of Driving Frequency

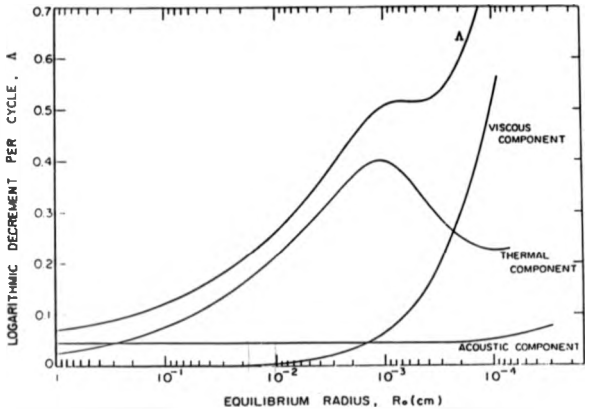

Figure 1-7. Logarithmic Decrement Per Cycle for Small-amplitude Free Oscillation of an Air Bubble in Water as a Function of Equilibrium Radius R_0

[Chapman and Plesset]

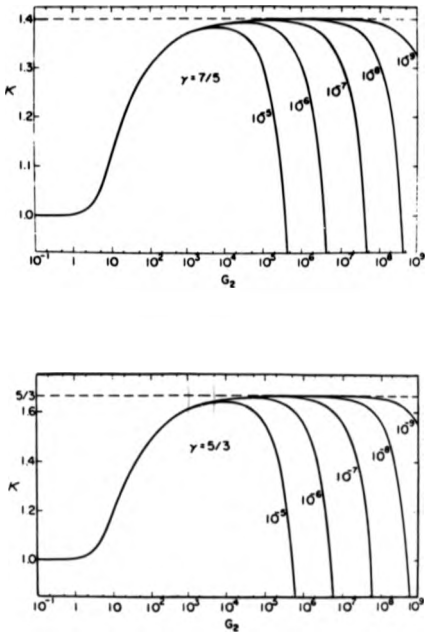

Figure 1-8. Variation of Effective Polytropic Exponent k for Diatomic Gas ($\gamma=\frac{7}{5}$) and Monatomic Gas ($\gamma=\frac{5}{3}$) with G_1 and G_2

[Prosperetti]

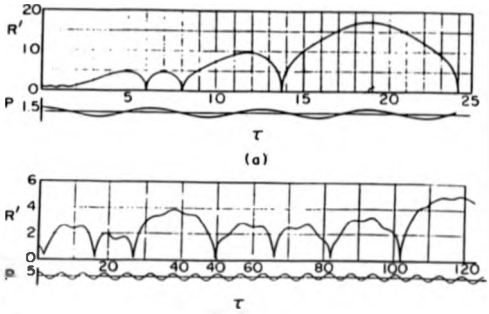

Figure 1-9. Numerical Results for Transient Motion of Gas Bubble in Oscillating Pressure Field ($\tau=\omega t$, $R'=\frac{R}{R_0}$):

(a) $\eta=1.5$, $\frac{\omega}{\omega_0}=0.154$ (b) $\eta=5$, $\frac{\omega}{\omega_0}=1.54$

[Borotnikova and Soloukin]

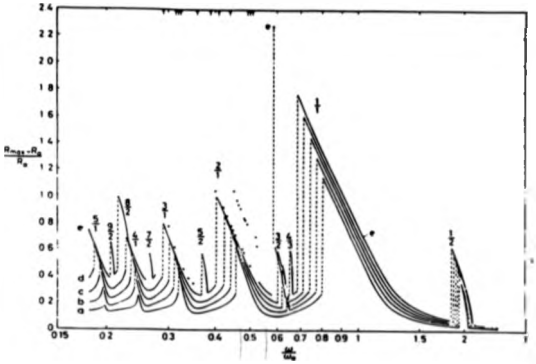

Figure 1-10. Response Curves for Steady Oscillations of an Air bubble of Equilibrium $R_0=10^{-3}$ (cm) in Water as a Function of Ratio of Driving Frequency ω to Natural Frequency ω_0: (a) $\eta=0.4$ (b) $\eta=0.5$ (c) $\eta=0.6$ (d) $\eta=0.7$ (e) $\eta=0.8$

[Lauterborn]

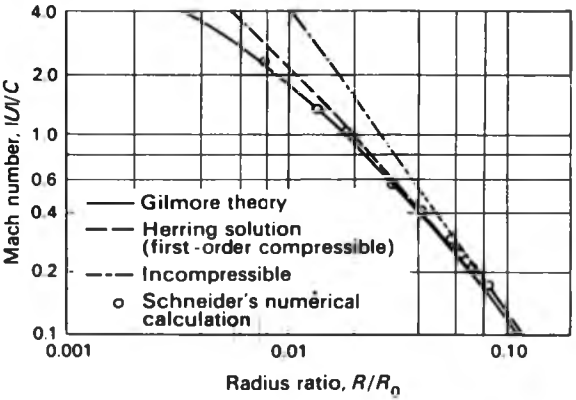

Figure 1-11. Comparison of Incompressible (Rayleigh), First-order Compressible (Herring/Trilling) and Gilmore's Results. Compressible Liquid without Viscosity and Surface Tension.

[Gilmore]

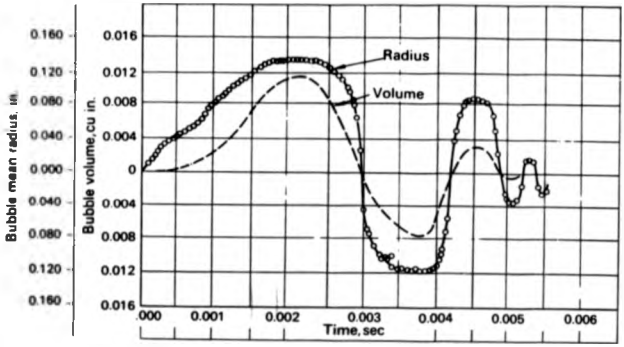

Figure 1-12. Size versus Time of a Collapsing and Rebounding Bubble

[Knapp and Hollander]

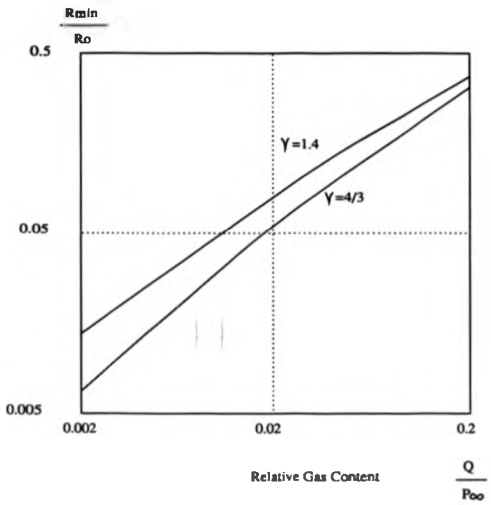

Figure 1-13. Variation of Minimum Radius with Relative Gas Content $\frac{Q}{P_\infty}$

[Ross]

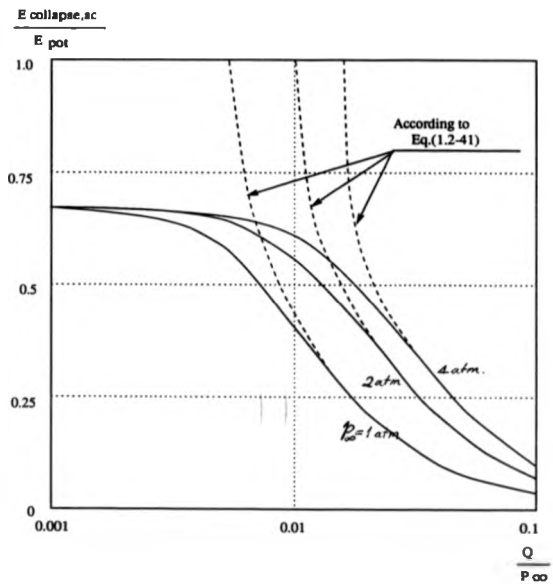

Figure 1-14. The Relation of $\frac{E_{collapse,ac}}{E_{pot}}$ vs. $\frac{Q}{P_\infty}$

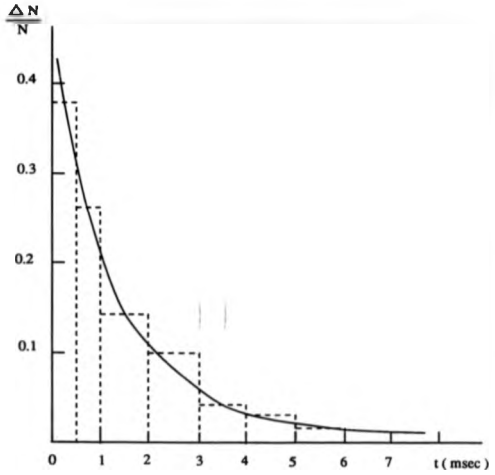

Figure 1-15. Statistical Distribution of Time Interval for a Random Pulse Train of Poisson Process

[Morozov]

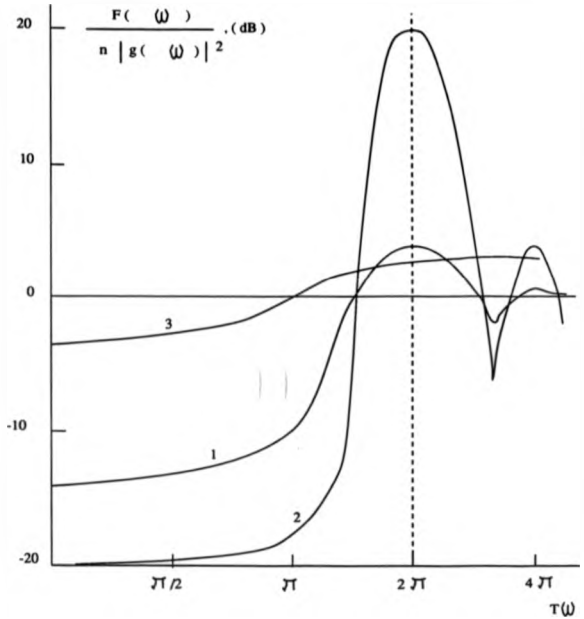

Figure 1-16. Influence of Periodicity on Power Spectra

[Morozov]

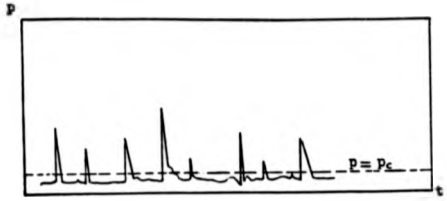

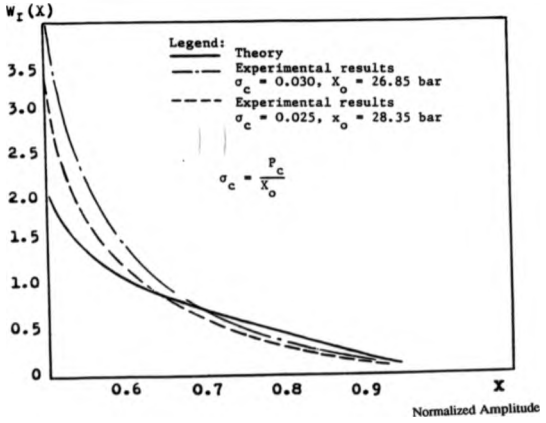

Figure 1-17. Comparison of Theoretical Analysis of Spectra of Pulse Amplitude with Experimental Results from U-M venturi

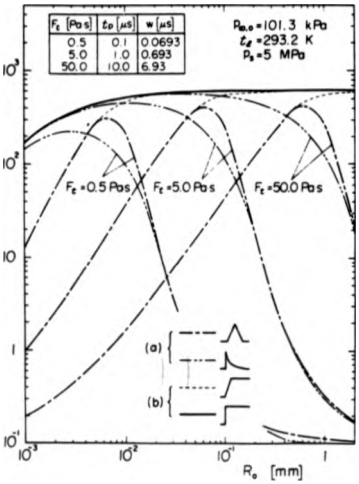

Figure 1-18. Variation of Maximum Collapse Pressure P_m Resulting from the Interaction of Different Shock Waves, under Different Initial Radius.

[Tomita, Shima and Sugiu]

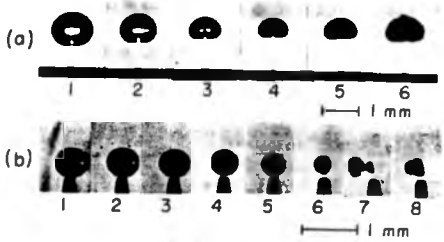

Figure 1-19. Flattening and Micro-jet Formation of Air (a) and Hydrogen (b) Bubble Impinged by Shock Waves.

[Tomita, Shima and Sugiu]

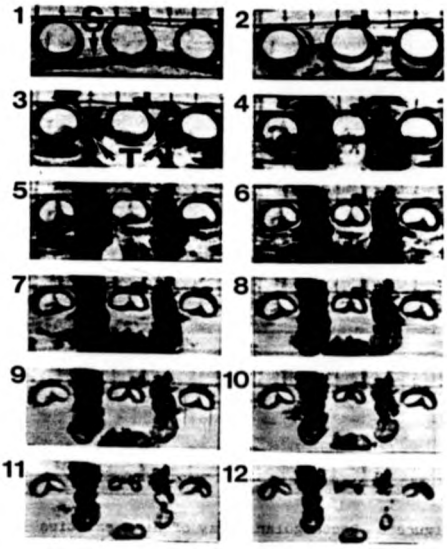

Figure 1-20. Three Cavities (diameter 3 mm, 6 mm apart) Parallel to the Shock Wave S.
Interframe Time = 0.96 μ s.

[Dear and Field]

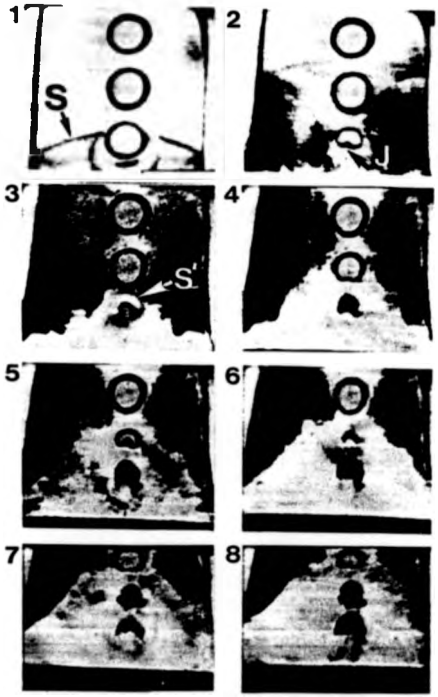

Figure 1-21. Chain Reaction Effect of Shock Wave Interaction.
Cavity Diameter = 3 mm, Interframe Time=4.25 μ s.

[Dear and Field]

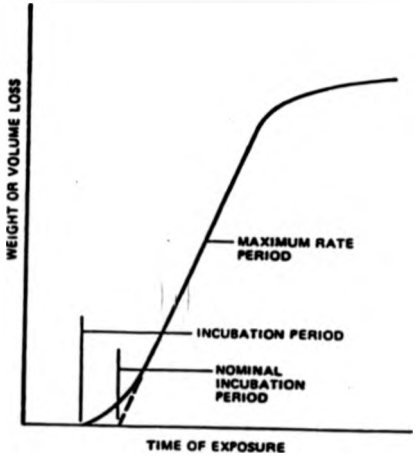

Figure 1-22. Typical Erosion Curve with S-shape

[He and Hammitt]

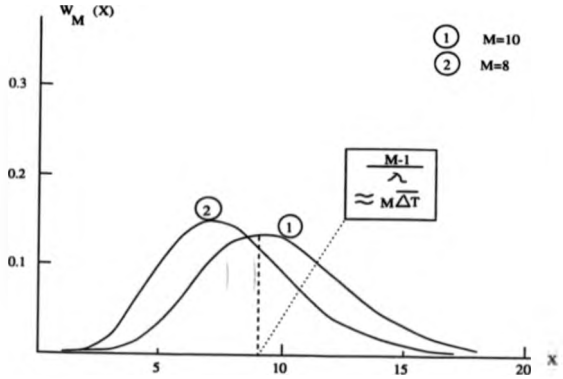

Figure 1-23. Statistical Distribution of $W_M(X)$

$\frac{Q}{P_{\infty}}$	Noltingk-Neppiras' Results (incompressible)	Hickling-Plesset Results (compressible)	
		P_{∞}=1 bar	P_{∞}=10 bar
	Minimum (Relative) Radius		
0.10	0.262	0.28	
0.010	0.047	0.060	0.074
0.0010	0.0069	0.018	0.025
10^{-4}	0.0010	0.006	0.009
10^{-5}			0.0035

Table 1-1. Comparison of Incompressible- with Compressible Approach

[Ross]

A comparison of the exponents n of the relation $MDPR_{max}^{-1} = aHB^n$

Material	*Venturi run*	*Vibratory run*
Al 1100-0 Al 2024-T-4 1018 carbon steel 316 stainless steel	2.97	3.64 (1.78×10^{-3} in)
Al 1100-0 Al 2024-T-4 Cast iron (3% C)	1.47	1.62 (1×10^{-3} in) 1.80 (1.38×10^{-3} in)

A comparison of the exponents n of the relation $LP = aHB^n$

Material	*Venturi run*[a]	*Material*	*Vibratory run*[b]
Al 1100-0 1018 carbon steel 316 stainless steel Al 2024-T-4	3.56	Al 1100-0 1018 carbon steel 316 stainless steel	2.70 (1×10^{-3} in)
		Al 1100-0 Al 2024-T-4 Cast iron (3% C)	1.76 (1×10^{-3} in)

[a] $V = 49$ m s^{-1}; 80 °F.
[b] Amplitude, 1×10^{-3} in; 80 °F.

Table 1-2. Test Values of Exponents n

[He and Hammitt]

A comparison of the exponents n of the relation $MDPR_{max}^{-1} = aUR^n$

Material	*Venturi run*[a]	*Material*	*Vibratory run*[b]
Al 1100-0 316 stainless steel Cast iron (3% C) 1018 carbon steel	1.15	Al 1100-0 316 stainless steel Cast iron (3% C)	1.54 (1×10^{-3} in)
Al 1100-0 Al 2024-T-4	0.21	Al 1100-0 Al 2024-T-4	0.32 (1×10^{-3} in) 0.18 (1.38×10^{-3} in) 0.61 (1.78×10^{-3} in)

[a] $V = 49$ m s^{-1}; 80 °F.
[b] 80 °F.

Table 1-3 Test Values of Exponents n

[He and Hammitt]

Material	UR psi	MDPRmax μ m/hr	Erosion Power watts/m^2 x10^{-6}	Efficiency η_c x10^{-12}
Stainless steel (316)	114.0	0.34	73.2	7.7
Carbon steel (1018)	81.7	0.46	71.8	7.6
Aluminum (1100-0)	6.1	55.88	646.8	68.1
Aluminuum (2024-T4)	170.0	4.90	1582.7	166.6
Cast iron	34.1	1.42	92.0	9.7

Table 1-4. Cavitation Erosion Efficiency η_c from U-M Venturi Test

2. EXPERIMENTAL METHOD

2.1. Cavitation Venturi Loop

No really standard device has yet been developed for flowing cavitation test, and a variety of devices have been used. One of the main facilities is the venturi test which includes all sorts of devices employing a flow restriction to convert pressure into kinetic head, creating a cavitating region when the static pressure falls to the level of the vapour pressure. For the cavitation erosion investigation, some relatively standard venturis have been used. Among them, the venturi at the *Cavitation and Multiphase Flow Laboratory* (University of Michigan) is a high speed cavitating loop which can model closely the usual flow conditions found in hydraulic machines and has been used for many fundamental researches on erosion and bubble dynamics. The throat velocity ranges from 17 m/s to 70 m/s and cavitation condition ranges from inception to fully developed, i. e., extending well into the diffuser section.

2.1.1. System Configuration

The cavitation test loop is shown in Figure 2-1. It can be divided into three major parts: deaeration system, venturi closed-loop, and data acquisition and processing system. The cylindrical plexiglass venturi with pressure transducer and damage specimen is shown in Figure 2-2 and the facility schematic is shown in Figure 2-3. After preprocessing, signals received by the transducer (rise time : 3.0 μ sec; resonant frequency: 130 kHz) are converted into digital signals by the analog-digital (A/D) converter and sent to the PDP-11/23 real time computer. Results from this system can also be sent to the Amdah 270 computer in the Michigan Computer Centre for further processing; or converted into analog signals by the digital-analog (D/A) converter to be displayed by oscilloscope; or printed directly.

A set of programs including signal sampling and processing have been especially designed by the author [24] for this research, allowing rapid experimentation, and

automatic and accurate processing of data. All the required information is stored in memory in advance. After in-putting fundamental independent parameters such as water temperature, downstream pressure, and pressure difference across flow orifice, the data acquisition and processing system starts sampling and processing the data. It then outputs the results such as the statistical distribution curves and spectrum analyses.

2.1.2. Venturi Test Section

The geometry of the University of Michigan venturi test section for a nominal $\frac{1}{2}$ in. throat diameter involving a 6 degree angle nozzle and a diffuser section separated by a cylindrical throat (4.60 L/D) is shown in Figure 2-2. Test fluid has been limited to water not exceeding the temperature of 90°C.

Figure 2-4 shows a typical normalized wall axial static-pressure profile for *Sonic Initiation*, i. e., the cavitation inception detected through the first detectable sound by stethoscope or hydrophone [27]. The sonic initiation differs from *Visible Initiation* which involves a continuous ring of cavitation at the exit of the throat where cavitation firstly appears.

The effect of throat Reynolds number (R_{e_t}) on the cavitation number (σ_c) for different cavitation conditions including the sonic initiation, the cavitation regime extending to first mark (1.75 in. downstream from the throat exit), the cavitation regime extending to second mark (3.5 in. downstream from the throat exit) is shown in Figure 2-5 [27], where

$$\sigma_c = \frac{p_{min} - p_v}{\frac{1}{2}\rho V^2}$$

where:

p_{min}=minimum throat pressure

It can be seen clearly that the effect of Reynolds number (here, i.e. the velocity) upon the cavitation number reduces remarkably with the increase of the cavitation

degree. To avoid this effect, the velocity was thus remained constant for each test in this research.

2.1.3. Instrumentation

Velocity Measurement

The throat velocity is calculated from the measured flow rate by the orifice device and the manometer in the venturi loop shown in Figure 2-3 (a). The orifice plate No. T478211 with the bore of 1.599 in. is installed in the 2 in. pipe stretch. It is calibrated before hand and its calibration curve is shown in Figure 2-6. Thus, the throat velocity V_{throat} can be calculated,

$$V_{throat}=\frac{Q}{A_{throat}}=\frac{Q(GPM)}{(448)\times(1.42\times10^{-2}ft^2)},\ (ft/sec)$$

where:

Q=flow rate read from calibration curve (Fig.2-6) according to the manometer reading, ΔH_{Hg}, i. e., $\Delta H_{H_2O}(=12.5\,\Delta H_{Hg})\rightarrow Q(GPM)$

A_{throat}=cross section area of throat ($1.42\times10^{-2}\,ft^2$)

Pressure Measurement

There is a high accurate Heise pressure gauge on the downstream stretch of the venturi to measure the static pressure as a reference pressure, p_r, for the whole system as shown in Figure 2-3 (a). It is also used as the pressure for calculating the cavitation number σ

$$\sigma=\frac{p_r-p_v}{\frac{1}{2}\rho V_{throat}}$$

The instant pressure is measured by the high response-frequency transducer (Kistler Model 601 A).

Temperature Measurement

It is assumed that the temperature is uniform along the loop. Therefore, only one thermocouple located at the downstream of the venturi is used to measure the temperature as shown in Fig. 2-3 (a). The reading is treated as the temperature of the medium in the system.

2.1.4. Data Acquisition System

The configuration of the PDP 11/23 computer based data acquisition and processing system including the signal pre-processing devices is shown in Figure 2-3 (b).

Pressure Transducer

According to Ivany's report [28], the typical maximum size of the bubbles in the venturi is about 60 mils (1.52 mm), and the corresponding risetime of shock wave is in the range of 1–10μs. The diameter of the micro-jet emitted from the asymmetrically collapsing bubbles is in the range of $\frac{1}{10}$ to $\frac{1}{100}$ of the maximum bubble radius according to Kling-Hammitt investigation [29]. Thus, to sample the instant point pressure of the pulses emitted from these cavitation bubbles, the transducer should be a very tiny (at least the diameter $\leq$ 1 mm) with high response frequency ($\geq$ 1 MHz). But, at that time, the only commercial transducer most suitable to this research was the Kistler Model 601 A.

The Kistler Model 601 A is a piezoelectric probe with the 3.0 μs risetime, 130 kHz resonant frequency, and 0.2 in. (5.08 mm) diameter of diaphragm. According to the manufacturer's calibration, it can measure the peak pressure in venturi up to 500 psi (34.4 bar). The detailed characteristics of it is listed in Table 2-1.

The calibration done by De also show that it can respond quite well to a real shock wave emitted from the electrical spark generated underwater-bubble and the deformation of the recorded waveform (Figure 2-7) with the charge amplifier is quite acceptable.

System Functions

The configuration of the data acquisition system is shown in Figure 2-3 (b). The pre-processing device consists of the Kistler 556 charge amplifier and the AP-220-5 multi-function filter. The analogue signals sent from the transducer Kistler 601 A are firstly pre-treated here. They can be amplified up to the level of 5 voltage compatible with the A/D converter. The analogue filter can work either on high-pass or low-pass mode to preliminarily screen the useful signals from the other signals such as the background noise which has the frequency up to the order of 10 kHz. The fast analogue-digital converter DT-1762 is used to digitize the preliminarily treated analogue signals. The input impedance of the converter is up to about 100 $M\Omega$ resulting in little distortion of the input signals.

The central processor unit is a DEC-LSI-11/23 microcomputer. The sampling rate, fore- and/or background working mode, and the procedure of data processing etc. all can be programmably controlled. The data are stored in a CRDS-MF-11 floppy disk system. The results can be displayed on the oscilloscope via a digital-analogue (D/A) converter DT-2766 or directly printed on the DEC-LA-36 terminal. For further processing, the data can also be sent to the University of Michigan computer centre via the Michigan Terminal System (MTS).

Software Design

A set of data-acquisition and processing computer programs in Fortran IV are specially designed by the author [24] for this research, incorporating the callable subroutines written in PDP-11 assembler for programmable clock, A/D and D/A converters; and the RT-11 system laboratory utilities. The main program flow chart is shown in Figure 2-8.

The determination of the reference pressure level, which is used as the elementary parameter for the data processing such as the calculation of the relative pressure value of the collapsing pulses for a given sample of pressure signals, is a difficult task due to the

superimposition of various pressure components such as the flow noise, bubble collapsing impulses etc. In order to eliminate the interference of the statistical asymmetry of the bubble collapsing impulses, which will be discussed in 3.1.1., a special iteration approach has been created to evaluate this quasi-steady pressure value which is used as the reference pressure. That is, all the recorded digital values of $p_1, p_2, p_3, \ldots, p_n$ in the pressure sample of size n are firstly taken to get the initial value of the reference pressure P_1,

$$P_1=\frac{p_1+p_2+\cdots+p_n}{n}$$

Then, the relative values of $p_1, p_2, \ldots, p_n$ referring to the first approximation of the reference pressure P_1 will be

$$p_1-P_1, p_2-P_1, \ldots, p_n-P_1$$

Thus, the absolute values, $|p_1-P_1|, |p_2-P_1|, \ldots, |p_n-P_1|$, of these n relative pressures are compared with a pre-determined threshold value $p_{threash}$ (>0) to identify those pressures whose absolute values of the relative pressures are greater than $p_{threash}$ and then the biggest m pressures of them are excluded from the sample. The remains ($n-m$ pressures in the sample) are used to get the second approximation of the reference pressure P_2. Here, m is a pre-set number much smaller than n (i.e. $m \ll n$). Then, according to a pre-set tolerance value P_{tol} (>0), the absolute difference between P_1 and P_2, i. e., $|P_2-P_1|$, is checked to see if

$$|P_2-P_1| \le P_{tol}$$

If not, a second group of m pressure values whose absolute values of the relative pressures (referring to the second approximation of the reference pressure P_2) are greater than $p_{threash}$ are excluded from the sample and the remains ($n-2m$ pressures) are used to get the third approximation P_3. This procedure is repeated k times until

$$|P_k-P_{k-1}| \le P_{tol}$$

is satisfied. The value of P_k is then used as the reference pressure for this sample.

2.2. Test Method

2.2.1. Test Procedure

The two circulations of the venturi facility, i. e. the deaeration- and testing circulations, are respectively driven by an auxiliary (aurora) pump and a large speed-variable pump as shown in Figure 2-3 (a). The main system can be pressurized through the surge tank attached to the inlet of the low-pressure tank. The flow-rate, as well as the system pressure, can be changed through the speed variation of the main driving pump. The water is pre-deaerated in the deaeration circulation before test. The coil-heater in the deaeration circulation is used to heat the water which is then sprayed into the vacuum tank held at partial vacuum by the water ejector and the mechanical vacuum pump for deaeration.

To start a test, the main loop is firstly filled up with the Ann Arbor tap water. Then it is pressured to 1 kg/cm^2 and the air is expelled from the system by opening the vent on the top of the loop and running the main pump at a half-speed for 10 to 30 minutes until the air bubbles are gone. To maintain the required test temperature, here $T=80°F$ ($26.7°C$), the flow rate of the cooling water in the cooler of the low-pressure tank should be regulated accordingly. The deaeration is performed by running the auxiliary pump with the large pump operating at slow speed. For $T=80°F$, the deaeration needs one hour with the vacuum tank pressure remaining at 30 psig ($0.0762 kgf/cm^2$) approximately. The air content (volume fraction) α is measured by the Van Slyke apparatus. For this study, α is maintained at about 50% of the saturation STP (1.7% Vol.), i. e. α=0.8% at 1 bar pressure. After deaeration, the deaeration circulation is shut off from the main test circulation and then the system is ready for test.

2.2.2. Test Range

For this study, the deaerated (α=0.8% at 1 bar) Ann Arbor tap water was used through out the study. Temperature was remained as constant at $T=26.7°C$.

For a given test condition, the venturi throat velocity V_{throat} was constant, for say 38.4m/s, remaining a constant throat Reynolds number $R_{e,t}$ to eliminate the effect of $R_{e,t}$ on the cavitation number σ as well as the inception. Only the downstream reference pressure p_r was changed to provide changes in the cavitation number σ, which is here defined as

$$\sigma=\frac{p_r-p_v}{\frac{1}{2}\rho V_{throat}^2}$$

Thus, for each test, the influences of turbulence, Reynolds number and the finite number of pump blades were all remaining constant while σ was changed to cover the whole cavitation range from non-cavitation to fully developed cavitation. Therefore, only the influence of σ and the consequent change of cavitation cloud were observed. The tests have covered the velocity ranged from 28 to 38.4 m/s.

2.2.3. Sampling Parameters

Sampling Rate

For the spectrum analysis of the low-frequency fluctuations, the *Fast Discrete Fourier Transformation (DFT)* analyses were performed for the sampled digital signals. The DFT for waveform $f(t)$ with finite sampling number N is

$$\bar{F}_m=\bar{F}\left(\frac{j2\pi m}{NT}\right)=\sum_{n=0}^{N-1} f_n e^{\frac{-j(2\pi mn)}{N}};\quad m=0,1,2,\ldots,n-1$$

where:

N =number of sampling points

T =time interval between successive sampling points

Thus, the angular frequency, ω_m, of the m th harmonic is

$$\omega_m(=2\pi f_m)=2\pi\frac{m}{NT}$$

According to Nyquist sampling theorem, the maximum frequency f_{max} of harmonic components analysed by the DFT must not exceed the half value of the sampling rate f_s.

That is

$$f_{max} \leq \frac{1}{2} f_s$$

Thus, the sampling rate can be determined accordingly. For this study, it was programmably adjusted as

$$f_s = \frac{1}{T} = 2048$$

The corresponding analysed frequency range is from 0 to 1024 Hz.

Sampling Length --- Size of Sample

The fluctuation is regarded as a stationary stochastic process. To eliminate the window effect, the sampling length, i. e. sampling point N, was taken as the maximum value of the buffer length covering at least 50 cycles of the lowest (basic) harmonic.

Thus, the sampling points for each sample was

$$N = 2^{11} = 2048$$

Statistical Results

For each test condition, the performances of the sampling (N=2048 points) and the corresponding data processing (such as the statistical- and spectrum analyses etc.) were all repeated 10 times. Then, the average values of them were output as the statistical results for the given test condition to assure the statistical accuracy for this stationary stochastic event.

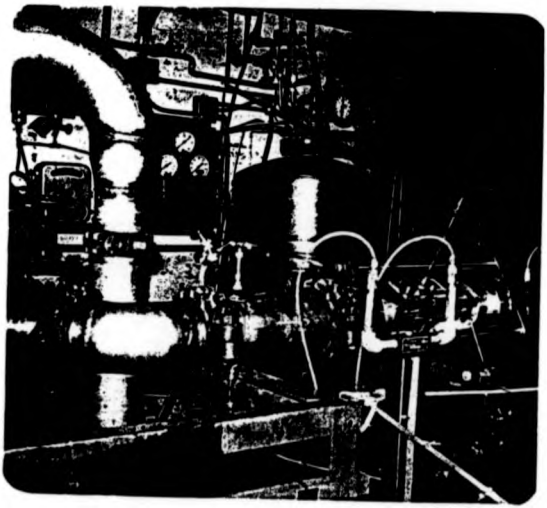

Figure 2-1. Venturi Cavitating Loop, University of Michigan (U-M)

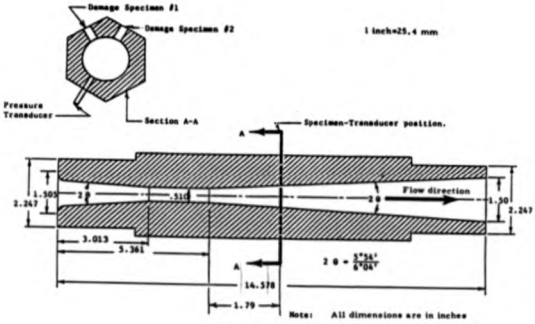

Figure 2-2. U-M Venturi Test Section and Transducer Position

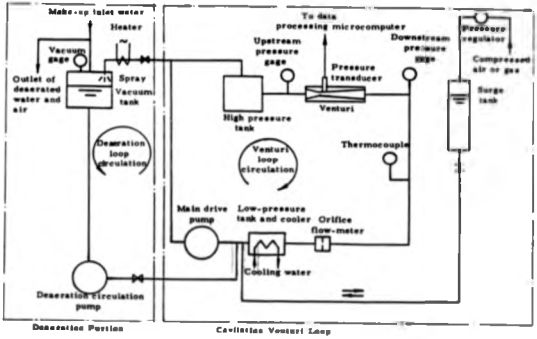

Figure 2-3 (a). Schematic Cavitating Venturi Facility

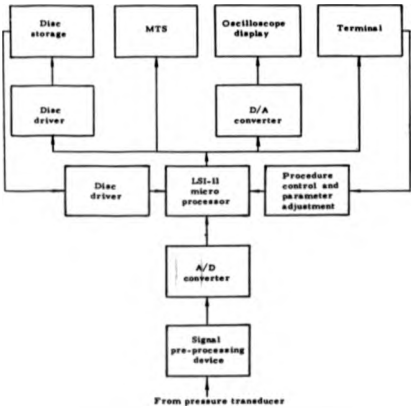

Figure 2-3 (b). Venturi Tunnel Facility (Data Processing Portion: Real Time Computer System)

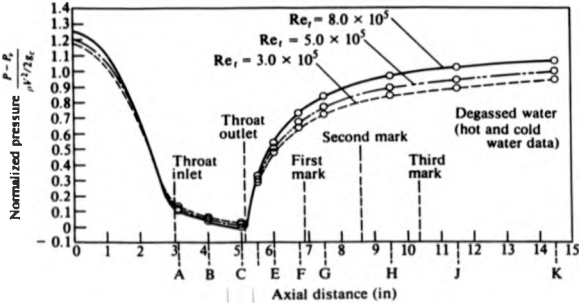

Figure 2-4. U-M Venturi Static-pressure Profile. Normalized Pressure vs. Axial Position (Sonic Initiation)

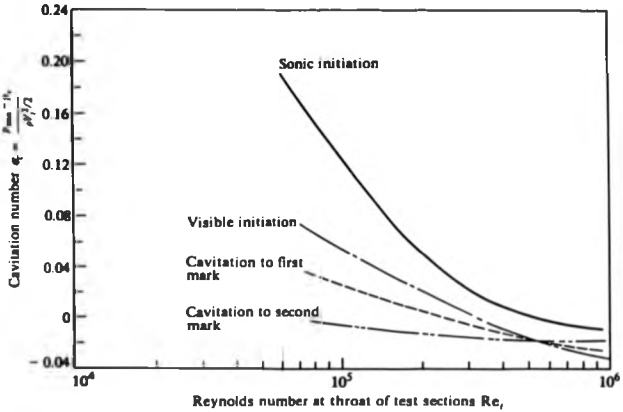

Figure 2-5. Comparison of Cavitation Number vs. Throat Reynolds Number for Various Degrees of Cavitations (U-M venturi)

[Hammitt]

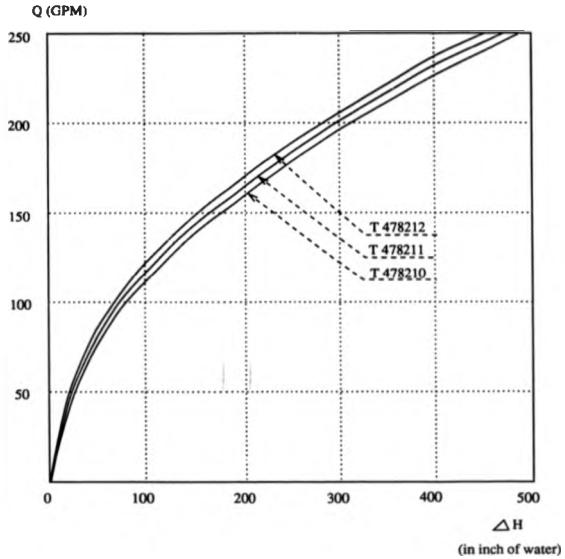

Figure 2-6 Calibration Curve of Orifice Device with Plate No. T478211

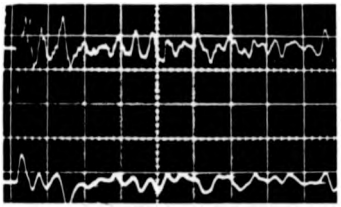

Figure 2-7. Responses of Kistler 601 A to Underwater Spark Bubble. (Top trace without charge amplifier; the bottom one with charge amplifier)

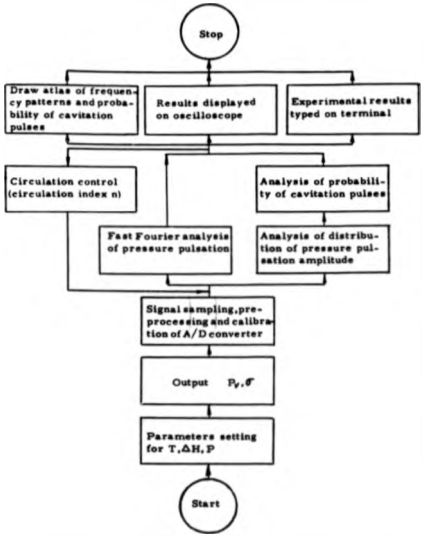

T: Water temperature, ΔH: Manometer pressure differential, P: Downstream pressure, P_v: Vapor pressure, σ: Cavitation number.

Figure 2-8. Flow Chart of Main Program

Kistler Model 601 A

Diaphragm diameter	0.2 in
Risetime	3.0 μs
Temperature range	-40 to 260 °C
Capacitance of quartz crystal	5 pF
Sensitivity	1 pcb/psi
Resonant frequency	130 kHz
Maximum pressure	5000 psi
Pressure range	10 to 300 psi
Curie point of quartz	550 °C
Mechanical Q	10
Piezoelectric constant	2.3 pcb/N
Dielectric constant (air)	4.5

Table 2-1. Characteristics of Kistler Model 601 A

3. OBSERVED PHENOMENON AND THEORETICAL ANALYSIS

3.1. Phenomenon Features

Through the characteristics study of cavitating venturi flows in the University of Michigan venturi, it was found that the overall pressure pulsation is composed of several components. According to their own distinctively statistical features and the variation laws with the cavitation development, they can be statistically categorized as three basic components [24] as already been mentioned before (refer to 1.3.1 Description of Phenomenon): basic flow noise, cavitation pulses and cavitation associated low-frequency fluctuations. For understanding the mechanism of the component of the cavitation associated low-frequency fluctuations, the experimental observations were carried out with the test range from V=28 to 38.4 m/s. Then, the analytical and numerical analyses were performed as well. The results for these different values of velocity V show similar features as described below. The test results for V=38.4 m/s are used as the typical situation throughout.

3.1.1. Features of Analogue Signals

Low Frequency

One of the main features of this observed component (i.e. the cavitation associated low-frequency fluctuations) is that the basic harmonic and its higher order harmonics are all appear at very low frequencies ranging from the order of 10^1 to 10^2, in contrast with the frequency of the flow noise component (up to 10 kHz) and with that of the cavitation bubble pulses (very short duration, μ second range). This feature can be clearly seen from Figure 3-1 which is the typical waveforms of these three components extracted from a test with T=26.7°C, V_{throat}=38.4 m/s and σ varying from 1.12 to 0.65, i. e., from non-cavitation to fully developed cavitation.

Periodicity

The perfect periodicity is another important feature of this component, which distinguishes this component from the somewhat irregular flow noise component; and from the rather random cavitation pulses. Of course, the cavitation pulses might also present some sort of periodic nature due to the mutual influences with the periodic perturbations of the dominant flow field, such as the Van Karman's vortex street flow etc. as has been discussed in Section 1.2.4. But the periodic nature of the cavitation pulse is totally different --- it is a statistical periodicity of the stochastic-event appearance and its strength depends on the value of $\frac{\sigma}{\sigma_i}$, whereas, the event of the analogue waveform itself of the low-frequency fluctuation does not present this sort of periodicity. This feature can also be seen from Figure 3-1.

Statistical Symmetry

The comparison of the statistical distributions of the three basic components of pressure pulsations clearly shows the another important feature of the component of the cavitation associated low-frequency fluctuations: its contribution to the symmetrical expansion of the statistical distribution curve.

Because these three components appear at their own corresponding flow stages, the overall pressure pulsation is the different combinations of these three components for different flow stages, and the resultant patterns of the statistical distribution curves for different flow stages (cavitation number σ's) thus varies with the variation of the combination of these three components accordingly.

The flow noise appears at all σ's, regardless of the presence of cavitation. The bubble-collapse pulses (short duration and sharp peak) appear whenever cavitation is present. Whereas, the cavitation associated low-frequency fluctuation component (50 to 60 Hz) appears primarily near cavitation inception σ_i but also for more developed cavitation (lower σ), and disappears for fully developed cavitation ($\sigma \leq 0.65$). The waveforms

of the overall pressure pulsations at different (typical) flow stages are shown in Figure 3-2.

The corresponding statistical distribution curves for these typical flow stages are shown in Figure 3-3. From Figure 3-3 (a), it can be seen that for the non-cavitation stage (σ=1.12) where only the flow noise component is present in the overall pulsations, the statistical distribution curve appears to be a standard normal distribution (mean value E_ξ=0 and square root variance D_ξ=1.04 for this particular case); and for the fully developed cavitation stage (σ=0.65) where both components of the flow noise and the cavitation (bubble-collapse) pulses are present, the corresponding statistical distribution curve (σ=0.65) is transformed from the curve for σ=1.12 (non-cavitation) by expanding its right side towards higher pressure region due to the contribution from the collapse pulses (this right-side expansion also indicates the positivity of the most cavitation pulses as expected). With the reduction of σ down to 0.93,0.84 and 0.74 respectively, the component of low-frequency appears in the overall pulsations and the statistical curves expand symmetrically as shown in Figure 3-3 (b) because of the addition of this basically (statistically) symmetrical low-frequency fluctuation component. For example, the value of D_ξ increases up to 5.95 for the case of σ=0.93 which is just about the cavitation inception. At this cavitation regime, the right-side expansion is still present and it increases with the strengthening of the cavitaion pulse intensity (reduction of σ) as shown by the curves for σ=0.84, 0.74 respectively in Figure 3-3 (b).

Therefore, it can be concluded that the main contribution of the low-frequency component is to symmetrically expand the statistical distribution curve of the overall pressure pulsations (the stronger the component, the more symmetrical expansion). In other words, this component presents the nature of statistical symmetry.

Association Nature

The extensive observations show that the component of low-frequency fluctuations associates closely with the cavitation presence (especially with the inception). It

appears just before the visible inception (σ_{inc}=0.89) and grows rapidly around inception point. With the reduction of σ it reaches a maximum then gradually disappears for further reduction of σ. This association with cavitation is also an important indicator of cavitation inception which has been suggested by the author as an alternatively indirect indicator of cavitation inception for this cavitating venturi flows and possibly for other similar cavitating flows [30]. And it has been thus named as *Cavitation Associated Low-frequency Fluctuation* [24,31].

All the tests on the University of Michigan venturi show similar features as those mentioned above. Some typical waveforms for different throat velocities are shown in Figure 3-4 (V_{throat}=28 m/s, σ=1.12, 0.93, 0.74, 0.69, 0.65) and Figure 3-5 (V_{throat}=35 m/s, σ=1.12, 0.84, 0.74, 0.65). From these waveforms, the association with cavitation and its variation with the cavitation development can also be seen clearly.

3.1.2. Features of Spectra

The results of the spectrum analyses of the overall pressure pulsations using the DFT show clearly the features of the low-frequency fluctuation component, which agree well with the foregoing analyses based on the analogue waveforms.

For each test (i.e., throat velocity V_{throat}), the DFT analyses were performed from non-cavitation to fully developed cavitation at the decrement of cavitation number $\Delta\sigma$=0.05 to observe the variation of spectrum features with the cavitation degree. For focusing on the spectra of the low-frequency component, the frequency range of DFT analyses were chosen as 0 to 1024 Hz, the corresponding sampling rate is 2048 points per second.

The typical DFT result (V_{throat}=38.4 m/s, σ=0.84, 0.74, 0.69) is shown in Figure 3-6. When σ reduces down to σ=0.84 just past the visible inception point (σ_{inc}=0.89), there is a strongest peak with relative amplitude $\frac{a_f}{a}$=8.2 appearing at a low frequency f_f=60 Hz in the spectrum for σ=0.84. Here a_f is the amplitude at this particular frequency f_f=60 Hz

and $\bar{a}$ is the average amplitude over the frequency range of this spectrum for given σ. This strongest peak, $\frac{a_f}{\bar{a}}$, approximately designates the strength of the low-frequency fluctuation component. The other higher order harmonics have much lower peaks and higher frequencies, e. g., there is a much smaller peak existing at the frequency of 240 Hz. The other two spectrum curves for the further reduced σ's (σ=0.74 and 0.69) show the similar features and have basically the same frequencies (f_f=50 Hz) at which the strongest peaks but with relatively lower amplitudes ($\frac{a_f}{\bar{a}}$=5.0 and 2.0 respectively) appear. For other values of σ (not shown in Figure 3-6), the frequencies f_f are also within the range of 50 to 60 Hz basically independent of σ. Whereas, the values of $\frac{a_f}{\bar{a}}$ depend strongly upon the cavitation number σ (that is, when σ≥1.12, $\frac{a_f}{\bar{a}}$≈0; when σ approaches the inception σ_{in}=0.89, $\frac{a_f}{\bar{a}}$ rapidly increases and reaches a maximum with further reduction of σ then gradually reduces to $\frac{a_f}{\bar{a}}$≈0 at σ=0.65). In order to show the detail of the low-frequency component, a semi-logarithmic presentation of the spectra is presented in Figure 3-7.

If the dimensionless amplitude

$$\frac{a_f}{0.5\rho V^2_{max}}$$

is plotted against the cavitation number σ as shown in Figure 3-8, the variation law of the strength of the low-frequency component with the cavitation degree (σ) especially the feature of the rapid growth around the inception can be highlighted.

Thus, the spectrum features can be summarized:

A The characteristic frequency F_f at which the strongest peak appears remains basically constant at a relatively low level, here 50 to 60 Hz.

B Its strength, i. e. the relative amplitude $\frac{a_f}{\bar{a}}$, shows a strong dependence upon the variation of cavitation number, presenting the association nature with cavitation

inception.

3.2. Theoretical Analysis

3.2.1. Wave Propagation in Bubbly Medium

The behaviour of pressure wave propagation in the cavitation cloud is one of the important factors dominating the phenomenon of the cavitation associated low-frequency fluctuation. Actually, the cavitation cloud is a bubbly medium of liquid-vapour/gas (in bubble form) mixture. It becomes a highly elastic medium with remarkably reduced wave propagation speed, as low as 15 m/s reported by Arndt [1], compared with the speed in pure liquid.

To show the substantial characteristics of the wave propagation in the bubbly medium, the case of the linear wave propagation in the liquid containing small amount of gas bubbles was studied by Van Wijngaarden [32], with following assumptions:

A All bubbles are spherical with the same radius, in disturbed condition.

B The gas concentration by volume is small, i. e., void fraction $\alpha \ll 1$, subsequently, the liquid in the mixture still forms continuous phase.

C The frequency of the wave is so low that the local pressure in the liquid can be considered equal to the local pressure in the gas.

D The thermodynamic change in the gas phase are of isentropic.

E No relative motion between bubbles and liquid.

F The wave has an infinitesimal amplitude and the linear analysis can be performed.

The main physical effect of the small gas bubbles dispersed in the water is that the compressibility of the resulting liquid becomes remarkably larger than that of the pure water, which dominates the propagation speed of the low-frequency sound waves.

If let ρ_g and ρ_l denote the densities of gas and liquid respectively, the mass of the gas in a per unit mass of the mixture should be constant, i. e.,

$$\frac{\alpha\rho_g}{\rho_l(1-\alpha)+\rho_g\alpha}=constant \qquad (3.2\text{-}1)$$

Here, the denominator of Eq. (3.2-1) is the unified density of the mixture ρ_{mix},

$$\rho_{mix}=\rho_l(1-\alpha)+\rho_g\alpha$$

Considering the assumptions of C and D above, (3.2-1) can be written as

$$\frac{\alpha p^{\frac{1}{k}}}{\rho_l(1-\alpha)+\alpha\rho_g}=constant \tag{3.2-2}$$

where:

k =the ratio between specific heats in the gas

For $\rho_g \ll \rho_l$ and neglecting the compressibility of liquid, following relation will be held approximately,

$$\alpha\approx\frac{\rho_l-\rho_{mix}}{\rho_l} \tag{3.2-3}$$

Thus, from (3.2-2) and (3.2-3), the sound wave propagation speed (S_g) in the liquid-gas mixture can be derived

$$\left[\frac{dp}{d\rho}\right]^{\frac{1}{2}}=S_g=\left[\frac{kp}{\rho_l\alpha(1-\alpha)}\right]^{\frac{1}{2}} \tag{3.2-4}$$

Extensive experiments have verified the accuracy of Eq.(3.2-4) in predicting the sound speed in the liquid with dispersed gas bubbles except for the extreme cases with $\alpha\to0$ or $\alpha\to1$, where some appropriate corrections are needed.

Based on Eq.(3.2-4), the family of curves of the sound speed in the liquid-gas mixture as the function of the free gas concentration α and pressure p are shown in Figure 3-9. From these analytical resolutions shown in Figure 3-9, the effect of the dispersed air bubbles on the wave propagation can be seen. The presence of the air bubbles will dramatically reduce the wave speed S_g, even lower than the speed in pure air. The larger the air concentration, the lower the wave speed except for the case of $\alpha\to1$. The wave speed also reduces quickly with the reduction of the pressure p. Curve No.1 corresponds to the pressure p equal to the vapour pressure p_v at temperature of 27°C (test temperature),

$p=p_v=3531P_a(27^oC)$

The study by Van Wijngaarden [33] of the effect of the natural frequency of the bubble oscillation on the wave propagation shows that the wave frequency f does affect the behaviour of the wave propagation especially if the wave frequency f is close to the natural frequency f_{bubble} of bubble oscillation.

According to (1.2-31), the natural frequency of air bubble is

$$f_{bubble}=\frac{1}{2\pi}\left[3k\frac{p_{i,eq}}{\rho R_0^2}-\frac{2\sigma}{\rho R_0^3}\right]^{\frac{1}{2}}$$

If the surface tension is neglected,

$$f_{bubble}=\frac{1}{2\pi R_0}\left[3k\frac{p_{i,eq}}{\rho}\right]^{\frac{1}{2}} \tag{3.2-5}$$

or

$$\omega_{bubble}=\frac{1}{R_0}\left[3k\frac{p_{i,eq}}{\rho}\right]^{\frac{1}{2}}$$

For the case of cavitation bubbles, filled with both vapour and air, the internal equilibrium pressure $p_{i,eq}$ in the Eq.(3.2-5) for the case of air bubble should be replaced by

$$p_{i,eq}=p_v+\frac{4}{3}\frac{\sigma}{R_0}$$

if the surface tension is to be taken account for.

When the frequency ω of waves in bubbly liquids approaches the bubble resonance frequency ω_{bubble}, the liquid inertia in radial acceleration and deceleration associated with the spherical oscillation of the bubbles becomes so important that the assumption C above is no longer valid, i. e. the local pressure in liquid can not be considered as equal to the local pressure in the gas. Thus, the wave propagation speed is also no longer determined by (3.2-4) and it becomes a frequency-dependent speed. Wijngaarden [33] introduces the generalized Rayleigh equation to represent the difference between the pressure p_∞ in the liquid far from bubble and the internal pressure p_i of the air bubble, i. e. Eq.(1.2-23),

$$p_\infty-p_i=\rho_l\left[R\frac{d^2R}{dt^2}+\frac{3}{2}\left(\frac{dR}{dt}\right)^2+\frac{4\nu}{R}\frac{dR}{dt}\right] \tag{3.2-6}$$

Taking (3.2-6) as the pressure difference and the viscosity as the damping mechanism for the radial motion, the velocity u in the mixture could be expressed in the following wave equation form,

$$\frac{\partial^2 u}{\partial t^2} = S_l^2 \frac{\partial^2 u}{\partial x^2} + \frac{S_l^2}{\omega_{bubble}} \frac{\partial^3 u}{\partial x^2 \partial t} + \frac{4 S_l^2 \lambda_v}{\omega_{bubble} R_0^2} \frac{\partial^3 u}{\partial x^2 \partial t} \tag{3.2-7}$$

Instituting the solution form of $\exp i(\alpha x - \omega t)$ into (3.2-7), the dispersion equation results,

$$\frac{\alpha^2}{\omega^2} = \frac{1}{S_l^2} + \frac{1 - \frac{\omega^2}{\omega_{bubble}^2} + \frac{i\delta\omega}{\omega_{bubble}}}{S_l^2 [1 - \frac{\omega^2}{\omega_{bubble}^2})^2 + \delta^2 \frac{\omega^2}{\omega_{bubble}^2}]} \tag{3.2-8}$$

Here, S_l is the sound speed in pure liquid, δ is the logrithmic decrement for damping. In (3.2-7), the viscous damping δ_{vis} is the only damping component included, which is

$$\delta_{vis} = \frac{4\nu}{\omega_{bubble} R_0^2}$$

As has been discussed in 1.2.2. Single Bubble Dynamics, in the range of R_0=10^{-1} to 4×10^{-4} cm, the thermal damping $\delta_{thermal}$ dominates the viscous- and acoustic component (δ_{vis} and $\delta_{acoustic}$ respectively) contributions to the energy dissipation. $\delta_{thermal}$ and $\delta_{acoustic}$ are also frequency-dependent parameters [33],

$$\delta_{thermal} = \frac{3(k-1)}{2(\frac{\omega}{2D_g})^{\frac{1}{2}} R_0}$$

where:

D_g =thermal diffusivity of gas

$$\delta_{acoustic} = \frac{\omega^2 R_0}{[1+(\frac{\omega R_0}{S_l})^3] \omega_{bubble} S_l}$$

The real part of $\frac{\omega}{\alpha}$ given by (3.2-8) represents the propagation speed of the acoustic wave with frequency ω, whereas the imaginary part represents the damping. The results reported by Oldenziel [34] for air bubble with radius R_0 in water are shown in Figure 3-10, 3-11, which agree quite well with the experimental observations [32].

Figure 3-10 shows that for $\omega \to 0$ the wave speeds tend to the values determined by (3.2-4), they rise above S_l for $\omega \to \omega_{bubble}$ and reduce to the value of S_l for $\omega \to \infty$. Figure 3-11

shows that the damping effect reaches the maximum for $\omega = \omega_{max}$. These give a good explanation on the dispersion behaviour of the acoustic waves in bubbly liquid due to the variation of the bubble dynamic response.

If the bubbles have different size, i. e. the assumption A is no longer valid, the dispersion expression corresponding to (3.2-8) becomes very complicated and the statistical distribution of the bubble size must be considered, i. e. the results from (3.2-8) must be weighed with the number density over the bubble size distribution.

For waves with finite amplitude, i. e. the assumption F is no longer valid, the presence of bubbles will further affect the wave propagation resulting in the amplitude dispersion and frequency dispersion, which is much more complicated.

From above analysis, it can be concluded that for the University of Michigan venturi cavitating flow, the wave propagation behaviour is complicated and should be treated differently from that for the pure liquid due to following factors.

A The presence of the cavitation cloud, i. e. the bubbly medium of liquid-vapour/gas mixture, causes the effects of the wave-speed reduction, the wave-propagation dispersion and the wave-attenuation variation.

B The presence of the finite amplitude will further disperse the wave propagation.

C The nonuniform radius of bubbles will complicate the bubble dynamic response to the pressure waves.

D The three dimensional effect of the cavitation cloud.

Therefore, the wave propagation in the cavitation cloud of the venturi is a strongly three-dimensional and nonlinear behaviour. However, considering the features of the low-frequency fluctuation component, some approximations can be made so that the wave propagation speed of this component can be evaluated.

According to the radius range of 0.254 to 1.27 mm [35], the natural frequency of the cavitation bubbles in the venturi cavitating flows can be estimated by (3.2-5) as

f_{bubble}=4.7–23.6 *kHz*

The frequency of the low-frequency fluctuation component, f_f=50–60 Hz, is much smaller than the natural frequency of bubbles f_{bubble},

$$f_f \ll f_{bubble}$$

Thus, according to above analysis, the wave propagation speed of this component can be approximately treated as frequency-independent parameter. Furthermore, the experiments show that in practice the sound in a liquid-vapour mixture propagates at the same sound speed as in a liquid-gas mixture [36]. Therefore, as an approximation, the wave speed S_s evaluated by (3.2-4) can be used as the wave speed S_{cav} (of the low-frequency fluctuation component) in the cavitation cloud (liquid-vapour/gas mixture). The value of S_{cav} for this study is thus evaluated as

$$S_s=\left[\frac{dp}{d\rho_{mix}}\right]^{\frac{1}{2}}=\left[\frac{kn}{\rho_l\alpha(1-\alpha)}\right]^{\frac{1}{2}}=20\text{–}25\ m/s$$

3.2.2. Natural Frequency of Cavitation Cloud

The natural frequency of the cavitation cloud depends on the cloud shape and dimension as well as on the wave speed S_{cav}. As a preliminary approximation, a linearized one-dimensional model is assumed by the author [31] as follows (referring to Figure 3-12).

A Cloud is the homogeneous two-phase medium of liquid-vapour/gas mixture and both phases have the same velocity. It has uniform temperature T, and uniform equilibrium values of density $\bar{\rho}_{mix}$, and pressure $\bar{P}$.

B For given σ, the positions of the phase-change interfaces are stationary. Letting x designate the longitudinal coordinate in the venturi, x_u be the coordinate value of the upstream interface and x_d be the value of downstream interface. Then x_u and x_d are constant, and the cavitation cloud length, $L_{cav}=x_d-x_u$, is also a constant value.

C One-dimensional flow is assumed with

$$v=\frac{Q}{A}$$

where:

V =velocity

Q =volume flow rate

A =cross-section area

D Conduit elasticity- and frictional effects are negligible.

E Assuming a small oscillation, the pressure P (also expressed in terms of hydraulic head H) and flow rate Q can be linearized about their equilibrium values, $\overline{H}$ and $\overline{Q}$, as follow:

$$\begin{cases} H=\overline{H}+h' \\ Q=\overline{Q}+q' \end{cases} \tag{3.2-9}$$

where:

$$H=\frac{P}{\rho}$$

Then

$$A(x)=A_m+\frac{\partial A}{\partial x}(x-x_m) \tag{3.2-10}$$

Thus, the continuity and momentum equations for the cavitation cloud can be written respectively,

$$\frac{\partial \rho_{cav}}{\partial t}+\frac{1}{A}\frac{\partial(\rho_{cav}VA)}{\partial x}=0 \tag{3.2-11}$$

$$\frac{\partial V}{\partial t}+V\frac{\partial V}{\partial x}+\frac{1}{\rho_{cav}}\frac{\partial P}{\partial x}=0 \tag{3.2-12}$$

Introducing equations (3.2-9) and (3.2-10) into Eqs.(3.2-11) and (3.2-12), neglecting higher order terms, considering

$$\frac{\partial h'}{\partial x}\ll\frac{\partial h'}{\partial t}\ ;\ \ \frac{\partial q'}{\partial x}\ll\frac{\partial q'}{\partial t}$$

and taking

$$\frac{\partial A}{\partial x}=\frac{\pi}{2}\tan\theta\approx 0\ \ (\text{for}\theta=3^0)\ ;\ \ \frac{\partial \overline{H}}{\partial x}\approx 0$$

Eqs.(3.2-11) and (3.2-12) become

$$A_m\frac{\partial h'}{\partial t}+\frac{S_{cav}}{g}\frac{\partial q'}{\partial x}=0 \tag{3.2-13}$$

$$g\frac{\partial h'}{\partial x}+\frac{1}{A_{cav}}\frac{\partial q'}{\partial t}=0 \tag{3.2-14}$$

Eliminating q' from (3.2-13) and (3.2-14) yields

$$\frac{\partial^2 h'}{\partial t^2}-S_{cav}^2\frac{\partial^2 h'}{\partial x^2}=0 \tag{3.2-15}$$

Under the boundary condition

$$h'|_{x=x_0}=h'|_{x=x_0}=0$$

and using the variable separation method to solve Eq.(3.2-15), the eigenvalue solution is obtained. And, the first harmonic frequency f_{cav} of the cavitation cloud is

$$f_{cav}=\frac{S_{cav}}{2L_{cav}} \tag{3.2-16}$$

3.2.3. Physical Model

The mechanism of the low-frequency fluctuation is complex. As a preliminary result, an empirical-theoretical model based on the foregoing analysis is proposed by the author [31] to explain the observed phenomenon as follows.

When flow is noncavitation, only the liquid phase is present in the entire closed loop. When cavitation occurs, an additional vapour-gaseous phase appears within the cavitation cloud which has two phase-change interfaces at its up- and down stream ends. The flow in the diffuser portion of the venturi becomes much more unstable due to the appearance of highly elastic cavitation cloud, resulting in some sort of self-stimulated pressure oscillation. The phase-change interfaces serve as the reflecting and reinforcing boundary conditions. The whole loop can be considered as a series complex pipeline system with both liquid and liquid-vapour/gas portions as shown in Figure 3-13.

The natural frequency of the pressure oscillation for the liquid portion depends mainly on the loop characteristics such as geometry, element elasticities and wave propagation speed in the liquid. It is basically independent of cavitation cloud length (i. e. the value of cavitation number σ). Its first harmonic frequency f_{liq} in the series pipeline can be analytically estimated [37] as:

$$f_{liq} = \sum_{n=1}^{m} \frac{S_{liq,n}}{4L_n} \qquad (3.2\text{-}17)$$

where:

$S_{liq,n}$ =wave propagation speed in liquid for nth pipe

L_n =nth pipe length

m -number of pipes in series

For the University of Michigan venturi loop, f_{liq} is estimated as

f_{liq}=53 (Hz)

Thus, once cavitation occurs, the venturi loop becomes a system in which low-frequency oscillations are much easier to be stimulated due to the appearance of the cloud. At the inception stage, the f_{cav} is much higher than f_{liq}(=53 Hz) due to the small value of L_{cav}. The stimulated low-frequency component oscillates approximately at the frequency of f_{liq}. With the reduction of σ, the lengthening of cloud length, L_{cav}, reduces the natural frequency, f_{cav}, of the cloud. When σ is reduced to 0.76–0.82, the cloud length increases to L_{cav}=0.16–0.24 m (measured from the exit of throat). And, f_{cav} decreases to 50–60 Hz according to Eq.(3.2-16), resulting in the coincidence of both frequencies of f_{cav} and f_{liq}. Thus, a maximum low-frequency fluctuation results for σ=0.76–0.82. That is, if

$$f_{cav} = f_{liq}$$

i. e.,

$$\frac{S_{cav}}{2L_{cav}} = \sum_{n=1}^{m} \frac{S_{liq,n}}{4L_n}$$

a resonant interaction between the cavitation cloud and the liquid portion results. This is called *Cavitation Resonance*, and the corresponding value of σ (here σ=0.76–0.82) is designated as σ_{res}.

The foregoing analysis and the estimated values of f_{liq}, f_{cav} and σ_{res} agree quite well with the experimental results, referring to Figures 3-6, 3-7 and 3-8. The low-frequency component appears for a slightly higher σ than the visual inception (σ_{inc}=0.89). This is presumably because, although there is no visible cavitation, the small local unstable

cavitation patches already occur before the general inception [7, 27], creating the low-frequency fluctuation component.

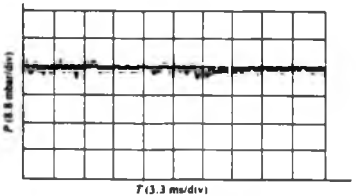

(a) Flow Noise Waveforms Extracted from Test with V=38.4 m/s, σ=1.12

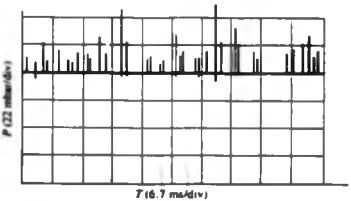

(b) Cavitation Pulse Waveforms Extracted from Test with V=38.4 m/s, σ=0.65

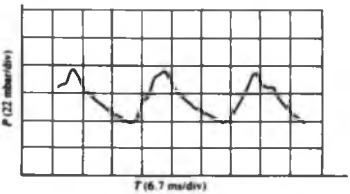

(c) Low-frequency Fluctuation Waveforms Extracted from Test with V=38.4 m/s, σ=0.74

Figure 3-1. Typical Waveforms of Three Components

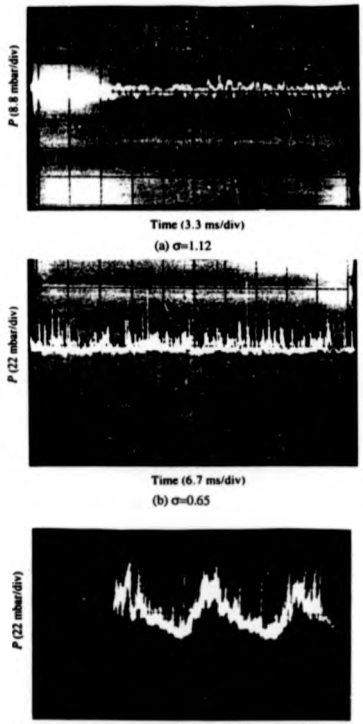

Figure 3-2. Waveforms of Overall Pressure Pulsations at Different Flow Stages, V=38.4 m/s

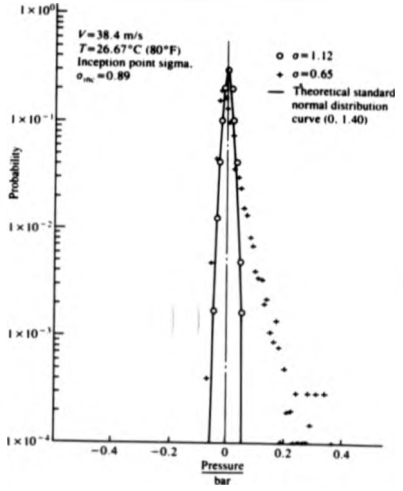

Figure 3-3 (a). Statistical Distributions of Pressure Pulsations, σ=1.12, 0.65

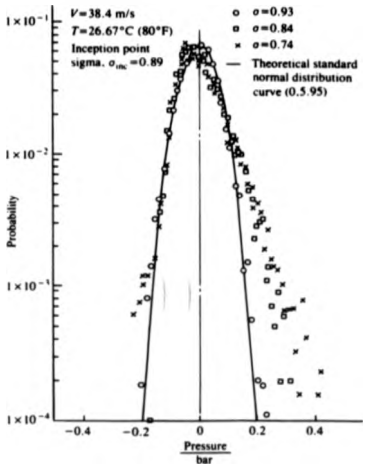

Figure 3-3 (b). Statistical Distributions of Pressure Pulsations, σ=0.93, 0.84, 0.74

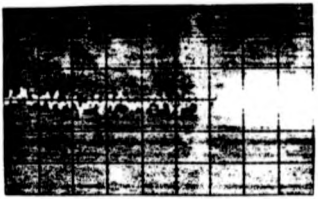

(a) σ=1.12

(b) σ=0.93

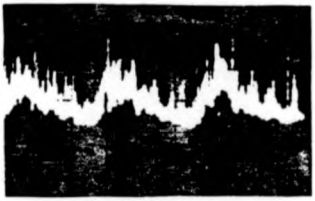

(c) σ=0.74

Figure 3-4. Waveforms of Overall Pressure Pulsations. V_{throat}=28 m/s, σ=1.12, 0.93, 0.74, 0.69, 0.65

(d) σ=0.69

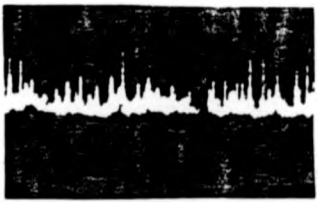

(e) σ=0.65

Figure 3-4(cont'd).
Waveforms of Overall Pressure Pulsations. V_{throat}=28 m/s, σ=1.12, 0.93, 0.74, 0.69, 0.65

(a) σ=1.12

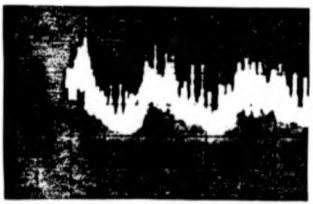

(b) σ=0.84

Figure 3-5. Waveforms of Overall Pressure Pulsations. V_{throat}=35 m/s, σ=1.12, 0.84, 0.74, 0.65

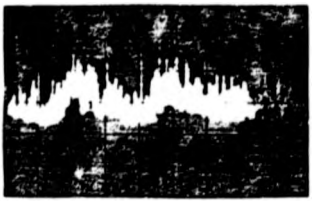

(c) σ=0.74

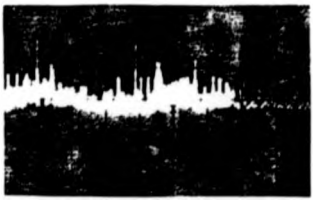

(d) σ=0.65

Figure 3-5(cont'd).
Waveforms of Overall Pressure Pulsations. V_{throat}=35 m/s, σ=1.12, 0.84, 0.74, 0.65

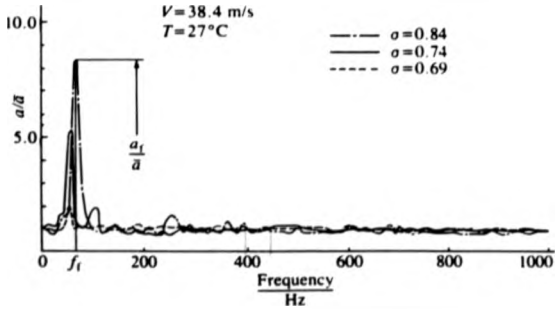

Figure 3-6. Frequency Spectra (Linear Plot), V_{stream} =38.4 m/s

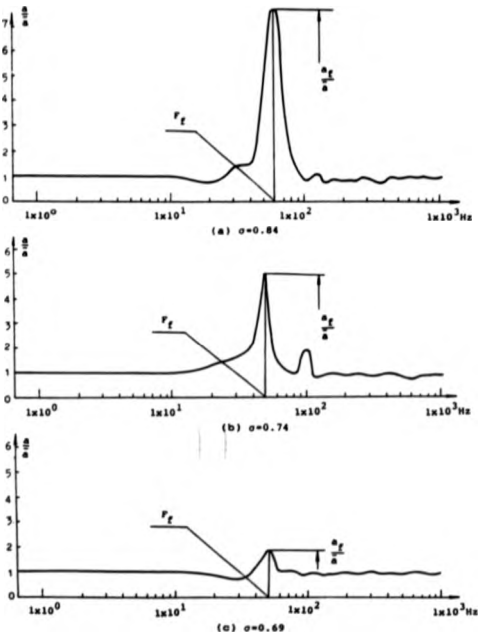

Figure 3-7. Frequency Spectra (Semilog Plot), V_{steam}=38.4 m/s

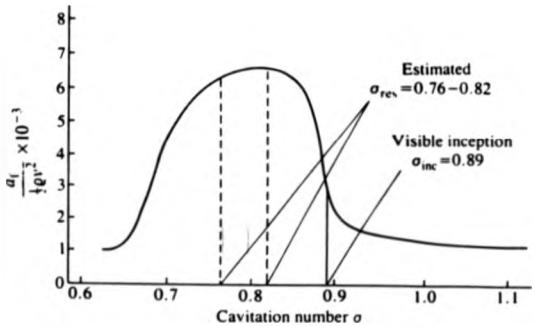

Figure 3-8. Non-dimensional Amplitude $\frac{a_f}{0.5\rho V^2 L_{max}}$ versus σ

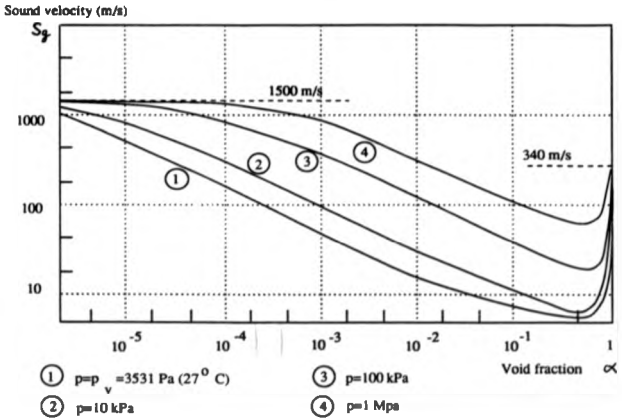

Figure 3-9. Sound Speed S_g in Water-gas Mixture as Function of α and p

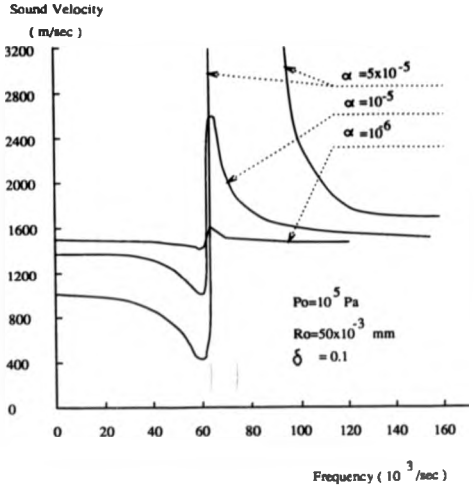

Figure 3-10. Sound Speed in Bubbly Mixture

[Wijngaarden]

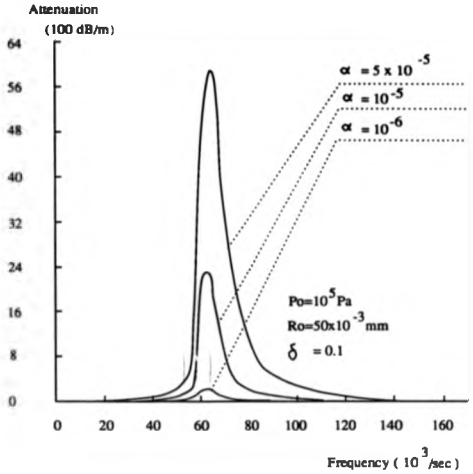

Figure 3-11. Attenuation of Sound in Bubbly Mixture

[Wijngaarden]

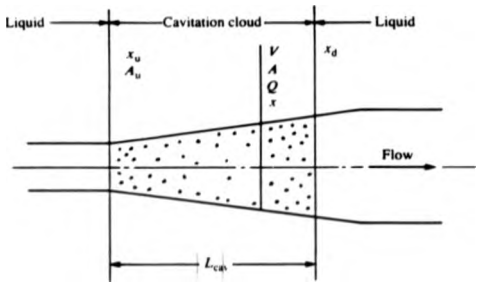

Figure 3-12. Linearized One-dimensional Cavitation Cloud

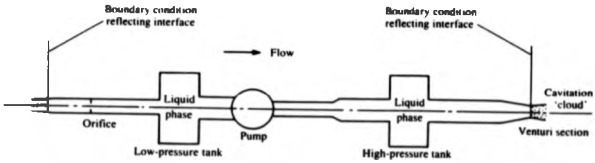

Figure 3-13. Schematic of Venturi Loop at Cavitating Flows

4. NUMERICAL STUDY

A numerical study, based on the proposed physical model, of the oscillation characteristics (i. e. the frequency response) of the University of Michigan venturi flow system is performed by the author using the *Hydraulic Impedance Approach*.

4.1. Theorem of Free Vibration Analysis Using Hydraulic Impedance Approach

The fluid oscillation in a complex flow system can be approximately analyzed by using the linear vibration theory to obtain some substantially analytical relations in respect of the system frequency response and the resonance. Basically, there are two different ways to analyze system response [37]. One is the *Frequency Response Analysis* using the concept of the steady forced vibrations. The second identifies the natural frequencies and the oscillatory mode shapes by the *Free Vibration Concept*, which is assuming a free vibration (in terms of both flow rate and pressure) at one of the natural frequencies initially existing in the flow system and then decaying exponentially due to the physical damping such as the friction etc. The latter one has been chosen for this study due to its following advantage. The free vibration method offers an alternative procedure without knowing the input forcing function, as required by the frequency response method, for the self-excited oscillation phenomenon in which the forcing factor is not clearly identifiable. Therefore, it is specially useful in studying the experimental data to identify and/or verify the cause of an oscillation/resonance which is just the case.

The concept of free vibration in frictionless hydraulic systems were firstly used by Jaegar [38]. In this study, the energy dissipation mechanism is also incorporated in the analysis. And, some special treatments are adopted to improve the numerical accuracy and to consider the inertia effect in the low- and high-pressure tanks.

Usually, there are two mathematical procedures [37] being used in the oscillatory flow study. One is the matrix method utilizing the transfer functions for the pressure and flow rate. The other is the hydraulic impedance approach which utilizing the transfer

functions for the hydraulic impedance as well as for the pressure and flow rate. Here, the hydraulic impedance approach is adopted for the free vibration analysis of the University of Michigan venturi flow system.

4.1.1. Linearized Unsteady Flow Equations for Use in Free Vibration Analysis

The general partial differential equations for the transient flow can be written in following form with the assumptions [37]:

A One-dimensional flow.

B Shear stress τ_0 being the same as if the velocity were steady, in Darcy-Weisbach factor f,

$$\tau_0=\frac{\rho f V|V|}{8}$$

C Medium being pure liquid with bulk modulus of elasticity K.

Motion equation

$$gH_x+VV_x+V_t+\frac{fV|V|}{2D}=0 \tag{4.1-1}$$

and the continuity equation

$$VH_x+H_t-V\sin\alpha+\frac{S^2}{g}V_x=0 \tag{4.1-2}$$

where:

x and t =longitudinal coordinate and time respectively

$H(x,t)$ and $V(x,t)$=centre line piezometric head (or elevation of hydraulic grade line above an arbitrary datum) and average velocity respectively; dependent variables with x and t

D =diameter of conduit

S =wave propagation speed in the liquid considering the properties of the conduit wall; $S=\left|\frac{\frac{K_l}{\rho}}{1+(\frac{K_l}{E})(\frac{D}{e})}\right|^{\frac{1}{2}}$

K_l =modulus of elasticity of liquid

E =modulus of elasticity of conduit material

D =diameter of conduit

e =thickness of conduit wall

For convenience, above equations are further developed by using discharge Q instead of velocity V, generalizing the friction term and neglecting small terms (such as $\frac{VQ_x}{gA}$). They become

$$\begin{cases} H_x+\frac{1}{gA}Q_t+\frac{fQ^n}{2gDA^n}=0 \\ Q_x+\frac{gA}{S^2}H_t=0 \end{cases} \tag{4.1-3}$$

where:

A =cross-section area of conduit.

For linearization treatment, the small perturbations of pressure and velocity are assumed,

$$H=\bar{H}+h'$$

$$Q=\bar{Q}+q'$$

and the friction term is expanded as series (which is convergent if $q'<\bar{Q}$) and only the first approximation terms are used, i. e.,

$$\frac{fQ^n}{2gDA^n}=\frac{f(\bar{Q}+q')^n}{2gDA^n}=\frac{f\bar{Q}^n}{2gDA^n}+\frac{nf\bar{Q}^{n-1}}{2gDA^n}\cdot q'$$

Thus, the linearized equations for free vibration flow result,

$$\begin{cases} h_x'+Lq_t'+Rq'=0 \\ q_x'+Ch_t'=0 \end{cases} \tag{4.1-4}$$

where:

L =inertance of the liquid in the pipe

$$L=\frac{1}{gA}$$

C =capacitance of the liquid in the pipe

$$C=\frac{gA}{\lambda^2}$$

R =linearized resistance per unit length of pipe

for laminar flow:

$$R=\frac{32\nu}{gAD^2}$$

for turbulent flow:

$$R=\frac{nfQ^{n-1}}{2gDA^n}$$

4.1.2. Transfer Equations

The transfer functions for hydraulic impedance as well as for head and discharge, used for the hydraulic impedance approach of the free vibration analysis, can be derived as follow [37].

Using variable separation method, the linearized equations (4.1-4) for free vibration can be changed as identical in form,

$$\begin{cases} q'_{xx}=CL\ q'_{tt}+RC\ q', \\ h'_{xx}=CL\ h'_{tt}+RC\ h', \end{cases} \tag{4.1-5}$$

Let

$$h'(x,t)=X(x)T(t),$$

the second equation of (4.1-5) becomes

$$\frac{1}{X}\frac{d^2X}{dx^2}=\frac{1}{T}\left[CL\frac{d^2T}{dt^2}+RC\frac{dT}{dt}\right]=\gamma^2$$

and the solutions of $X(x)$ and $T(t)$ have the form of

$$X(x)=A_1e^{\gamma x}+A_2e^{-\gamma x}$$

$$T(t)=A_3e^{\lambda t}$$

where:

λ =complex-valued constant, independent of x and t, called complex frequency

or Laplace variable containing real part σ and imaginary part ω respectively

$$s=\sigma+i\omega$$

γ=complex-valued constant, independent of x, t, and being the function of s, called propagation constant

$$\gamma^2=Cs(Ls+R)$$

Thus, the solution of the oscillatory pressure h', and subsequently the solution of q' can be obtained,

$$\begin{cases} h'=e^{st}(C_1e^{\gamma x}+C_2e^{-\gamma x}) \\ q'=-\dfrac{Cs}{\gamma}e^{st}(C_1e^{\gamma x}-C_2e^{-\gamma x}) \end{cases} \tag{4.1-6}$$

h' and q' may also be written as

$$h'(x,t)=H(x)e^{st}$$
$$q'(x,t)=Q(x)e^{st}$$

where:

$$H(x)=C_1e^{\gamma x}+C_2e^{-\gamma x}$$

$$Q(x)=-\frac{1}{Z_c}(C_1e^{\gamma x}-C_2e^{-\gamma x})$$

Z_c=characteristic impedance of the liquid in the pipe which is a complex-valued function independent of space and time but dependent upon the properties of the liquid and the pipe as well as upon the complex frequency s

$$Z_c=\frac{\gamma}{Cs}$$

Using the up- and down-stream end conditions, the integration constants can be evaluated in terms of H_U and Q_U at x=0, and the complex head $H(x)$ and discharge $Q(x)$ can be expressed as the function of position x

$$\begin{cases} H(x)=H_U\cosh\gamma x-Z_cQ_U\sinh\gamma x \\ Q(x)=-\dfrac{H_U}{Z_c}\sinh\gamma x+Q_U\cosh\gamma x \end{cases} \tag{4.1-7}$$

where:

H_U, Q_U =values of H, Q at up stream end, i. e., at $x=0$

Letting $x=l$, here l is the length of pipe, and solving (4.1-7) for H_U and Q_U, the transfer functions for the upstream head H_U and discharge Q_U in terms of the downstream conditions of H_D, Q_D can be obtained,

$$\begin{cases} H_U = H_D \cosh\gamma l + Q_D Z_c \sinh\gamma l \\ Q_U = \dfrac{H_D}{Z_c}\sinh\gamma l + Q_D \cosh\gamma l \end{cases} \tag{4.1-8}$$

If the ratio of the complex head $H(x)$ to the complex discharge $Q(x)$ is defined as the hydraulic impedance $Z(x)$

$$Z(x)=\frac{H(x)}{Q(x)}$$

then the transfer function for hydraulic impedance can be obtained by introducing the definition of hydraulic impedance into (4.1-8),

$$\begin{cases} Z_D = \dfrac{Z_U - Z_c \tanh\gamma l}{1-(\dfrac{Z_U}{Z_c})\tanh\gamma l} \\ Z_U = \dfrac{Z_D + Z_c \tanh\gamma l}{1+(\dfrac{Z_D}{Z_c})\tanh\gamma l} \end{cases} \tag{4.1-9}$$

Thus, if the complex-valued functions of head, flow rate and impedance at x are expressed in following form,

$$H(x)=|H(x)|e^{i\Phi_h}$$
$$Q(x)=|Q(x)|e^{i\Phi_q}$$
$$Z(x)=|Z(x)|e^{i\Phi_z}$$

thus, the following relation holds

$$|H(x)|=|Q(x)||Z(x)|$$
$$\Phi_h=\Phi_q+\Phi_z$$

4.1.3. Numerical Procedure

Theorem

It is assumed that a free oscillatory fluid motion already exists in the flow system. The analysis is used to reveal the system characteristics of the natural frequencies, the mode shape, and the hydraulic impedance profile. The substantial information of the flow oscillation in the system can be thus obtained.

Due to the complexity of the physical flow system, it is impossible to analytically solve the transfer function (4.1-8) to find the natural frequencies ($s=\sigma+i\omega$) satisfying the boundary conditions although the analytical solution for some simple frictionless configurations can be obtained. Alternatively, the numerical method is often adopted.

The hydraulic impedance Z, and/or head- and flow perturbations H, U at some boundary conditions of the system (such as high- and low pressure tanks, orifice, centrifugul pump etc.) are often known. Thus, the hydraulic impedance at some particular position, here the exit of low-pressure tank in the venturi loop, is chosen as the characteristic point for the impedance calculation, where the pressure is maintained as constant by the pressure regulator (i. e., the head oscillation $H12=0$) and the corresponding hydraulic impedance designated as Z12 in the computer program (Appendix A) is equal to zero,

$$Z12=H12=0$$

Thus, using the impedance transfer function (4.1-9), the impedance Z12 at the exit of the low pressure tank can be expressed in terms of other known impedances. Due to the propagation constant γ and the characteristic impedance Z_c in (4.1-9) being the function of frequency s, the resultant expression of Z12 to be solved numerically will be an implied equation of s,

$$Z12(s)=0 \qquad (4.1\text{-}10)$$

The solution satisfying (4.1-10) will be the complex-valued frequencies $s=\sigma+i\omega$ sought for the free vibration of the venturi system.

Newton's Iteration

Newton's iteration method is used for seeking the numerical solution of the implied Eq.(4.1-10) which is a multi-element problem.

The initial values of s used for Newton's iteration are found by performing a frequency scan with an assumed value of σ, in this study $\sigma=0$, which produces a number of minimum values of $|Z12|$ (here, 3 minima) in the resultant graph of the modulus $|Z12|$ *vs.* ω. The each of these 3 minima is investigated by the Newton's method to obtain the exact numerical solution of $s=\sigma+j\omega$ satisfying Eq.(4.1-10).

If s_i is one of the initial values of s, i.e. corresponding to one of the minima resulted from the frequency scan, the correction Δs to the s_i is

$$\Delta s = -\frac{Z12(s_i)}{\frac{dZ12(s_i)}{ds}}$$

The corrected value of s_i used for successive iteration is

$$s_i = s_i + \Delta s$$

Considering

$$\frac{dZ12(s_i)}{ds} \approx \frac{Z12(s_i+\varepsilon)-Z12(s_i)}{\varepsilon}$$

here, ε is a small change of s, in the program (Appendix A) it is expressed as

$$ZEP = CMPLX(DS, DOM)$$
$$DS = 0.01$$
$$DOM = 0.01$$

Thus, the correction Δs can be numerically calculated

$$\Delta s = -\frac{\varepsilon Z12(s_i)}{Z12(s_i+\varepsilon)-Z12(s_i)}$$

In this study, for accelerating the iteration procedure, the real part σ_i of the initial value s_i is assumed as $\sigma_i=-0.1$ instead of $\sigma=0$.

The iteration is carried out until

$$|Z12| \to 0$$

i. e.,

$|Z12| \leq TOL$

here, TOL (>0) is a small value chosen as

$TOL = 0.03$

Each of the initial values leads to one of the complex-valued frequencies of the system. Its imaginary part, ω, is a free vibration frequency and the real part, σ, is a measure of the decay rate of a free vibration in the system.

Mode Shape

Once the frequencies of free vibrations have been evaluated, the mode shape of vibration at each frequency can be determined by use of the transfer functions with a specification of the amplitude of the oscillatory head at some particular position. Here, the oscillatory head at the cross-section of transducer in the venturi section is specified as 1 m, i. e.,

$HDJJ = 1$

in the program (Appendix A).

The mode shape merely reveals the manner in which the free vibration appears in the system. But, due to the dependence of the magnitude of the mode shape upon the selected value of the free variable, i. e. the specified amplitude of the oscillatory head, the comparison of the magnitudes between mode shapes for different frequencies is not meaningful.

Hydraulic Impedance Profile

The variation of hydraulic impedance along the system for each frequency can be evaluated. This hydraulic impedance profile reveals the characteristics of each element of the system in respect of inducing the vibration at the particular frequency. The element or location showing a large value of hydraulic impedance is the position where small flow oscillation of the particular frequency may be capable of stimulating large head oscillation. Thus, the impedance profile of a complex flow system is helpful in identifying the

locations/elements at where the pressure perturbation of particular frequency is likely to be stimulated.

4.2. Schematization of Flow System

For a numerical study, the whole venturi loop has to be schematized. It is divided as a series of 11 pipes/elements. The schematization of the University of Michigan venturi system is shown in Figure 4-1.

4.2.1. Venturi Section

For the numerical accuracy, the venturi section is treated as a series of 5 sections with each section schematised as an equivalent cylindrical tube. The schematization is shown in Figure 4-2.

4.2.2. High- and Low Pressure Tanks

Considering the effect of the partial tubular flow within the tanks, the tanks are not merely treated as accumulators. The momentum effect is taken account of by adding an equivalent pipe to the accumulator as shown in Figure 4-3. That is, the tank is approximately considered as the combination of two portions, one is the tubular flow portion which is represented by an equivalent pipe, the other is an equivalent liquid accumulator.

The hydraulic impedance for the accumulator is

$$Z=\frac{iK_e}{\rho g\bar{V}\omega}$$

where:

$\bar{V}$=mean volume of liquid in the container

K_e=equivalent bulk modulus of elasticity of the liquid in the container

4.2.3. Orifice

The orifice used for measuring the flow rate is a fixed orifice. Its hydraulic impedance is

$$Z=\frac{2\bar{H}_0}{\bar{Q}}$$

where:

$\bar{Q}$=mean flow rate

$\bar{H}_o$=head drop across the orifice for mean flow rate; $\bar{H}_o$=1.27 according to the performance curve of this orifice

The hydraulic impedance of orifice is designated as BM in the computer program. The impedance transfer equation for the orifice is

$$ZU(11)=ZD(10)-BM$$

where:

$ZU(11)$=the value of hydraulic impedance at the upstream end of pipe 11

$ZD(10)$=the value of hydraulic impedance at the downstream end of pipe 10.

4.2.4. Centrifugal Pump

The impedance transfer equation for the centrifugal pump operating at constant speed is

$$ZU(2)=ZD(1)-PM$$

Here, PM is the slope of the pump characteristic curve at the operating point as shown in Figure 4-4. The value of PM dominates the role of the pump (whether it amplifies or attenuates the perturbations passing through the pump). According to the performance curve, PM=0.087.

4.3. Numerical Results and Discussion

4.3.1. Results

The computer program used for frequency scan, Newton's iteration, mode shape and impedance profile is included in Appendix A, which was run on the *Great Wall* 0520 CH computer (Chinese computer, IBM compatible).

Natural Frequency

Under the assumed σ=0, the hydraulic impedance at the exit of low pressure tank, i. e. Z12 against the complex-valued frequency $s=\sigma+i\omega$ was scanned by running the scan program with the step length

$$\delta s=\delta\sigma+i\,\delta\omega=0+i\,10$$

producing the graph of the modulus |Z12| vs. ω as shown in Figure 4-5. This result reveals 3 minimum values at

$$\omega_0=380,\ 920,\ 2160$$

which were used as the initial values for Newton's iterations to find the exact values of s satisfying

$$Z12(s)=0$$

The Newton's iterations were performed for each of these 3 minima with the real part σ, changed as -0.1,

$$s_0=-0.1+i\,380,\ -0.1+i\,920,\ -0.1+i\,2160$$

The iteration results are the natural frequencies of the system,

$$s_1=-1.03+i\,385.16$$
$$s_2=-6.82+i\,917.94$$
$$s_3=-1.54+i\,2156.50$$

Mode Shape

The mode shapes and the corresponding impedance profiles for these three frequencies are shown in Figure 4-6.

4.3.2. Discussion

The hydraulic impedance characteristics of the venturi flow system shows that there is a remarkably high impedance value at the venturi diffuser section, where cavitation cloud initiates and then develops, for the complex-valued natural frequency of s_1=-1.03+*i*385.16 (refer to Figure 4-6). As has been discussed in Chapter 3, the cavitation cloud itself is a highly elastic medium and is very easy to stimulate a low frequency oscillation. This result indicates that the cavitation cloud in this high impedance region has become more capable of inducing the self-excited pressure fluctuation at the basic frequency of ω_0=385.16 rad/sec (i. e. f_{bq}=61.3 Hz). This numerical solution is very close to the observed frequency F_f of the low-frequency fluctuation component,

F_f=50-60 (*Hz*)

With the reduction of σ, i. e. the lengthening of cloud length, the cavitation cloud frequency f_{cav} approaches the system basic frequency f_{bq}, the maximum fluctuation (resonance) results.

Therefore, the proposed mechanism of cavitation associated fluctuation and cavitation resonance is thus strongly supported by the numerical results.

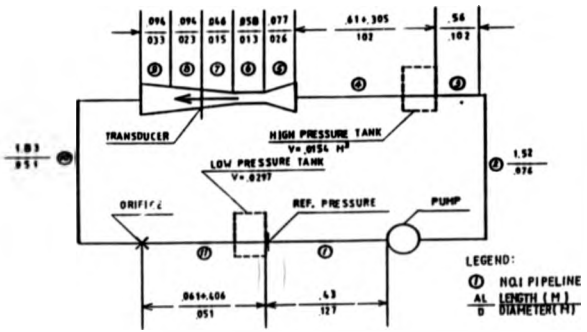

Figure 4-1. Schematization of U-M Venturi System

Legend: Equivalent Length / Equivalent Diameter

Unit: Meter

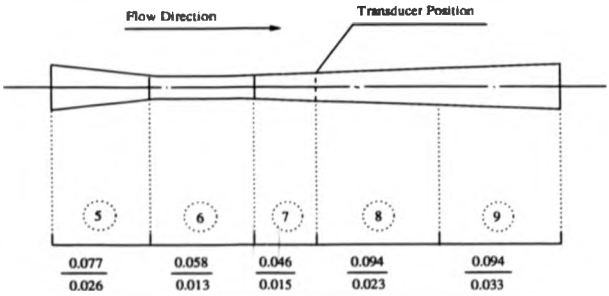

Figure 4-2. Schematization of U-M Venturi Section

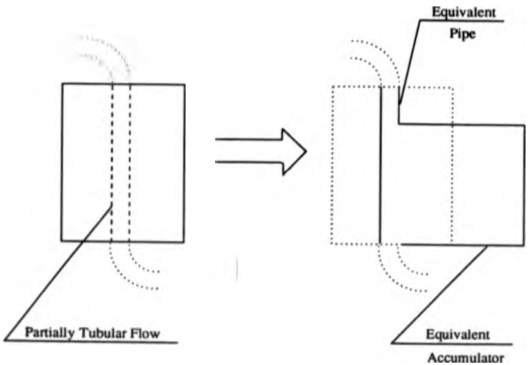

Figure 4-3. Schematization of High- and Low pressure Tanks

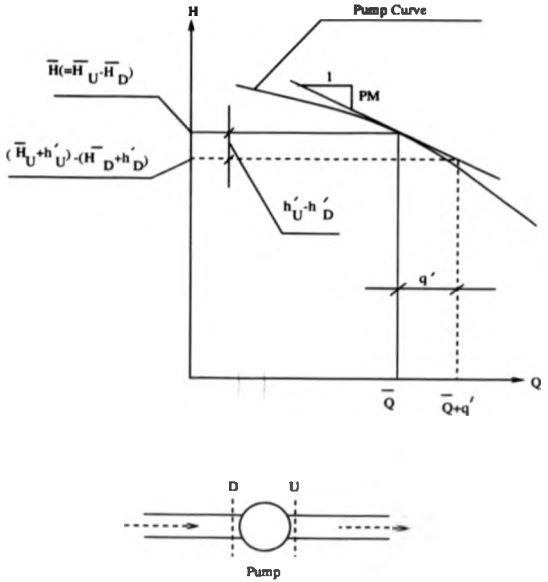

Figure 4-4. Hydraulic Impedance of Centrifugal Pump

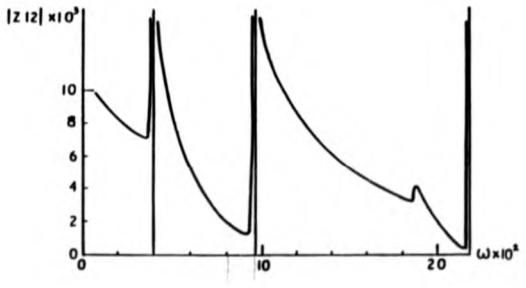

Figure 4-5. Modulus of Z 12 vs. Angular Frequency

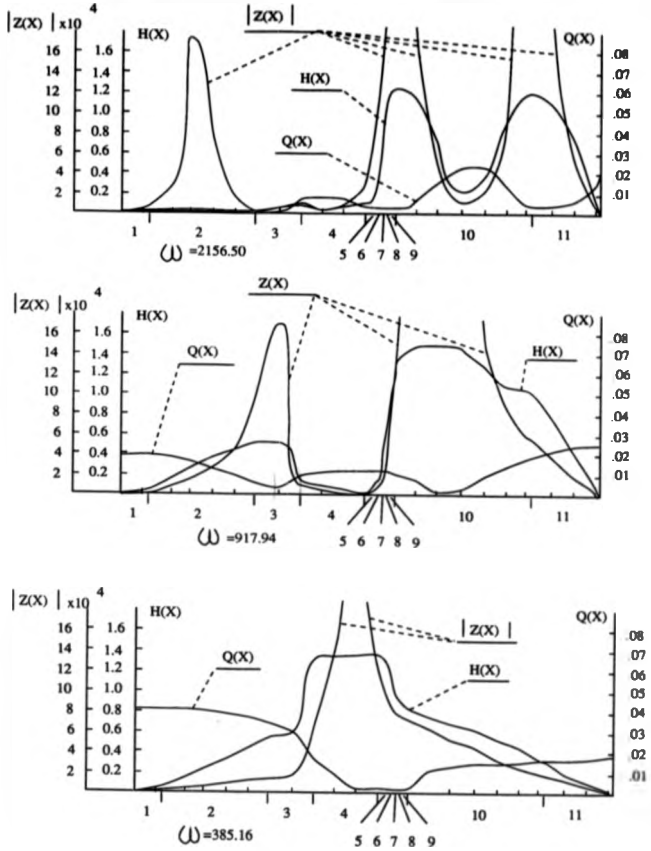

Figure 4-6. Mode Shapes and Impedance Profiles for ω=385.16, 917.94, 2156.50

5. PRACTICAL APPLICATIONS --- CAVITATION ASSOCIATED FLUCTUATIONS IN HYDRAULIC MACHINERY SYSTEMS

As has been explained before, the phenomenon of cavitation associated low-frequency pressure fluctuation is often observed in various flow systems, especially in the hydraulic machinery system. But, due to the complexity of the practical hydraulic engineering system in terms of the geometry (three dimensional effect) and the movement of the machine rotator, the mechanism through which the low-frequency fluctuation is induced is still not well understood.

The foregoing understanding of this phenomenon from the study of the University of Michigan cavitating venturi flow has been applied to the investigations of the cavitating flows in some hydraulic machinery systems in respect of the cavitation association nature of the low-frequency fluctuations. Some preliminary results are presented here.

5.1. Cavitating Flow in Draft Tube of Francis Turbine

5.1.1. Importance and Complexity

The huge pressure fluctuations in the Francis turbine's draft tube at partial load operation, which even spread through the whole system under certain conditions, is a challenging problem to the design and operation of the machine and system.

If the draft-tube flow is under cavitating condition, the fluctuations usually become much more severe and the mechanism of the phenomenon becomes much more complicated due to the formation of two-phase (liquid-vapour/gas) flow. Although, the vortex rope in the draft tube has been proposed as the general cause of this phenomenon, the mechanism (even qualitatively) of it is still not clear due to the following factors.

A. The nature of the (liquid-vapour/gas) two phase flow.

B. The non-steady three dimensional flow field with strongly nonlinear nature.

It is very difficult to establish an analytical mathematical model for this cavitating

draft-tube flow. So far, the contributions toward the solution of this problem are all made based on the Rheingans hypothesis [39]: the vortex rope formed in the draft tube at partial load operation is the unique cause of the fluctuations, even for the case of cavitating flows (such as the cavitating vortex-rope flow), and the whirling/rotation motion of the vortex rope plays the role in driving the fluctuation. Thus, this hypothesis must lead to the conclusion that the fluctuations must have the same frequency as that of the driving force , i.e. the rotating angular frequency ω_v, of vortex rope (or its higher-order harmonics). The very recent contribution from M. Fanelli [40] can be regarded as the most representative one. Its main points can be summarized as follow.

A. A basic steady potential flow field is dominated by a vortex rope with diameter kR, inclined angle θ and circulation Γ (referring to Figure 5-1). The parameters of Γ, k, θ can be determined through solving simultaneous equations of (5.1-1), (5.1-2) and (5.1-3), which represent the discharge continuity, the conservation of the ratio of the momentum moment F_{mx} to moment F_m, and the value of the circulation Γ at runner exit respectively,

$$Q\,(=nQ_0)=\frac{\Gamma R(1-k^2)}{2kl g\,\theta} \tag{5.1-1}$$

$$\beta_0 tg\,\theta=\frac{F_k^2 E(n)}{nk}\cdot\frac{C_v}{C_Q} \tag{5.1-2}$$

$$\frac{\Gamma}{\omega_0 R^2}=2\pi(1-\frac{n}{C_v})C_r \tag{5.1-3}$$

where:

Q =discharge rate

Q_0=zero-swirl discharge rate

$n\le 1$

R =radius of the straight part of the draft tube

$\beta_0=\frac{Q_0}{\pi\omega_0 R^3}$

ω_0=rated turbine angular speed

$F_2=\frac{gH}{\omega_0 R}$

H=head applying upon the turbine

$E(n)=(1-n)\{E_1(1-n)-E_2+A\cdot\eta_H(1+n)\}$

E_1=1.1 ~ 1.2

E_2=0.05 ~ 0.1

A=0.1 ~ 0.2

η_H=hydraulic efficiency of turbine at n=1

$C_v(\leq 1)$=volumetric coefficient, $C_{v_{n=1}}=1$

C_Q=velocity distribution coefficient, $C_Q=1+k^2$

$C_r(<1)$=correction coefficient for circulation evaluation

The potential ϕ_1 formed by this vortex rope only induces a " Rotational Pressure Field ". The spatial average pressure at each section will remain steady.

B. A similar postulation is proposed for the elbow part, and the existence of the elbow is the only cause to induce the so-called " Synchronous Pressure Excitation " at frequency ω_n, due to the destruction of the axial-symmetricity of the vortex rope flow field in the elbow especially if the elbow does not contain exactly an even number of half-pitches (half-wavelengths) of the toroidal helix, referring to Figure 5-2. Thus, the excitation amplitude in elbow and diffuser will be

$$\frac{\Gamma^2}{gR^2}\cdot E_b,\ \frac{\Gamma^2}{gR^2}\cdot E_d$$

respectively. Accordingly, a small (potential) perturbation $\Delta\phi$ should be superposed,

$$\Delta\phi=\frac{\Delta n Q_0}{\pi R^2}z\cdot e^{i\omega_n t}$$

The corresponding discharge variation will be

$$\Delta Q=\Delta n\cdot Q_0 e^{i\omega_n t}$$

C. If the vortex rope is cavitating, a lumped cavity model in compliance with the driving movement is actually supposed, whose function is no more than enhancing the existing " Synchronous Pressure Excitation ". The volumetric variation of the cavitated vortex rope per unit height of Δx is

$$q_v = \frac{\Delta Q}{\Delta x} = A e^{i\omega_v t}$$

where:

$$A = \frac{i\omega_v \pi D_v}{2\sin\theta} d_v$$

D_v =diameter of cavitating rope determined under liquid-phase flow condition, i.e. the non-cavitating case. (Note: this is obviously not reasonable)

d_v =small perturbation of D_v induced by the driving force explained in B.

To accommodate the volume variation, a even-distributed source-sink model is used, and the pseudo-Poisson equation is established to solve the following additional potential field caused by the volumetric variation of the cavitating vortex rope,

$$\phi_{vv} = A\left(\frac{r^2}{2\pi R^2} + \phi_0\right) e^{i\omega_v t}$$

D. The whole system will response to this excitation at the frequency of ω_v, or/and at its higher order harmonics if non-linear effect is concerned.

E. In short, the mechanism proposed is that the excitation exists only if the co-existing condition of a rotating vortex rope and a elbow (especially if it contains non-even number of half-pitches of the toroidal helix) is met, whereas the cavitation of the vortex rope as a lumped cavity only enhances the excitation already existing before the appearance of the cavitating vortex rope.

Considering the complexity of the problem itself, it should be said that above model proposed by Fanelli is quite well self-contained and gives a conceptual explanation of the

mechanism of the excitation which is driven through the interaction of the rotating vortex rope with the elbow.

The experimental investigations, based on the similar hypothesis as proposed by Fenelli, of Rheingans pressure surge of the model Francis turbines have been also carried out by some investigators [55,56,57] and the following mechanism has been postulated to explain the phenomenon:

The rotating pressure field (formed by the swirling/rotation of the cavitating vortex rope) is the unique driving force inducing the observed pressure oscillation in the subsystem, i.e. the draft tube system. If the frequency of the driving force (i.e. the rotating pressure field) coincides with the natural frequency of the subsystem, the amplitude of the pressure surge reaches a maximum. The natural frequency of the subsystem is evaluated based on a lumped model of the subsystem, i.e. lumped cavity at the up-stream end, lumped water column in the draft tube and the tail water with constant free surface at the down-stream end. The lumped capacitance C ($=-\frac{1}{H}\frac{\partial V_{cav}}{\partial \sigma}$) or the cavitation compliance C' ($=CH$) of the cavity is evaluated by its V_{cav} - σ relation. Therefore the mechanism proposed merely explained the pressure fluctuation component caused by the interaction of both the rotating driving force and the subsystem response taking into account the effect of the volumetrical variation of the cavity.

The above two mechanisms reported in [40] and [57] respectively are based on the same hypothesis that the origin of the driving force is the swirling/rotation of the cavitating vortex rope and the cavity only functions passively as a lumped chamber. The only difference is: the former describes the Rheingans pressure surge as the result of the interaction of the swirling/rotation of vortex rope with the elbow whereas the latter describes it as the interaction of the rotating pressure field with the lumped subsystem.

5.1.2. Author's Remark

However, as has been explored by the author in the Statistic Cavitation Study carried on the Cavitation Venturi Flow, the function of cavitation cloud in a dynamic cavitating flow system should not simply be simulated just as a passive vapour-chamber, i.e. the lumped cavity model. The cavitation cloud has its own dynamic characteristics rather than the function of a lumped compliant vapour chamber. For example, the cloud's natural frequency is one of the major characteristics which varies with the wave propagation speed, the shape and size of the cloud, and the movement of cloud such as the rotation/swirling of cavitating vortex rope in Francis Turbine's draft tube [25]. Under certain condition, the cloud would serve as an exciter inducing some sort of oscillations in the system (i.e. the component defined as the cavitation associated low-frequency fluctuation in previous Venturi study), which are different from and have much higher frequencies than the Rheingans pressure oscillation component (it will be discussed in 5.2.), due to its own dynamic nature of the high elasticity rather than the passively compliant function.

This idea was used by the author to investigate the draft-tube cavitating flow of a Francis turbine model in 1988 [41], trying to find the characteristics of the cavitation associated low-frequency fluctuation and the interaction relationship between the macro attribution (here, the periodical pressure pulsation) and the micro attribution of cavitation (i. e. the characteristics of cavitation bubble collapse behaviour). One of the findings is that the cavitating vortex rope not only acts as a compliant vapour chamber to the driving force of the rotating vortex rope, but also induces a low-frequency fluctuation at its own characterized frequency, which is much higher than ω_{rr} . This phenomenon found in cavitating draft-tube flow of Francis turbine presumably has similar mechanism as the cavitation associated low-frequency fluctuation in the cavitating venturi flow. As an example of the application of this theorem to the investigation of the practical hydraulic machinery system (here the model turbine system), some of the preliminary

result is thus briefly explained in next section.

5.2. Experimental Study

5.2.1. Experimental Design

The investigation was carried on the Chinese model runner of Francis type turbine HL-160-25 in Author's Hydraulic Machinery Lab, NCIWCP.

Cavitation Test Stand

The model runner is installed on the closed Cavitation Test Stand (Figures 5-3 and 5-4), which was specially designed for the cavitation test of model turbine (D_1=250mm). It consists mainly of the turbine test section, vacuum tank, low-pressure tank, driving pump (speed variable), air absorber tank, venturi flow-rate meter, high pressure tank. The HL-160-25 model runner was chosen to be studied, which is one of the turbines inducing strong vortex rope at partial load operation. The specifications of HL-160-25 are listed as follow, referring to Figure 5-5.

Type: Radial-Axial Flow HL-160-25 (i.e. Francis turbine)

Size: Nominal Diameter D_1=250 mm

Specific Speed: n_s=180 (optimum operation condition)

Efficiency: η=90.5 %

No. of Blades: 17

Relative Height of Guide Vane: $\overline{b_0}=\frac{b_0}{D_1}$=0.224

No. of Guide Vanes: 24

The draft tube for the model is chosen, based on the theorem of the optimum performance, from the Chinese Standard, which consists of straight cone, elbow and diffuser sections with following specifications, referring to Figure 5-6.

Height: 651 mm

Length: 1124 mm (=436+688)

Exit Height: 328 mm

Height of Straight Cone: 200 mm

Height of Elbow: 340 mm

Diffusive Angle: β=9°

Data Acquisition and Processing System

The Data Acquisition and Processing System basically consists of various transducers for pressure and flow rate measurements, signal pre-processing facilities and 0520 CH (Great-Wall) real-time computer system. Figure 5-7 is the photograph of the partial signal processing facilities (excluding the charge amplifiers etc) and computer system. The schematic data acquisition and processing system is shown in Figure 5-8.

Piezoelectrical Transducer

For measuring the short-duration cavitation collapse pulses as well as the low-frequency pressure fluctuations in the cavitating draft-tube flows, a set of 4 piezoelectrical transducers (Model PT-80) of high accuracy and response frequency were mounted flush with the draft-tube wall shown in Figure 5-9, which were specially designed and made by the Mechanics Institute of China Academic for this test. For investigating the transmission of the pressure fluctuations in the system, a fifth piezo-transducer was mounted at the inlet of the spiral case (Figure 5-9). The main specifications of PT-80 are:

Pressure Range: -1 to 4 atm

Sensitivity : 1000 - 2000 pcb/atm

Accuracy: +- 0.5 %

Response Frequency: 40 k Hz (first natural frequency 100 k Hz)

Diameter: 4 mm

The quasi-dynamic calibration of these 5 transducers were carried out successively at 1, 2, 3 atm pressure levels after their static calibrations. The results are listed in Table 5-1. Figure 5-10 is the photo of these transducers.

Software

The software specially designed by the author for this test can perform:

A The monitoring of the turbine operation parameters such as the unit speed n_1', unit discharge Q_1', and installation cavitation number σ_y.

B The various samplings (in terms of sampling rate, size and combinations of sampling channels) of the pressure oscillations at the draft tube and at the inlet of the spiral case.

C The sampling of cavitation bubble collapse pulses.

D The statistical and spectral analyses.

Experimental Procedure

Test Procedure

To investigate the variation of the vortex rope with the operating point (n_1', Q_1') and the installation cavitation number σ_y, the testing points of HL-160-25 were arranged covering nearly the whole range of the Hill Chart while the test head H retained constant H=6 m (referring to Figure 5-11). Here, the definitions of n_1', Q_1', and σ_y are:

$$n_1'=\frac{nD_1}{H^{\frac{1}{2}}}$$

$$Q_1'=\frac{Q}{D_1^2H^{\frac{1}{2}}}$$

$$\sigma_y=\frac{H_a-H_s-H_v}{H}$$

where:

H_a=atmosphere value at the site (in terms of hydraulic head), here, being the vacuum pressure of the vacuum tank

H_s=suction head, referring to Figure 5-9

H_v=vapour pressure at the test temperature (in terms of hydraulic head)

For each testing point (i. e. each pair of n_1', Q_1'), the investigation was performed with the draft-tube flow varying from non-cavitation to fully developed cavitation (by reducing the value of σ, through the pressure reduction of the vacuum tank). The test procedure is as follows:

A Fixing the guide vane opening at one of the four test openings, a_0=5.6, 7.85, 10, 12.54 mm.

B Changing the runner speed n to achieve the required value of unit speed by means of varying the brake torque applying on the turbine shaft; meanwhile the speed of the driving pump has to be adjusted accordingly to maintain the constant test head, H=6 m.

C Changing σ_v to the required value by means of adjusting the vacuum value in the vacuum tank; meanwhile some minor regulations of the pump speed are needed to maintain the constant head.

D Maintaining the turbine running at the required test conditions (n_1', Q_1', σ_v) whereas the computer based data acquisition system automatically monitors the operation making sure that the current values of n_1', Q_1' and σ_v meet the required values and are stable enough for the data sampling; and the sampling procedure is thus triggered automatically.

Data Sampling

For the signal sampling of the low-frequency pressure fluctuations, the sampling parameters are chosen as follow.

No of channels to be sampled:

5 channels with the piezoelectrical transducers marked 11, 56, 38, 1, 23 in sampling order

Overall sampling rate:

6250 points per second

Overall sampling length:

60000 bytes = 30000 words (points)

Sampling length of each channel:

30000/5 = 6000 points

Sampling rate for each channel:

6250/5 = 1250 points per second

Sampling time:

30000/6250 = 4.8 seconds

Thus, according to Nyquist sampling theorem, the frequency range of the pressure fluctuations sampled is 0.21 to 625 Hz which just covers the whole frequency range of the low-frequency fluctuations in the craft tube and at the inlet of the spiral case. For sampling the signals emitted from the bubble collapse pulses, a data sampling of very high frequency was performed as well, the results which is beyond this topic will not be included here.

Considering the nature of stationary random process, the sampling was repeated 5 times, and the sampled data were stored in the floppy disk for further processing.

The main flow chart of the sampling procedure is shown in Figure 5-12. The corresponding computer program is listed in Appendix B.

5.2.2. Observation

The observations of the flow patterns in the draft tube and the spectral analyses of the fluctuation waveforms were performed for each test (operating) point with the flow varying from fully-developed cavitation to non-cavitation.

The flow patterns observed can be basically categorized as following 5 types:

A One-phase (liquid) flow.

This is the case that the flow is an entire non-cavitation flow which appears for all operating points with relatively high values of σ_v. There might be invisible vortex (in various forms such as vortex rope etc.) existing in the draft tube flow for some operating points deviating from the non-rotation (runner-exit) flow condition.

B (Cavitating) central (straight) vortex (thin) filament.

This usually appears at the very early stage of the cavitating flow. For some critical cavitation conditions, it presents the nature of instability - sometimes appears and sometimes disappears. The typical photo and schematic pattern of it are shown in Figure 5-13.

C (Cavitating) spiral vortex rope.

This usually forms at further reduced values of σ_v, i. e. more severe cavitation conditions and with the runner-exit flow deviating from non-circulation condition. Sometimes, a periodical swing situation (between the central vortex filament and spiral vortex rope) presents. The typical photo and its schematic pattern are shown in Figure 5-14.

D (Cavitating) inversely conic cavity.

With the further development of cavitation, the spiral vortex rope would usually develop into a much thicker one especially for its top portion, resulting a nearly inversely conic cavity with relatively small swirling. Sometimes, it even becomes a fixed inversely conic cavity without swirling due to the severe cavitation and/or the non-circulation runner-exit flow. The typical pattern is shown in Figure 5-15.

E Dispersive vapour-liquid flow.

With further development of the cavitation and/or at some certain operating points where runner-exit flow has small circulation, an uniform liquid-vapour/gas two-

phase flow would occupy the whole top of the draft tube for some short period which usually appears when the inversely conic cavity becomes unstable and is just in the course of transit. The typical pattern is shown in Figure 5-16.

The frequencies of the pressure fluctuations recorded are basically within following 3 bands. Sometimes, there would be 2 even 3 fluctuation components of these bands co-existing in the pressure field of the draft tube subject to the operating conditions (n_1', Q_1', σ_v), which will be discussed in detail later on.

A Frequency F_1.

It covers the frequency range of 1.22 to 6.1 Hz, concentrating in the range of 2.44 to 4.0 Hz. This frequency component usually appears at severe cavitating flows and presents the dependence upon the runner speed. The typical waveforms and the spectra (from transducers 11, 56 and 1) for the operating condition of a_0=5.6 mm, n_1'=66.34 rpm and σ_v=1.18 are shown in Figure 5-17, here, F_1=2.44 Hz.

B Frequency F_2, ranging from 52 to 88 Hz.

This component always appears for all test (operating) points provided that the cavitation occurs in the draft tube and reaches some certain early stage (quite often a cavitating vortex rope with the spring-like axial vibration can be observed). This component also shows the dependence upon the runner speed. The typical waveforms and their spectrum analyses for a_0=5.6 mm, n_1'=45.93 rpm, σ_v=1.32 are shown in Figure 5-18.

C Frequency F_3, ranging from 140 to 315 Hz, even higher.

This component appears mostly at non-cavitation conditions and/or early stage of cavitation, and it often disappears with further (severe) cavitation development. It presents strong dependence on the runner speed. The typical waveforms and spectra for a_0=12.54 mm, n_1'=51.03 rpm, σ_v=1.59 are shown in Figure 5-19.

5.2.3. Analysis and Discussion

In order to further explore the causes of these fluctuation components (especially the cavitation association nature of some components), it is necessary firstly to evaluate the frequencies of the potential driving forces and their relations with the operating conditions, and to analyze the frequency-response characteristics of the whole system.

Potentially Driving Forces

The possible driving forces for the fluctuations in this system were analyzed and their frequencies were evaluated as well.

A. Rotation/swirling of the vortex rope --- Rheingans Explanation.

This driving force usually appears at part load operation and its frequency varies with runner speed. The frequency range evaluated for HL-160-25 is $0.00432\,n$ corresponding to 2.16 to 3.46 Hz for n=500 to 800 rpm. This coincides quite well with the frequency of F_1 component and should be taken as a significant factor contributing to the F_1 component.

B. Effect of finite numbers of runner blades and guide vanes.

The frequencies from these two factors (for n=500 to 800) are evaluated as 141.7 to 226 Hz and 200 to 300 Hz respectively. These are well within the frequency range of F_3 component.

C. Karman vortex street in the blade tail wake.

The frequency of perturbation caused by this effect has the order of 1×10^3 Hz which is much higher than that of F_3 and falls beyond the highest sampled frequency of 625 Hz. Obviously, it has nothing to do with the observed pressure fluctuations.

D. Perturbation caused by the pressure-wave reflection between the up- and down stream ends of the draft tube.

The frequency of this perturbation is evaluated as ≈311.4 Hz, which contributes to the F_3 component.

So far, those mentioned above are all known potential factors which could contribute to the pressure fluctuations. According to the currently proposed interpretations [39, 40], the appearance of cavitation (usually in cavitating vortex rope form) is only passively to enhance the existing fluctuations and will not induce any other fluctuation components. Thus, it seems that no rational causes within the available hypotheses could be used to explain the genesis of the observed F_2 component here if the F_2 component is not interpreted as the effect of *Cavitation Associated (Induced) Low-frequency Fluctuation* in the cavitating draft-tube flows (this will be further discussed after the next subject of Frequency Response of Flow System).

Frequency Response of Flow System

The hydraulic impedance approach is used again for the analysis of the frequency-response characteristics of the system due to the same reasons described for the numerical study of the venturi system.

System Schematization

The system is schematized as shown in Figure 5-20. The vacuum tank is divided into two portions: the weir-enclosed part is considered as the constant-pressure portion; the rest part filled with certain amount of air is considered as an air chamber partially filled with water.

For the accuracy sake, the draft tube is divided into three short cylindrical pipes with the diameters equal to their own average diameters. For the same reason, the venturi section is divided into three portions: the throat portion is pipe No.8; the up- and down stream diffusers are included in the adjacent pipes 7 and 9 respectively.

The transfer impedance of the HL-160-25 turbine is linearized as

$$ZU12=ZD11-TM$$

where:

ZU 12=hydraulic impedance at the up-stream end of pipe 12

ZD 11=hydraulic impedance at the down-stream end of pipe 11

TM =the slope of the turbine H-Q performance curve at the operating point, here TM=20 for Q=150 l/s.

The driving pump is also linearized as

ZU 4=*ZD* 3+*PM*

where:

PM =the slope of the pump H-Q curve at the operating point.

Characteristics Analysis of System Vibrations

The characteristics of the system vibration were numerically studied using the computer program in Appendix C. The program firstly performs the frequency scan using the tail water of draft tube as the reference point where

HD 14=*ZD* 14=0 (5.1-4)

to get the first approximation of the complex-valued frequencies $s=\sigma+i\omega$ satisfying equation (5.1-4). These natural frequencies are expressed in terms of the variation of |*ZD* 14| vs. angular frequency ω shown in Figure 5-21. The accurate values of these frequencies were obtained by performing the Newton's iteration using their first approximations as the initial values. The resultant accurate frequencies are:

-0.8 + i 26.92

-0.09 + i 53.71

-0.83 + i 78.68

-0.36 + i 393.75

-1.89 + i 740.38

-0.12 + i 1015.58

The mode shapes for s_1=-0.8+*i* 26.92 and s_2=-0.36+*i* 393.75 are shown in Figure 5-22.

The impedance at the draft tube (pipes 12 to 14) for s_2 is much higher than that for s_1, which indicates that the pressure fluctuations in the draft tube are much more likely to be stimulated by a very small discharge perturbations at or near the frequency of s_2.

Discussions

It has been found in previous venturi study that the cavitation cloud portion will induce some sort of cavitation associated low-frequency pressure fluctuations at its own natural frequencies f_{cm}, and the value of f_{cm} depends basically on the wave propagation speed as well as its own geometry (i. e. its length in the linearized one-dimensional venturi model). In the draft tube case, the phenomenon becomes much more complex due to following factors: the dramatical variations of the geometry of the cavitation cloud (e. g. from central cavitation vortex filament to cavitating spiral vortex rope, etc) and their strongly three-dimensional effect; the complex movements of cavitation cloud itself such as rotation, swirling etc; and the dependence of the natural frequency of the cavitation cloud upon the cloud movement as well as upon its wave speed and geometry [25]. Although a three-dimensional mathematical model reflecting these substantial relations has not been achieved yet, some general features can be summarized by comparing the observed phenomenon from the cavitating draft-tube flows with the cavitation associated fluctuations in venturi system:

A. The component of F_1 is always associated with cavitation conditions and never appears at non-cavitation flows.

This is just the distinctive feature of F_1 component --- it can never be observed under non-cavitation flows, i. e. it has the nature of cavitation association.

B. The value of the natural frequency of the cloud depends on wave speed, cloud geometry and its movement.

The observed F_1 frequency does show a speed-dependent feature which is presumably due to the influences from the cavitation cloud movements such as the

rotation/swirling of the cavitated vortex rope etc. The dependence of F_3 frequency on the unit speed n_1' is shown in Figure 5-23.

In some cases, the spring-like axial vibration movement of the cavitated vortex rope can be obviously observed for which a typical spectral result is shown in Figure 5-24. It can be seen that in addition to the F_3 component, a strong F_2 (=51.27 Hz) component, together with its second and third harmonics, appears in the spectrum.

The F_3 component also shows the dependence on the cloud shape. In the tests, it is observed that when the cavitating vortex rope gradually grows thicker and longer with the reduction of σ_v, the F_3 component usually reduces its frequency. The amplitude of F_3 usually becomes quite large when the cloud develops up to a certain shape and size (i. e. its corresponding natural frequency approaches to, or coincides with, one of the natural frequencies such as s_2=-0.36+*i*393.75). With further reduction of σ_v, the cloud usually transforms into an inversely conic cavity; subsequently, the F_3 component disappears and only a strong F_1 component presents (as shown in Figure 5-17). At this cavitation stage, the cloud behaves rather like the lumped cavity model which acts passively as a vapour chamber volumetrically oscillating at the driving frequency (2.16 to 3.46 Hz) according to Rheingans theorem, and the F_3 component usually becomes weak (even entirely disappears) presumably because the high frequency component of F_3 is much easier to be absorbed by the large cavity.

C. Cavitation associated fluctuation component often becomes significant when the frequency f_{nat} is close to or coincides with one of the system frequencies.

The observed F_2 component does show this feature as has already been described in B. The fluctuation also propagates in the whole system. The amplitudes of F_2 component for different guide-vane openings at some typical positions of the system, i. e. the inlet of spiral case (transducer No.1), up- and lower parts of the conic portion of draft tube (No.11 and No.56 respectively), are shown in Figure 5-25.

From the foregoing analysis of the system frequency response, it is known that the hydraulic impedance at the conic part of the draft tube for s_2=-0.36+*i*393.75 (which is just within the frequency range of F_2 component) is quite large. This explains why the F_2 component is so easier to be stimulated in the draft tube with strong amplitude travelling upwards into the penstock. It just meets the features of cavitation resonance as described for venturi cavtating flows.

D. In addition to above features, the mutual influence between the flow field and cavitation cloud has also been observed.

The cavitation cloud portion, as known, is the result of the vaporization of the partial liquid in the flow field due to the reduction of σ_v. Whereas, the appearance of cavitation cloud not only means the medium change (from liquid phase to liquid-vapour/gas two phases), it also inversely produces the significant changes of the flow pattern, i. e. the change of flow field (velocity/pressure distributions). Usually, for a given pair of values of n_1' and α_0 (corresponding to a given operating point n_1^*, Q_1^*), the cavitation cloud firstly appears as a central filament (Figure 5-13) then changes into the pattern of a rotating spiral vortex rope (Figure 5-14) with further σ_v reduction and finally changes into an inversely conic cavity (Figure 5-15). Sometimes it even presents an unstable situation swinging between different patterns periodically. These cavitation-cloud visualized results of the flow pattern changes just show that the appearance of cloud not only induces the cavitation associated fluctuations (with quite low frequency) but also often changes the flow pattern dramatically, i. e. the influence of cavitation cloud on the flow field. Also, it should be recognized from these observations that the appearance of cavitation cloud is a significant factor contributing to the flow instability as has been described in the venturi study. Therefore, the hypothesis [40] that the appearance of cavitation will not change the flow pattern and the cavitating portion can be evaluated based on the pressure field derived under the non-cavitation condition deviates far from these observations and should not be used without certain limitations.

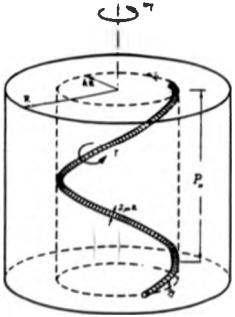

Figure 5-1 Schematic of Vortex Rope in the Draft Tube

[Panelli]

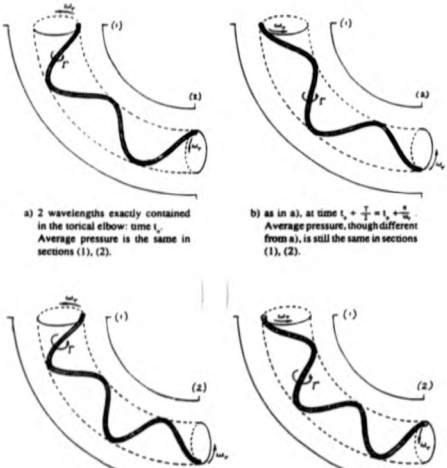

a) 2 wavelengths exactly contained in the torical elbow: time t_o. Average pressure is the same in sections (1), (2).

b) as in a), at time $t_o + \frac{T}{2} = t_o + \frac{\pi}{\omega_o}$. Average pressure, though different from a), is still the same in sections (1), (2).

c) $\frac{1}{2}$ of wavelength exactly contained in the torical elbow: time t_o. Average pressures in sections (1), (2) are different.

d) as in c), at time $t_o + \frac{T}{2} = t_o + \frac{\pi}{\omega_o}$. Average pressure are interchanged, in section (1) and (2), with respect to c).

Figure 5-2 Mechanism of Excitation in the Elbow

[Panelli]

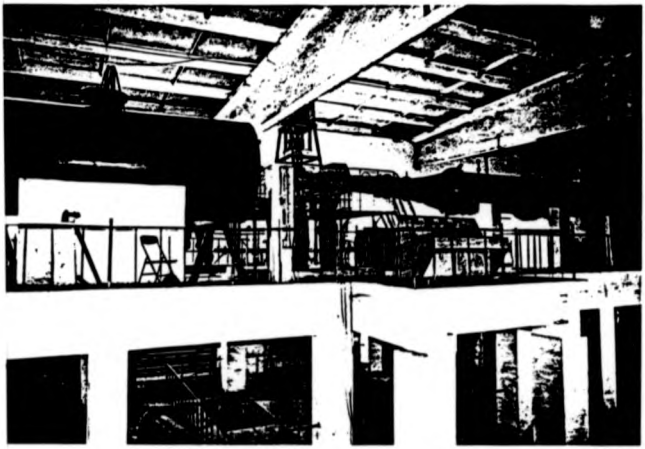

Figure 5-3 Cavitation Test Stand (photo)
(Hydraulic Machinery Lab, NCIWCP, China)

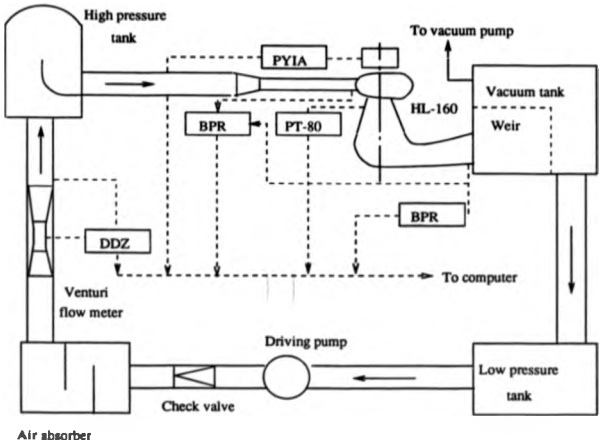

Figure 5-4 Schematic Cavitation Test Stand, NCTWCP, China

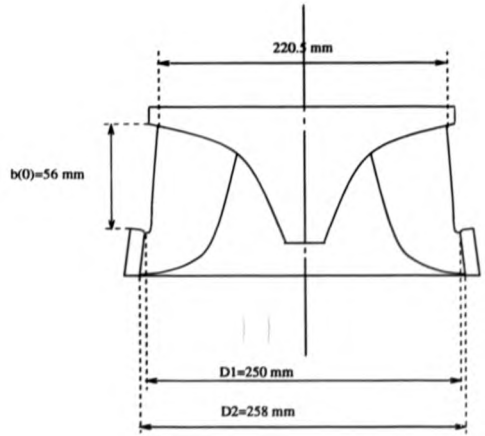

Figure 5-5 Model Runner HL-160-25

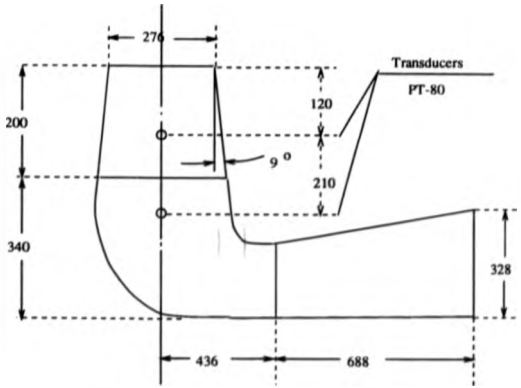

Figure 5-6 Schematic Draft Tube for HL-160-25 Model Runner

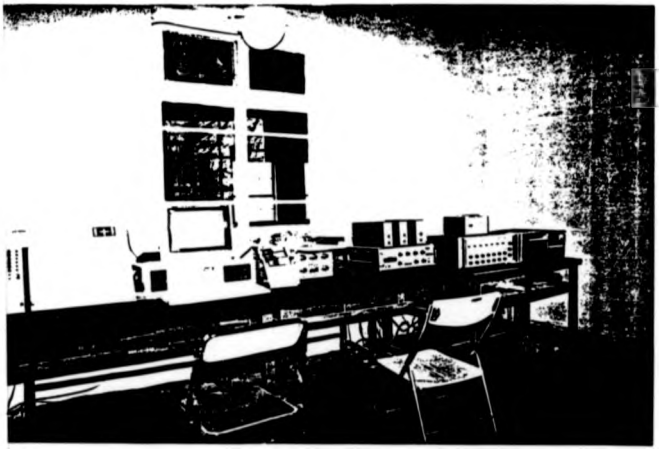

Figure 5-7 Photograph of Data Acquisition and Processing System

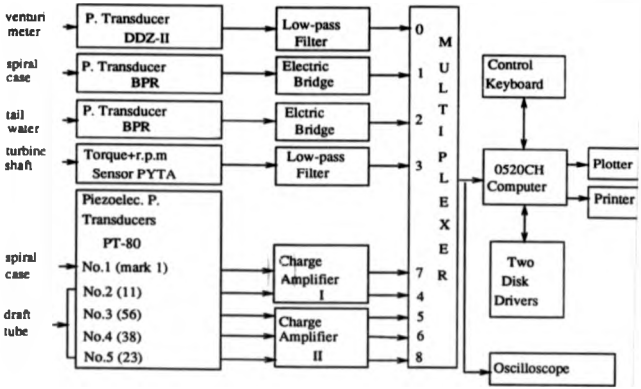

Figure 5-8 Schematic Data Acquisition and Processing System

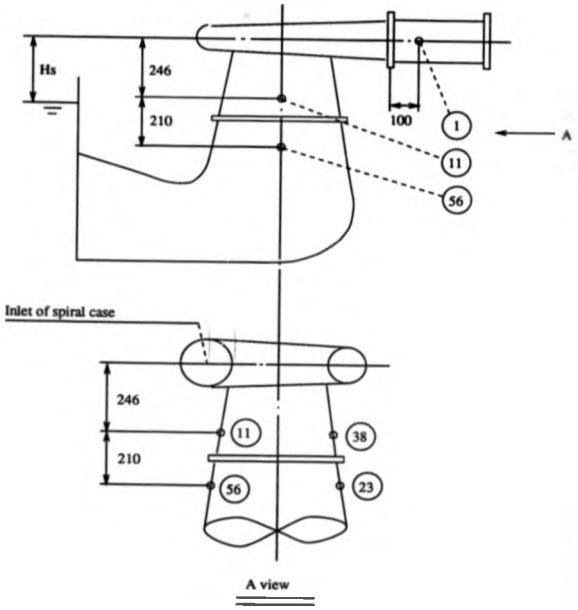

Figure 5-9 Installation of the Piezoelectrical Pressure Transducers on the Inlet of Spiral Case and Draft Tube

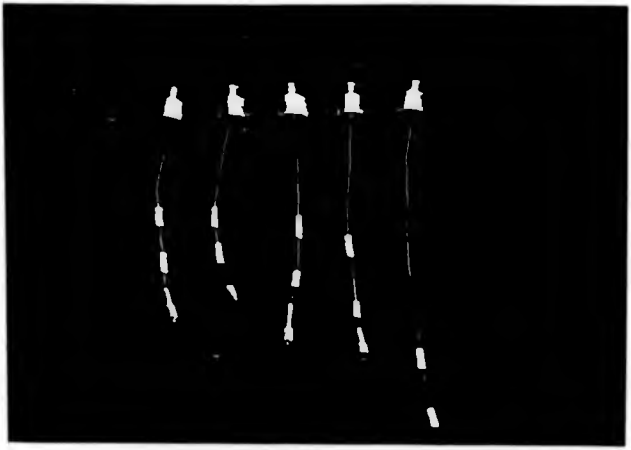

Figure 5-10. Photo of PT-80 Piezoelectrical Transducers

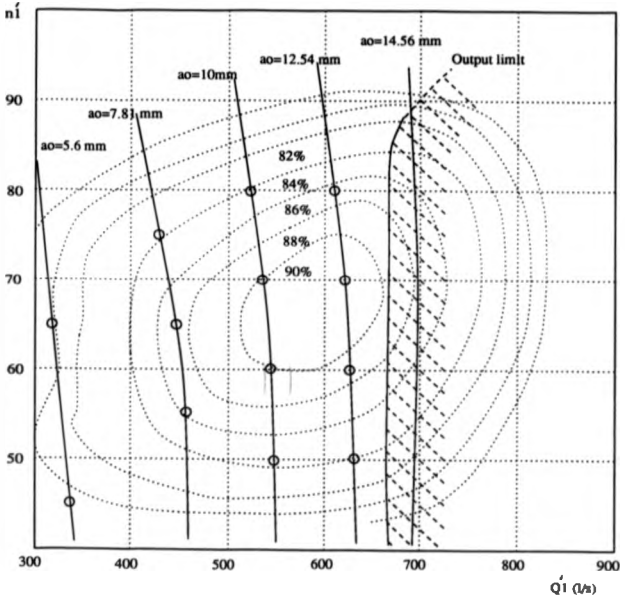

Figure 5-11. Testing Range of HL-160-25

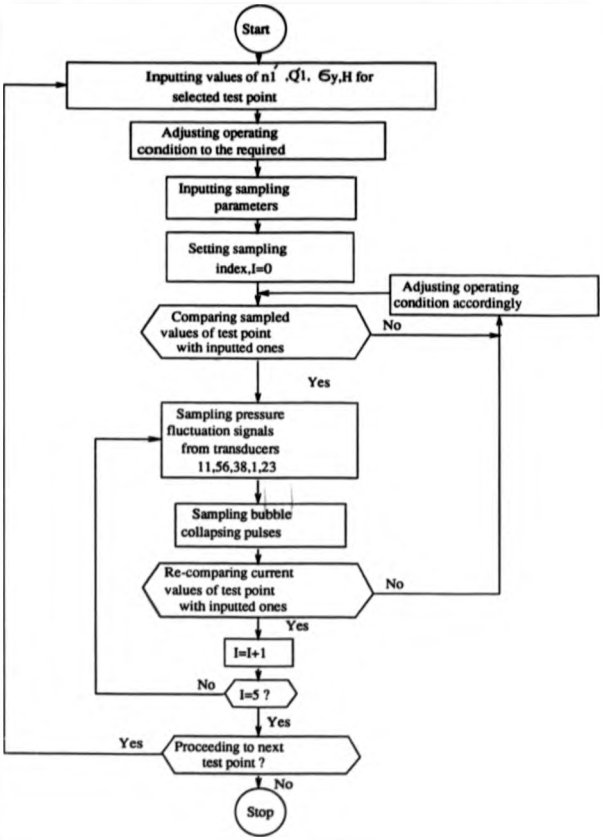

Figure 5-12. Main Flow Chart of Sampling Procedure

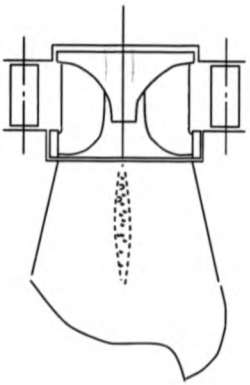

Figure 5-13. (Cavitating) Central Vortex Filament, a_0=10 mm, n_1'=51.03 rpm, σ_y=1.235

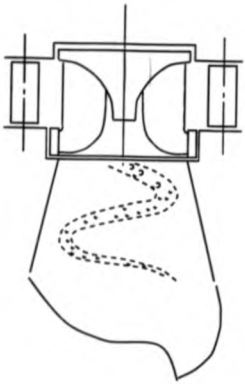

Figure 5-14. (Cavitating) Spiral Vortex Rope. a_0=10 mm, n_1'=81.65 rpm, σ_y=1.156

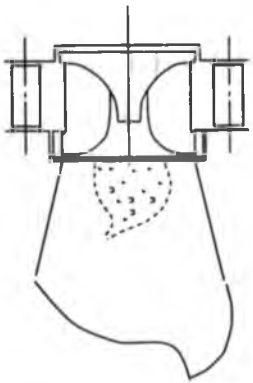

Figure 5-15. (Cavitating) Inversely Conic Cavity, a_0=7.81 mm, n_1'=66.34 rpm, σ_v=1.32

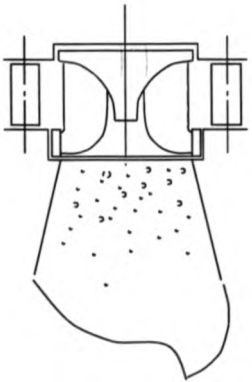

Figure 5-16. Dispersive Liquid-vapour/gas Flow, d_e=5.6 mm, n_1'=45.93 rpm, σ_y=1.09

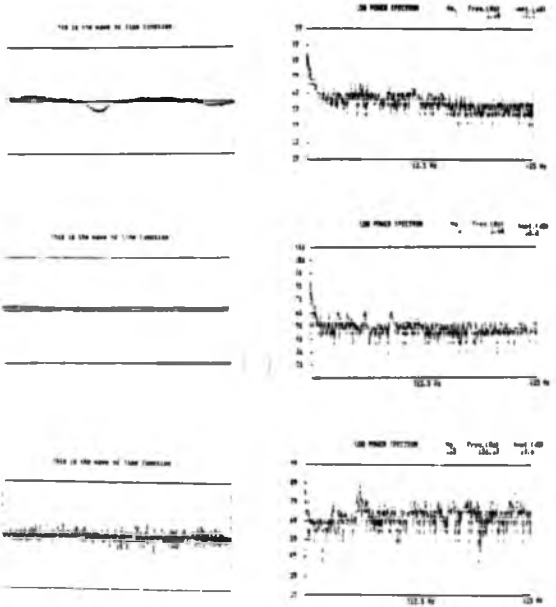

Figure 5-17 Waveforms and Spectra of F_1 component at a_0=5.6 mm, n_1'=66.34 rpm, σ_y=1.18

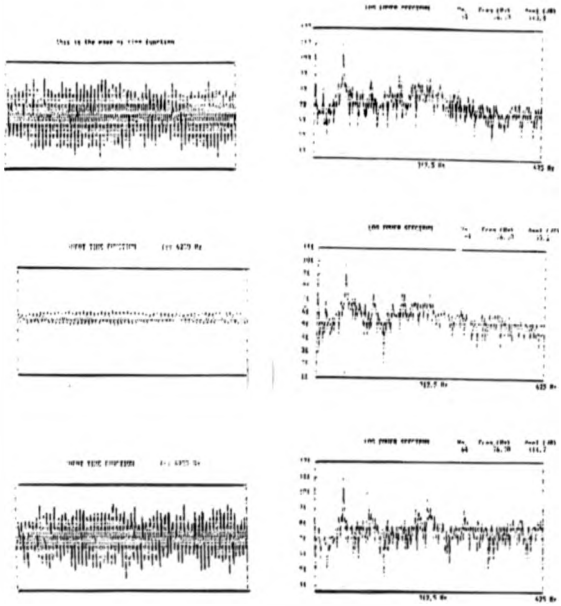

Figure 5-18. Waveforms and Spectra of F_2 Component for a_e=5.5 mm, n_1=45.93 rpm, σ_y=1.32

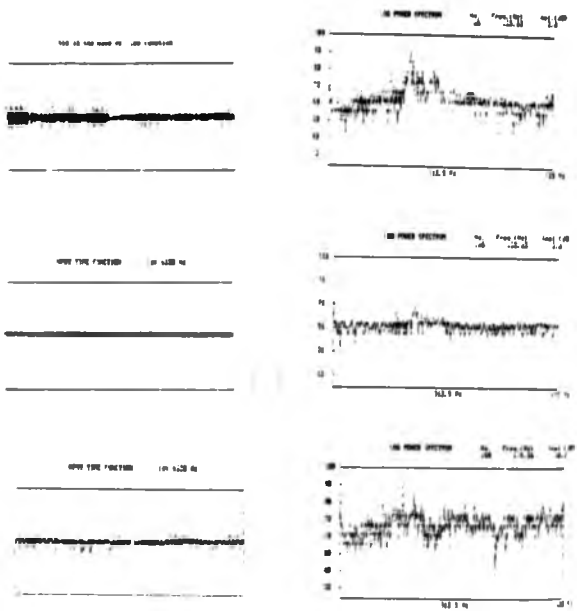

Figure 5-19. Waveforms and Spectra of Component F_1 for a_{ge}=12.54 mm, n_1'=51.03 rpm, ω_2=1.59

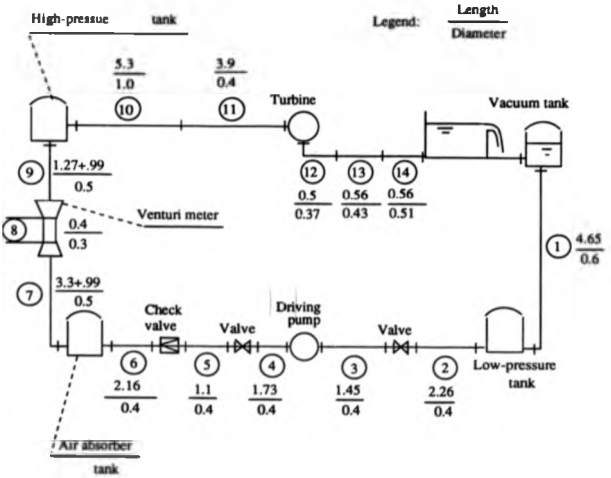

Figure 5-20. Schematization of HL-160-25 Cavitation Test Stand

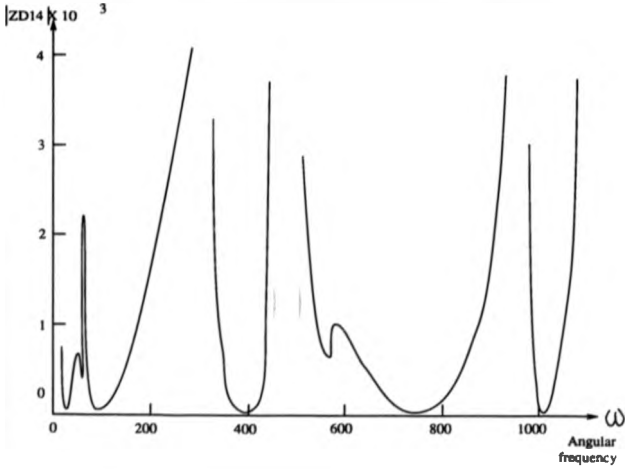

Figure 5-21. Approximation of Natural Frequencies for HL-160-25 Cavitation Test Stand

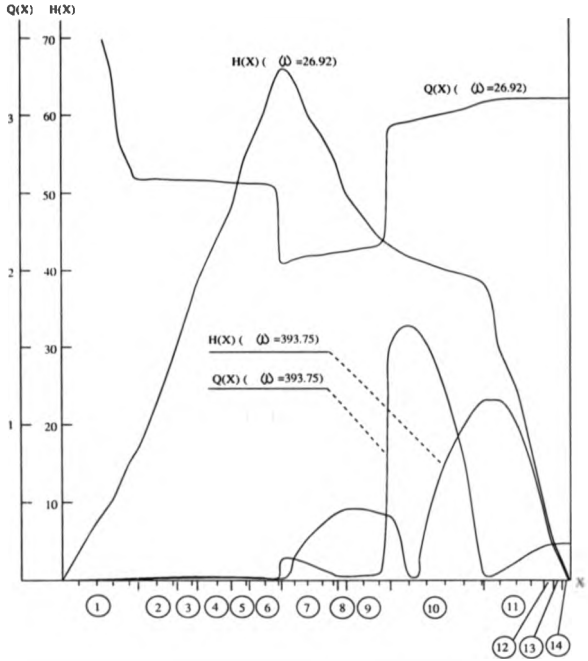

Figure 5-22 Vibration Shape Modes of HL-160-25 System for $s_1=-0.8\omega_1 26.92$ and $s_2=-0.36\omega_1 393.75$

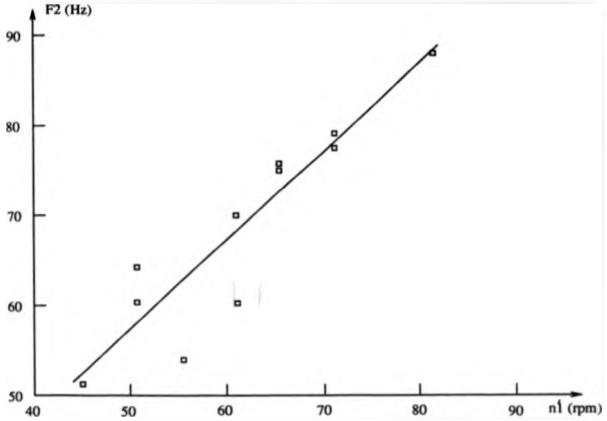

Figure 5-23. Dependence of F_2 Frequency on Unit Speed n_1'

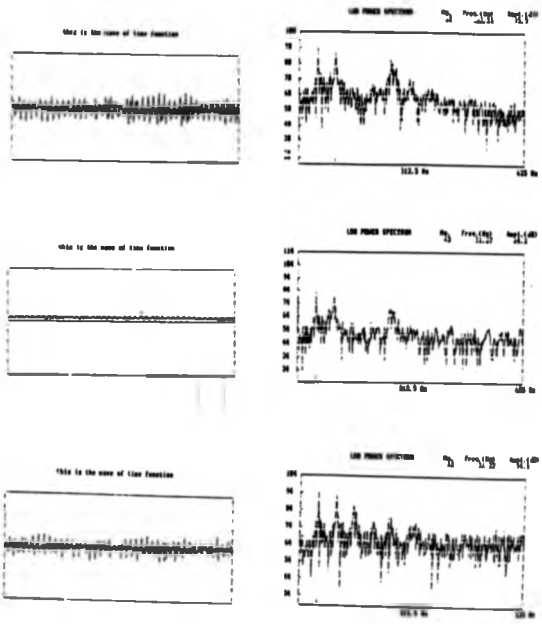

Figure 5-24. Waveform and Spectra for a_{ep}=7.81 mm, n_1'=56.13 rpm, σ_y=1.285

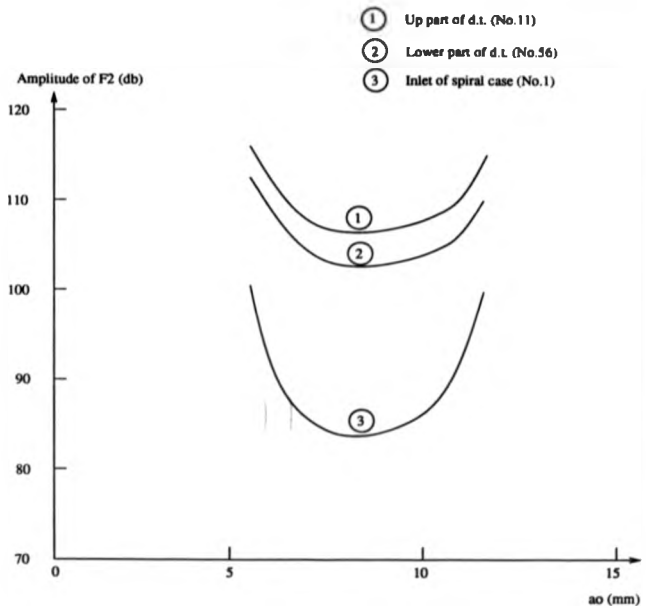

Figure 5-25 Amplitudes (at Different Positions of System) of F_2 Component vs. Guide-vane Opening

Transducer	Sensitivity (mV/kg)		
	1 atm	2 atm	3 atm
No.1	139.32	135.00	128.58
No.11	227.62	220.51	206.80
No.23	119.80	118.80	111.30
No.38	-170.10	-164.80	-162.50
No.56	-262.67	-255.43	-242.34

Table 5-1. Quasi-Dynamic Calibration Results of PT-80 Piezoelectrical Pressure Transducers

6. SUGGESTIONS FOR FURTHER RESEARCH

Due to the fact that the result presented in this thesis is one part of the findings from the author's long-term project *Statistical Characteristics of Cavitation Bubble Collapse Pulses, Associated Low-frequency Fluctuations and Flow Noise*, the following relevant researches have already been done by the author according to the scheme of the long-term project (its objectives have been clearly explained in the Chapter of Introduction).

A The derivation of the expression of the acoustic energy emitted from single collapsing bubble taking account of the liquid compressibility (in collaboration with Zhang) [16].

B The establishment of the Random Pulse Train model considering the effect of the statistical distribution of the original nucleus diameters (in collaboration with Zhang) [16].

C The preliminary investigations of the statistical characteristics of the collapsing pulses of the cavitation-bubble pulses in the venturi cavitating flow and the draft-tube cavitating flow respectively [24,25,41].

According to the plan of the long-term research project, following further investigations should be carried out.

A The investigation into the statistical characteristics of the cavitation pulse field of the cavitation cloud in the venturi cavitating flow. This research should also include the development of the pattern recognition technology for detecting and sorting the waveforms of the collapse pulses (this is being performed by the author).

B The study of the three dimensional effect of the cavitation associated low-frequency fluctuations in the venturi cavitating flow.

C The investigation of the correlation of the statistical characteristics of the cavitation bubble pulses with the cavitation cloud behaviour (i.e. the mutual influences between the micro- and macro attributions of the cavitation behaviour) for some

common cavitating flow types such as the venturi and orifice flows.

D The statistical evaluation of the power of the cavitation pulses in respect of their amplitudes and waveforms. The establishment of the erosion prediction technique taking account of this statistical evaluation.

E The application of the knowledge acquired from the suggested researches on the venturi cavitating flows to the study of the cavitating flows in the hydraulic machinery system especially the draft-tube cavitating flow, leading to the establishments of the three-dimensional mode of the cavitated vortex rope and the relationship between the statistical characteristics of the bubble collapse pulses and the macro behaviour of the cavitated vortex rope.

F For sampling the real value of the pulse pressure emitted from bubble collapses, a special pressure transducer should be searched or invented. Its diameter should be within the order of 1×10^{-1} mm and its frequency response should be higher than 10×10^{6} Hz.

7. CONCLUSIONS

A. The phenomenon of cavitation associated low-frequency fluctuation with its own characteristic frequency is a macro-attribution of the cavitating flows. When cavitation appears, the venturi loop becomes a two portion system --- cavitation cloud portion and liquid phase portion. The natural frequency f_{cav} of the cloud, which is relatively low due to the high elasticity of the cloud, depends on the properties of cavitation cloud such as the wave propagation speed in the cloud, spatial shape and size etc. The strength of the cavitation associated fluctuation component depends on the coupling condition of whole system, i.e. the frequency-response characteristics of the system. When the natural frequencies of both portions coincide, the cavitation resonance results producing huge fluctuations. The one-dimensional linearized model proposed for venturi cavitating flows, which meets the experimental observation quite well, gives a rather clear picture of this phenomenon.

B. The preliminary results from the investigations of cavitation draft-tube flows of HL-160-25 turbine using the knowledge acquired from previous venturi study show that one of the observed fluctuation components, i. e. F_2, is the cavitation associated component which can be distinguished from the other components in following aspects: (1). It shows a strong association nature with cavitation, i.e. it always appears with cavitation and vanishes under non-cavitation conditions. (2). It has higher characterized frequency compared with the fluctuation component described by Rheingans theorem, i.e. $F_2 \gg F_1$. (3). Its frequency varies not only with the machine speed but also with the variation (shape, size and movement) of cavitation cloud.

C. The cavitation association nature of this phenomenon provides the artificially intelligent monitoring system of the hydraulic system with a useful criterion for cavitation detection.

D. For some cavitation flows with complex geometry such as the draft-tube cavitating flows, the three-dimensional effect strongly influences the presentation of this

phenomenon. A three-dimensional model should be pursued.

REFERENCES

1. Arndt, R.E.A., " Cavitation in Fluid Machinery and Hydraulic Structures ", *Ann. Rev. Fluid Mech., 13*, 1981, 273-328, Annual Reviews Inc.
2. Hammitt, F.G., " Cavitation ", *Handbook of Fluids and Fluid Machinery*, John Wiley and Sons, Inc. 1983.
3. Ross, D., *Mechanics of Underwater Noise*, Pergamon Press, New York, 1976.
4. Plesset, M.S. and Prosperetti A., " Bubble Dynamics and Cavitation ", *Ann. Rev. Fluid Mech.*, 9, 1977, 145-185, Annual Reviews Inc.
5. Plesset, M.S., " Physical Effects in Cavitation and Boiling ", *Proc. 1st Symp. Naval Hydrodyn*, Washington, DC, 1956, pp. 297-323.
6. Zarschizky, H., Lauterborn, W., " Digital Picture Processing on High Speed Holograms ", *ICIASF'83 Record*, 1983, pp 49-56.
7. Knapp, R.T., Daily, J.W. and Hammitt, F.G., *Cavitation* , McGraw-Hill, New York, 1970.
8. Rayleigh, L. (Strutt, John William), " On the Pressure Developed in a Liquid During the Collapse of a Spherical Cavity ", *Phil. Mag.* , 34, pp 94-98, Aug. 1917.
9. Porisky, H., " The Collapse and Growth of a Spherical Bubble or Cavity in a Viscous Fluid ", *Proc. First U.S. Nat. Congr. on Appl. Mech.*, 1952 (pp. 813-821)
10. Shu, S.S., " Note on the Collapse of a Spherical Cavity in a Viscous Incompressible Fluid ", *Proc. First U.S. Nat. Congr. Appl. Mech.* (ASME), pp 823-825, 1952.
11. Trilling, L., " The Collapse and Rebound of a Gas Bubble ", *Jr. Appl., Phys., 23*, 14-17, 1952.
12. Gilmore, F.R., " The Growth and Collapse of a Spherical Bubble in a Viscous Compressible Liquid ", *Calif. Inst. of Tech. Hydrodyn. Lab. Rep.* 26-4, 1952.
13. Noltingk, B.E. and Neppiras, E.A., " Cavitation Produced by Ultra-sonics ", *Proc. Phys. Soc. London*, 63B, 674-685, 1950.

14. Hickling, R. and Plesset, M.S., " Collapse and Rebound of a Spherical Bubble in Water ", *Phys. Fluids, 7*, 7-14, 1964.

15. Naude, C.F. and Ellis, A.T., " On the Mechanism of Cavitation Damage by Nonhemispherical Cavities Collapsing in Contact with a Solid Boundary ", *Trans. ASME*, 83, Ser. D. *Jr. Basic Engineering*, 648-656, 1961.

16. Zhang, Y.J. and Li, S.C., " Statistical Investigation of Bubble Collapse and Cavitation Erosion Effect ", *Int. Symp. on Cavitation*, Sendai, Japan. 1986.

17. Il'ichev, V.I. and Lesunovskii,V.P., " On the Noise Spectra Associated with Hydrodynamic Cavitation ", *Akust. Zh., 91*, pp 32-36, 1963.

18. Morozov, V.P., " Cavitation Noise as a Train of Sound Pulses Generated at Random Times ", *Soviet Physics- Acoustics, Vol 14, No.3*, pp 361-365, 1969.

19. Tomita, Y., Shima, A., and Sugiv, T., " Mechanisms of Impulsive Pressure Generation and Damage Pit Formation by Bubble-Shock Wave Interaction ", *Proc. Int. Symp. on Cavitation*, Sendai, Japan, 1986.

20. Dear, J. and Field, J., " A Study of the Collapse of Cavitation Using Two-Dimensional Gelatin Configurations ", *Int. Sym. on Cavitation*, Sendai, Japan, 1986.

21. Okada, T., Iwai, Y., Yamamoto, A., " A Study of Cavitation Erosion of Cast Iron ", *Wear*, 84 (1983).

22. Okada, T. et'al " Fundamental Studies on Cavitation Erosion ", *Bull. JSME. 20* (147) (1977).

23. He, J., Hammitt, F.G., " Comparison of Cavitation Erosion Test Results from Venturi and Vibratory Facilities ", *Wear, 76* (1982).

24. Li, S.C., Zhang, Y.J., and Hammitt, F.G. " Characteristics of Cavitation Bubble Collapse Pulses, Associated Pressure Fluctuation, and Flow Noise ", *DRDA Rept. No UMICH 014571-57-I*, University of Michigan, Ann Arbor, U.S.A. 1982; also

available *Journal of Hydraulic Research, Vol. 24*, 1986, No.2.

25. Li, S.C., " Pressure Pulsation of Cavitation " *Cavitation in Hydraulic Turbines* (in Chinese), Chap. 3. Hydro-electric Press, Beijing, 1984.

26. Li, S.C. et'al, " Cavitation Associated Low-frequency Pressure Fluctuation and Cavitation Resonance in Hydraulic Machinery Flow System ", *Proc. Inaugural Meeting of Int. Editorial Committee for Book Series on Hydraulic Machinery*, 1986, Beijing, China.

27. Hammitt, F.G., *Cavitation and Multiphase Flow Phenomena*, Adv. Book Series, McGraw-Hill, New York, 1980.

28. Lauterborn, W., and Ebeling, K.J., " High Speed Holography of Laser-Induced Cavitation Bubbles in Liquids ", *Proc. 7th. Int. Symp. on Nonlinear Acoustics*, Blacksburg, 1976.

29. Kling, C.L., " A Photographic Study of Spark-induced Cavitation Bubble Collapse ", *Trans. ASME. J. Basic Engr, D. 94*, 4, Dec. 1972.

30. Li, S.C., Zhang, Y.J., Hammitt, F.G., " An Alternative Indicator of Cavitation Inception for Venturi Flow ", *Proc. Int. Symp. on Propulsion and Cavitation*, China, 1986.

31. Li, S.C. , Zhang, Y.J. Hammitt, F.G., " Statistical Consideration of Pressure Pulses from a Cavitating Venturi ", *Proc. Instn. Mech. Engrs, Vol.200, No. C6*, 1986.

32. Van Wijngaarden, L., " One Dimensional Flow of Liquids Containing Small Gas Bubbles ", *Ann. Rev. Fluid Mech. 4*, 369, 1972.

33. Van Wijngaarden ," Sound and Shock Waves in Bubble Liquids ", *Cavitation and Inhomogeities in Underwater Acoustics*, Spring Series in Electrophysics Vol. 4, Berlin Heidelberg, New York, 1980.

34. Oldenziel, D.M., " Bubble Cavitation in Relation to Liquid Quality ", *Thesis*, Twente University of Technology, Enschede, 1979.

35. Ivany, R.D., Hammitt, F.G., " Cavitation Bubble Collapse in Viscous, Compressible Liquids --- Numerical Analyses ", *Trans. ASME. J. Basic Engr, D. 87*, 4, 1965.

36. Mallock, A., " The Damping of Sound by Frothy Liquid ", *Proc. Roy. Soc, A84*, 1910.

37. Wylie, E.B., Streeter, V.L., *Fluid Transients*. Advanced Book Progress, 1978, McGraw-Hill, New York.

38. Jaeger, C., " A Review of Surge-Tank Stability Criteria ", *J. Basic Eng, Trans. ASME*, Dec. 1960.

39. Rheingans, " Power Swings in Hydroelectric Power Plants ", *Trans. ASME, Vol. 62*, 1940.

40. Fanelli, M., " The Vortex Rope in the Draft Tube of Francis Turbines Operating at Partial Load: A Proposal for a Mathematical Model ", *J. Hyd. Res. Vol. 27*, 1989.

41. Li, S.C., " Draft-tube Cavitating Flow of HL-160-25 Turbine " (in Chinese), *Report to the Ministry of Water Resources and Power (National Research Grant No. 87022190 of Water and Power)*, China, 1989.

42. Kornfeld, M., Suvarov, L., " On the Destructive Action of Cavitation ", *Jr. Appl. Phys.*, 15, 495-503, 1944.

43. Plesset, M. S., Chapman, R. B., " Collapse of a Vapour Cavity in the Neighbourhood of a Solid Wall ", *J. Fluid Mech.*, Vol.2, No.47, p.238, May, 1971.

44. Mitchell, T. M., Hammitt, F. G., " Collapse of a Spherical Bubble in a Pressure Gradient ", *1970 ASME Cavitation Forum*, pp.44-46, 1970.

45. Tulin, M. P., " On the Creation of Ultra-Jets ", L. I. Sedov 60th Anniversary Volume, *Problems of Hydrodynamics and Continuum Mechanics*, Moscow, 1969, pp.725-747.

46. Hansson, I., Morch, K. A., " The Dynamics of Cavity Clusters in Ultrasonic (Vibratory) Cavitation Erosion ", *Journal of Applied Physics*, Vol.51, Sept. 1980,

pp.4651-4658.

47. Lush, P. A., Hutton, S. P., " The Relation between Cavitation Intensity and Noise in a Venturi-type Section ", *Proc. Int'l Conf. on Pump and Turbines*, Sept. 1976, pp.1-11, NEL, Glasgow.

48. De, M. K., Hammitt, F. G., " New Method for Monitoring and Correlating Cavitation Noise to Erosion Capability ", *Trans. ASME, J. Fluid Engr.*, 104, 4, 1982.

49. Oba, R., Uvanishi, K., Yasu, S., " Johnson Effects in Cavitating Flow through an Orifice with Enormous-Pressure-Fluctuations ", *Rep. Inst. High Speed Mech.*, Vol.44, No.343, 1981.

50. Prosperetti, A., " Thermal Effects and Damping Mechanisms in the Forced Radial Oscillations of Gas Bubbles in Liquids ", *J. Acoust. Soc. Am.*, Vol.61, No.1, pp.17-27, 1977.

51. Chapman, R. B., Plesset, M. S., " Thermal Effects in the Free Oscillation of Gas Bubble ", *J. Basic. Eng.*, Vol.93, pp.373-376, 1971.

52. Lauterborn, W., " Numerical Investigation of Nonlinear Oscillations of Gas Bubbles in Liquids ", *J. Acoust. Soc. Am.*, Vol.59, pp.283-293, 1976.

53 Borotnikova, M. I., Soloukin, R.I., 1964. *Sov. Phys. Acoust.* 10:28-32.

54 Fujikawa, S., et'al, " Interactions between Two Slightly Nonspherical Bubbles in a Compressible Liquid ", *Proc. Int. Symp. on Cavitation*, Sendai, Japan, 1986.

55 Henry, P. et'al, " Scale Effect Concerning Hydraulic Quasi-Stationary Oscillations on a Turbine Model and Test Circuit ", *Proc. 12th IAHR Symp. Hydraulic Machinery and Cavitation*, Stirling, 1984.

56 Prenat, J-E. et'al, " High Load Behaviour of a Francis Turbine Model and Scale Effect ", *Proc. 13th IAHR Symp. Hydraulic Machinery and Cavitation*, Montreal, 1986.

57 Jacob, T. et'al, " A Characterization Procedure for the Dynamic Behaviour of Francis Turbines: Practical Comparison of Elbow and Moody Type Draft Tubes ", *Proc. 14th IAHR Symp. Hydraulic Machinery and Cavitation*, Trondheim, 1988.

APPENDICES

A. Programs for Numerical Study of Frequency Response of Venturi Loop

Frequency Scan

```
      IMPLICIT COMPLEX(Z)
      DIMENSION AL(12),D(12),PZ(3)
      COMMON/AA/ AL,D,FN,Q
      AL(1)=0.43
      AL(2)=1.52
      AL(3)=0.56
      AL(4)=0.61+0.305
      AL(5)=0.0765
      AL(6)=0.0576
      AL(7)=0.0455
      AL(8)=0.094
      AL(9)=0.094
      AL(10)=1.85
      AL(11)=0.61+0.406
      D(1)=0.127
      D(2)=0.0762
      D(3)=0.102
      D(4)=0.102
      D(5)=0.0256
      D(6)=0.013
      D(7)=0.0153
      D(8)=0.0227
      D(9)=0.0329
      D(10)=0.051
      D(11)=0.051
      FN=0.018

      Q=0.0051
      ZS=CMPLX(0.,330.)

      WRITE(*,3)
3     FORMAT(1X,          SIGM                OMG
     *  ABS(ZD)  )
      K=1
      KL=0
      DO 100 I=1,3
      ZS=ZS+(0.,10.)
      CALL ZD12(ZS,ZD)
      PZ(K)=CABS(ZD)
      K=K+1
100   CONTINUE
```

```
170     IF(PZ(2).LT.PZ(1).AND.PZ(2).LT.PZ(3)) GOTO 150
        IF(PZ(2).GT.PZ(1).AND.PZ(2).GT.PZ(3)) GOTO 150
160     PZ(1)=PZ(2)
        PZ(2)=PZ(3)
        ZS=ZS+(0.,10.)
        CALL ZD12(ZS,ZD)
        PZ(3)=CABS(ZD)
        GOTO 170
150     KL=KL+1
        ZS2=ZS-(0.,10.)
        WRITE(*,'(2F20.10,F20.8)') ZS2,PZ(2)
        IF(KL.GE.8) GOTO 180
        GOTO 160
180     STOP
        END

        SUBROUTINE ZD12(ZS,ZD)
        IMPLICIT COMPLEX(Z)
        DIMENSION AL(12),D(12)
        COMMON/AA/ AL,D,FN,Q
        SAVE /AA/
        ZU1=CMPLX(0.,0.)
        CALL ZDU(ZU1,AL(1),D(1),FN,Q,ZS,ZD1)
        PM=0.087
        ZU2=ZD1+PM
        CALL ZDU(ZU2,AL(2),D(2),FN,Q,ZS,ZD2)
        CALL ZDU(ZD2,AL(3),D(3),FN,Q,ZS,ZD3)
        VR1=0.0154
        CALL ZUDA(ZS,ZD3,VR1,ZU4)
        CALL ZDU(ZU4,AL(4),D(4),FN,Q,ZS,ZD4)
        CALL ZDU(ZD4,AL(5),D(5),FN,Q,ZS,ZD5)
        CALL ZDU(ZD5,AL(6),D(6),FN,Q,ZS,ZD6)
        CALL ZDU(ZD6,AL(7),D(7),FN,Q,ZS,ZD7)
        CALL ZDU(ZD7,AL(8),D(8),FN,Q,ZS,ZD8)
        CALL ZDU(ZD8,AL(9),D(9),FN,Q,ZS,ZD9)
        CALL ZDU(ZD9,AL(10),D(10),FN,Q,ZS,ZD10)
        BM=2.*1.27/0.0051
        ZU11=ZD10-BM
        CALL ZDU(ZU11,AL(11),D(11),FN,Q,ZS,ZD11)
        VR2=0.0297
        CALL ZUDA(ZS,ZD11,VR2,ZU12)
        ZD=ZU12
        RETURN
        END
```

```
SUBROUTINE ZDU(ZU,AL,D,F,Q,ZS,ZD)
IMPLICIT COMPLEX(Z),REAL(L)
AF=0.7854*D*D
A1=2.02E9/998.26
A2=2.02E9/(9.80E10*2.E-3)
A=SQRT(A1/(1.+A2*D))
C=9.81*AF/(A*A)
L=1./(9.81*AF)
R=F*Q/(9.81*D*AF*AF)
ZGAM=CSQRT(ZS*CMPLX(C,0.)*(CMPLX(L,0.)*ZS+CMPLX(R,0.)))
ZC=ZGAM/(CMPLX(C,0.)*ZS)
ZEXP=CEXP(ZGAM*CMPLX(AL,0.))
ZTH=(ZEXP-CMPLX(1.,0.)/ZEXP)/(ZEXP+CMPLX(1.,0.)/ZEXP)
ZD=(ZU-ZC*ZTH)/(CMPLX(1.,0.)-ZU*ZTH/ZC)
RETURN
END

SUBROUTINE ZUDA(ZS,ZD,V,ZU)
IMPLICIT COMPLEX(Z)
ZA=CMPLX(-2.02E9,0.)/(CMPLX(9800.,0.)*CMPLX(V,0.)*ZS)
ZU=ZD*ZA/(ZD+ZA)
RETURN
END
```

Newton Iteration and Mode Shape

```
      IMPLICIT COMPLEX(Z)
        DIMENSION ZF(2),AL(14),D(12),ZU(12),ZD(12)
        DIMENSION ZC(20),ZCH(20),ZSH(20)
        DIMENSION ZHU(20),ZQU(20),ZHD(20),ZQD(20)
        DIMENSION NJ(20),OMN(20)
        COMMON/AA/ AL,D,FN,Q
        AL(1)=0.43
        AL(2)=1.52
        AL(3)=0.56
        AL(4)=0.61+0.305
        AL(5)=0.0765
        AL(6)=0.0576
        AL(7)=0.0455
        AL(8)=0.094
        AL(9)=0.094
        AL(10)=1.83
        AL(11)=0.61+0.406
        D(1)=0.127
        D(2)=0.0762
        D(3)=0.102
        D(4)=0.102
        D(5)=0.0256
        D(6)=0.013
        D(7)=0.0153
        D(8)=0.0227
        D(9)=0.0329
        D(10)=0.051
        D(11)=0.051
        FN=0.018
        Q=0.0051
      *
      OMN(1)=380.
      OMN(2)=920.
      OMN(3)=1860.
      OMN(4)=2160.
      NOM=4
      DO 500 JJ=1,NOM
      SIG=-0.1
      OM=OMN(JJ)
        DS=0.01
        DOM=0.01
        ZS=CMPLX(SIG,OM)
        ZEP=CMPLX(DS,DOM)
      *
        N=0
        NIT=8
        TOL=0.03
        KFIN=0
```

```
29      K=1
30      CALL ZD1(ZS,ZU,ZD,ZC,ZCH,ZSH,PM,BM)
        ZF(K)=ZD(12)
        IF(KFIN.EQ.1) GOTO 70
        IF(K.EQ.2) GOTO 60
        K=2
        ZSS=ZS
        ZS=ZS+ZEP
        GOTO 30
60      ZDS=-ZEP*ZF(1)/(ZF(2)-ZF(1))
        ZS=ZSS+ZDS
        N=N+1
        IF(N.GT.NIT) GOTO 134
        IF(CABS(ZF(1)).GT.TOL) GOTO 29
      ZS=ZS-ZDS
        KFIN=1
        GOTO 29
70    WRITE(*,71) OMN(JJ)
71    FORMAT(' THE RESULTANT VALUE FROM THE ITERA FOR THE SCANNED FREQEN
     2CY 0+i',F6.1,' IS',)
      WRITE(*,72) REAL(ZS),AIMAG(ZS)
72    FORMAT('                              ZS=',F5.2,'+i',F7.2)
      WRITE(*,73) AIMAG(ZS)
73    FORMAT(' THE MODE SHAPE FOR OMG=',F7.2,' IS COMPUTED AS FOLLOW')
        MDJJ=1.0
        ZNU(8)=CMPLX(MDJJ,0.)
        ZQU(8)=ZNU(8)/ZU(8)
        DO 100 I=9,10
        ZQU(I)=-ZNU(I-1)*ZSH(I-1)/ZC(I-1)+ZQU(I-1)*ZCH(I-1)
        ZNU(I)=ZQU(I)*ZU(I)
100     CONTINUE
        ZQD(10)=-ZNU(10)*ZSH(10)/ZC(10)+ZQU(10)*ZCH(10)
        ZND(10)=ZQD(10)*ZD(10)
        ZNU(11)=ZND(10)-BM*ZQD(10)
        ZQU(11)=ZNU(11)/ZU(11)
*
        DO 200 I=1,6
        K=8-I
        ZQU(K)=ZNU(K+1)*ZSH(K)/ZC(K)+ZQU(K+1)*ZCH(K)
        ZNU(K)=ZQU(K)*ZU(K)
200     CONTINUE
        ZND(1)=ZNU(2)-PM*ZQU(2)
        ZQD(1)=ZQU(2)
        ZQU(1)=ZND(1)*ZSH(1)/ZC(1)+ZQD(1)*ZCH(1)
        ZNU(1)=ZQU(1)*ZU(1)
```

```
      DO 110 I=1,4
      NJ(I)=AL(I)/0.3+1
110   CONTINUE
      DO 111 I=5,9
      NJ(I)=AL(I)/0.03+1
111   CONTINUE
      DO 112 I=10,11
      NJ(I)=AL(I)/0.3+1
112   CONTINUE

      WRITE(*,9)
9     FORMAT(1H0,'   PIPE      X      HEAD      PHIH         Q      PHIQ
     2 ABSZ')
      DX=0.3
      DO 120 J=1,4
      ZEXP=ZCH(J)+ZSH(J)
      ZGAM=CLOG(ZEXP)/AL(J)
      N1=NJ(J)
      X=-DX
      DO 120 I=1,N1
      X=X+DX
      ZEXP=CEXP(ZGAM*X)
      ZCHX=0.5*(ZEXP+1./ZEXP)
      ZSHX=0.5*(ZEXP-1./ZEXP)
      ZH=ZHU(J)*ZCHX-ZQU(J)*ZC(J)*ZSHX
      ZQ=-ZHU(J)*ZSHX/ZC(J)+ZQU(J)*ZCHX
      ZZ=ZH/ZQ
      QU=CABS(ZQ)*1000.
      HU=CABS(ZH)
      ABSZ=CABS(ZZ)
      PHIQ=ATAN2(AIMAG(ZQ),REAL(ZQ))
      IF(CABS(ZH).EQ.0.) GOTO 120
      PHIH=ATAN2(AIMAG(ZH),REAL(ZH))
120   WRITE(*,'(I5,F9.2,4F9.3,F12.1)')J,X,HU,PHIH,QU,PHIQ,ABSZ
      DX=0.03
      DO 125 J=5,9
      ZEXP=ZCH(J)+ZSH(J)
      ZGAM=CLOG(ZEXP)/AL(J)
      N1=NJ(J)
      X=-DX
      DO 125 I=1,N1
      X=X+DX
      ZEXP=CEXP(ZGAM*X)
      ZCHX=0.5*(ZEXP+1./ZEXP)
      ZSHX=0.5*(ZEXP-1./ZEXP)
      ZH=ZHU(J)*ZCHX-ZQU(J)*ZC(J)*ZSHX
      ZQ=-ZHU(J)*ZSHX/ZC(J)+ZQU(J)*ZCHX
      ZZ=ZH/ZQ
      QU=CABS(ZQ)*1000.
```

```
        HU=CABS(ZH)
        ABSZ=CABS(ZZ)
        PHIQ=ATAN2(AIMAG(ZQ),REAL(ZQ))
        PHIH=ATAN2(AIMAG(ZH),REAL(ZH))
      WRITE(*,'(I5,F9.2,4F9.3,F12.1)')J,X,HU,PHIH,QU,PHIQ,ABSZ
125     CONTINUE
        DX=0.3
        DO 130 J=10,11
        ZEXP=ZCH(J)+ZSH(J)
        ZGAM=CLOG(ZEXP)/AL(J)
        N1=NJ(J)
        X=-DX
        DO 130 I=1,N1
        X=X+DX
        ZEXP=CEXP(ZGAM*X)
        ZCHX=0.5*(ZEXP+1./ZEXP)
        ZSHX=0.5*(ZEXP-1./ZEXP)
        ZH=ZHU(J)*ZCHX-ZQU(J)*ZC(J)*ZSHX
        ZQ=-ZHU(J)*ZSHX/ZC(J)+ZQU(J)*ZCHX
        ZZ=ZH/ZQ
        QU=CABS(ZQ)*1000.
        HU=CABS(ZH)
        ABSZ=CABS(ZZ)
        PHIQ=ATAN2(AIMAG(ZQ),REAL(ZQ))
        PHIH=ATAN2(AIMAG(ZH),REAL(ZH))
      WRITE(*,'(I5,F9.2,4F9.3,F12.1)')J,X,HU,PHIH,QU,PHIQ,ABSZ
130     CONTINUE
      GOTO 140
134   WRITE(*,135) N,OMN(JJ)
135   FORMAT(' SOLUTION DID NOT CONVERGE TO ROOT IN',I3,'ITERATIONS
     2THE SCANNED FREQENCY OMG=',F7.2)
140   WRITE(*,131)
131   FORMAT('
      WRITE(*,132)
132   FORMAT('              ---------------------------------------
      WRITE(*,133)
133   FORMAT('
500   CONTINUE
        STOP
        END
```

```
      SUBROUTINE ZD1(ZS,ZU,ZD,ZC,ZCH,ZSH,PM,BM)
      IMPLICIT COMPLEX(Z)
      DIMENSION AL(14),D(12),ZU(12),ZD(12),ZC(20)
      DIMENSION ZCH(20),ZSH(20)
      COMMON /AA/AL,D,FN,Q
      SAVE /AA/
      ZU(1)=(0.,0.)
      CALL ZDU(ZU(1),AL(1),D(1),FN,Q,ZS,ZD(1),ZC(1),ZCH(1),ZSH(1))
      PM=0.087
      ZU(2)=ZD(1)+PM
      CALL ZDU(ZU(2),AL(2),D(2),FN,Q,ZS,ZD(2),ZC(2),ZCH(2),ZSH(2))
      ZU(3)=ZD(2)
      CALL ZDU(ZU(3),AL(3),D(3),FN,Q,ZS,ZD(3),ZC(3),ZCH(3),ZSH(3))
      VR1=0.0154
      CALL ZUDA(ZS,ZD(3),VR1,ZU(4))
      DO 105 I=4,10
      CALL ZDU(ZU(I),AL(I),D(I),FN,Q,ZS,ZD(I),ZC(I),ZCH(I),ZSH(I))
      ZU(I+1)=ZD(I)
105   CONTINUE
      BM=2.*1.27/0.0051
      ZU(11)=ZD(10)-BM
      CALL ZDU(ZU(11),AL(11),D(11),FN,Q,ZS,ZD(11),ZC(11),ZCH(11),
     2 ZSH(11))
      VR2=0.0297
      CALL ZUDA(ZS,ZD(11),VR2,ZD(12))
      RETURN
      END

      SUBROUTINE ZDU(ZU,AL,D,F,Q,ZS,ZD,ZC,ZCH,ZSH)
      IMPLICIT COMPLEX(Z),REAL(L)
      AF=0.7854*D*D
      A1=2.02E9/998.26
      A2=2.02E9/(19.6E10*2.E-3)
      A=SQRT(A1/(1.+A2*D))
      C=9.81*AF/(A*A)
      L=1./(9.81*AF)
      R=F*Q/(9.81*D*AF*AF)
      ZGAM=CSQRT(ZS*CMPLX(C,0.)*(CMPLX(L,0.)*ZS+CMPLX(R,0.)))
      ZC=ZGAM/(CMPLX(C,0.)*ZS)
      ZEXP=CEXP(ZGAM*CMPLX(AL,0.))
      ZCH=0.5*(ZEXP+1./ZEXP)
      ZSH=0.5*(ZEXP-1./ZEXP)
      ZTH=(ZEXP-CMPLX(1.,0.)/ZEXP)/(ZEXP+CMPLX(1.,0.)/ZEXP)
      ZD=(ZU-ZC*ZTH)/(CMPLX(1.,0.)-ZU*ZTH/ZC)
      RETURN
      END

      SUBROUTINE ZUDA(ZS,ZD,V,ZU)
      IMPLICIT COMPLEX(Z)
      ZA=CMPLX(-2.02E9,0.)/(CMPLX(9800.,0.)*CMPLX(V,0.)*ZS)
      ZU=ZD*ZA/(ZD+ZA)
      RETURN
      END
```

B. Data Acquisition Programs for Low-frequency Fluctuations and Bubble Collapse Pulses of HL160-25 Turbine

```
10 DEF SEG=&H1000
20 BLOAD"100",0
30 DEFSTR C
40 GOSUB 1310
50 '*************************************************
60 WIDTH 80:SCREEN 0,1
70 PRINT "*****************  MAIN  MENU  SELECTION  *****************"
80 PRINT :PRINT:PRINT  "M=0,1,2,3"
90 PRINT
100 PRINT "     0  ---------- Single-channel Sampling ? "
110 PRINT "     1  ---------- Double-channel Sampling ? "
120 PRINT "     2  ---------- D/A Converter Output ? "
130 PRINT "     3  ---------- Stop Sampling ? "
140 PRINT:INPUT "                 M=? ";M
150 IF M=3 THEN END
160 '----------Set up Parameters of DMA ----------
161 LET SG=.09216:HV=.12:HS=-.496:DI=.25
162 PRINT 'INPUT the Pre-selected Values of N1,Q1,H,SGA"
163 INPUT N1,Q1,H,SGA
164 KL=0 :KC=0:K=0 :KS=0
165 T$=TIME$:D$=DATE$
166 OPEN "C:DATA" FOR OUTPUT AS#1
167 WRITE #1,N1,Q1,H,SGA,T$,D$
168 CLOSE#1
169 CLS
170 PRINT TAB(8);"N1" TAB(20);"Q1" TAB(32);"H" TAB(44);"SGA" TAB(56);"TIME"
171 PRINT TAB(68);"DATA"
172 PRINT:PRINT
173 PRINT TAB(8);N1 TAB(18);Q1 TAB(30);H TAB(42);SGA TAB(54);T$ ;
174 PRINT TAB(66);D$
190 GOSUB 2700
191 M=0
195 AF=0
200 CYC=5000
210 LENGTH=2000
220 ADCH=5
240 CYC$=INT(CYC*4!+.5)
250 OUT &H114,AF
260 OUT &HB,&H47
270 OUT 15,14
280 OUT &H107,&HB6
290 OUT &H107,&HF
300 PADD=0
310 PAGE=7
320  DMACH=0
330 IF DMACH=0 THEN DMACH=7
340 IF DMACH=1 THEN OUT &HB3,15
350 IF DMACH=2 THEN OUT &HB1,15
360 IF DMACH=3 THEN OUT &HB2,15
370 IF ADCH=1 THEN OUT &H114,AF:OUT &H110,&H78:GOTO 480
380 IF M=1 THEN ADCH=ADCH*2
```

```
390 OUT &H103,&H54
400 OUT &H110,&H78
410 OUT &H101,ADCH
420 OUT &H103,&H10
430 CHMM=ADCH*AF
440 FOR I=AF TO CHMM
450 OUT &H100,&H35
460 NEXT I
470 GOTO 520
480 OUT &H103,&H14
490 OUT &H103,&H50
500 OUT &H100,&H20
510 OUT &H103,&H14
520 OUT &H107,&HE
530 OUT &H9,&H7
540 OUT &H9,&H7
550 OUT &H9,&H7
560 OUT &H103,&H34
570 OUT DMACH*2,BADD-INT(BADD/256)*256
580 OUT DMACH*2,INT(BADD/256)
590 OUT DMACH*2+1,LENGTH-INT(LENGTH/256)*256
600 OUT DMACH*2+1,INT(LENGTH/256)
610 IF DMACH=1 THEN OUT &H83,PAGE
620 IF DMACH=2 THEN OUT &H81,PAGE
630 IF DMACH=3 THEN OUT &H82,PAGE
635 GOSUB 2700
640 '----------DMA Transfer--------------
650 DMACH%=DMACH
660 DEF SEG=&H1700
670 DMAT=&H0
680 CALL DMAT(DMACH%,CYC%)
690 OUT &H110,&H0
700 OUT &H107,&HF
705 GOSUB 2700
710 GOTO 830
720 '---------Display ( Denary )----------------
730 INPUT "DISPLAY?[Y/N]";X$:IF X$ <>"Y" THEN 820
740 SCREEN 2:SCREEN 0,0,0
750 SEGM=PAGE*4096+INT(BADD/16)
760 DEF SEG=SEGM
770 FOR I=0 TO 200
780 PA1=PEEK(I*2)\16+PEEK(I*2+1)*16
790 IF PA1>2047 THEN PA1=PA1-4096
800 PRINT PA1,
810 NEXT I
830 '---- Test Condition Monitoring and Sampling Initiating -----
840 SEGM=PAGE*4096+INT(BADD/16)
850 DEF SEG=SEGM
860 FOR CH=0 TO ADCH-1
870 DP(CH)=0
880 FOR I=0 TO LENGTH/(2*ADCH)-1  STEP 10
900 L=PEEK(I*2*ADCH+CH*2)\16+PEEK(I*2*ADCH+1+CH*2)*16
```

```
910 IF L)=2048 THEN L=L-4096
920 DP(CH)=L+DP(CH)
930 NEXT I
940 DPA(CH)=DP(CH)/(LENGTH/(2*ADCH))*10
950  DPB(CH)=DPA(CH)*5/2048/2.952293
960  NEXT CH
965 FOR I=0 TO ADCH-1
966 IF DPB(I)<=0 THEN DPB(I)=.0001
967 NEXT I
990 N=DPB(0)/10*9554.474-14.1157
1000 Q=SQR(80353.69*DPB(1)+286.47)/1000 /2.05
1010 H1=Q^2/(2*9.810001*SS^2)+DPB(2)*12.826+.0107
1015 LOCATE 20,20:PRINT H1,H2
1020 H2=DPB(3)*9.579601-.4684
1030 HT=H1-H2+3.19
1035 HT=ABS(HT)
1040 SGA=(N2+10.33-5.43-HS-HV)/HT
1050 NIS=N*D1/SQR(HT)
1060 QIS=Q/(D1 2*SQR(HT))
1065 DB(0)=NIS:DB(1)=QIS:DB(2)=HT:DB(3)=SGA:DB(4)=DPB(4)
1070  FOR CH=0 TO ADCH-1
1080 LOCATE 7+KS,6+12*CH: PRINT INT(DB(CH)*1000+.5)/1000
1090 NEXT CH
1100 LOCATE 7+KS,50:PRINT TAB(54);TIME$ TAB(66):DATE$
1105 LOCATE 11,1
1107 PRINT TAB(6);INT(N*1000+.5)/1000  TAB(18);INT(Q*1000+.5)/1000  TAB(
HT*1000+.5)/1000 TAB(42);INT(SGA*1000+.5)/1000;"REAL N,Q,H,SAG"
1120 IF K<>0 THEN 1210
1125 LOCATE 9,1
1125 PRINT "PRESS ANY KEY TO START MAIN SAMPLING PROGRAM IF TEST CONDITIO
1130 SS2$=INKEY$:IF SS2$="" THEN 190
1131 FOR I=0 TO ADCH-1
1132 LET DC(I)=DB(I)
1133 NEXT I
1135 K3=KS+2
1136 T1$=TIME$:D1$=DATE$
1138 LOCATE 9,1:PRINT  SPACE$(80)
1210 GOSUB 1410
1270 SOUND 261,2 :KL=KL+1
1280 GOSUB  2250
1290 IF KL=6 THEN 2371
1300 GOTO 190
1310 '---------- Title Printing ----------------
1320 SCREEN 1,0:CLS: KEY OFF
1330 LINE (25,20)-(295,120),,B
1340 LINE (20,24)-(291,116),,B
1350 LOCATE 7,16:PRINT "HSH--ADC4P"
1360 LOCATE 10,6:PRINT "ADC4P CONVERTER BOARD SOFTWARE "
1370 LOCATE 20,3
1380 PRINT"Hydraulic Machinery Lab., NCIWCP, China, Oct. 1980"
1390 SS1$=INKEY$:IF SS1$="" THEN GOTO 1390
1400 RETURN
1410 '----------- Set up the Parameters of DMA -----------
1415 IF KL=5 THEN T2$=TIME$:D2$=DATE$
```

```
1420 M=0
1430 IF KL=5 THEN CHNO1=8 :GOTO 1450
1440 CHNO1=4
1450 IF KL=5 THEN CXC=7:GOTO 1470
1460 CXC=16
1470 CYC%=INT(CXC*4!+.5)
1480 OUT &H114,CHNO1
1490 OUT &H8,&H47
1500 OUT 15,14
1510 OUT &H107,&HB6
1520 OUT &H107,&HF
1530 BADD=0
1540 IF KL=5 THEN LETH=50000!:GOTO 1560
1550 LETH=60000!
1560 PAGE =2
1570 DMACH=3
1575 OUT &H82,15
1580 IF KL=5 THEN ADCH2=1:GOTO 2800
1590 ADCH2=5
1610 OUT &H103,&H54
1620 OUT &H110,&H78
1630 OUT &H101,ADCH2
1640 OUT &H103,&H18
1650 CHMM=ADCH2*CHNO1
1660 FOR I=CHNO1 TO CHMM
1670 OUT &H100,&H33
1680 NEXT I
1690 OUT &H107,&HE
1700 OUT &H9,&H7
1710 OUT &H9,&H7
1720 OUT &H9,&H7
1730 OUT &H103,&H34
1740 OUT DMACH*2,BADD-INT(BADD/256)*256
1750 OUT DMACH*2,INT(BADD/256)
1760 OUT DMACH*2+1,LETH-INT(LETH/256)*256
1770 OUT DMACH*2+1,INT(LETH/256)
1780 OUT &H82,PAGE
1790 '----------DMA Transfer---------------
1795 GOSUB 2700
1800 K=K+1
1810 PRINT:PRINT
1820 DMACH%=DMACH
1830 DEF SEG=&H1700
1840 DMAT=&H0
1850 CALL DMAT(DMACH%,CYC%)
1860 OUT &H110,&H0
1870 OUT &H107,&HF
1875 GOSUB 2700
1880 GOTO 1960
1890 SEGM=PAGE*4096+INT(BADD/16)
1900 DEF SEG=SEGM
1910 FOR I=0 TO 200
1920 PA2=PEEK(I*2)\16+PEEK(1+I*2)*16
1930 IF PA2)2047 THEN PA2=PA2-4096
1940 PRINT PA2,
```

```
1950 NEXT I
1960 RETURN
2250 REM ------- Saving Data in Floppy Disc ---------------
2260 DEF SEG =&H2000
2270 LOCATE 17,1o:PRINT  KL:"Times of Data Savings"
2280 SOUND 2o1,8
2290  ON KL GOTO 2300,2310,2320,2330,2340 ,2350
2300  BSAVE "C:D$1",0,LETH :GOTO 23o0
2310  BSAVE "C:D$2",0,LETH:GOTO 23o0
2320  BSAVE "C:D$3",0,LETH:GOTO 23o0
2330  BSAVE "C:D$4",0,LETH:GOTO 23o0
2340  BSAVE "C:D$5",0,LETH:GOTO 23o0
2350 BSAVE"C:D$6",0,LETH
2360 BEEP
2370 RETURN
2371 LET AO=4:ADCHO=5:LETHO=&OOOO!:CXCO=1o0
2372 INPUT "G.V.O. OF THE TEST CONDITION [KA%] ?":KA
2373 PRINT "Does Cavitation occur[y/n] ?"
2374 X$=INPUT$(1)
2375 IF X$="Y" OR X$="y" THEN A$="CAVITATION"  :GOTO 2377
2376 A$="No Cavitation":B$="NO":C$="NO":SP=0:GOTO  23oe
2377 PRINT "Central Cavitation Core [c] or Spiral Cavitation Rope [s] ?"
2378 Y$=INPUT$(1)
2379 IF X$="C" OR Y$="c" THEN B$="Central Core" ELSE B$="Central Core"
2380 IF X$="S" OR X$="s" THEN B$="Spiral"
2381 IF P$="Central Core" THEN C$="NO" :GOTO 238e
2382 PRINT "Direction of Draft-tube Vortex Rotation [+/-] ?"
2383 X$=INPUT$(1)
2384 IF X$="+" THEN C$="Clockwise"  ELSE B$="Counterclockwise"
2385 INPUT "Ratational Speed  of Draft-tube Vortex [rpm]?";SP
2386 INPUT "TOTAL SAMPLING TIMES OF LOW-FREQUENCY SAMPLING":LFO
2387 INPUT "TOTAL SAMPLING TIMES OF HIGH-FREQUENCY SAMPLING":LF1
2388 OPEN "c:data" FOR APPEND AS#1
2390 WRITE #1,A$,KA,B$,C$,SP,AO,LETHO,ADCHO,CXCO,LFO,LF1
2395 WRITE #1,DC(0),DC(1),DC(2),DC(3),T1$,D1$
2590 WRITE #1,D8(0),D8(1),D8(2),D8(3),T2$,D2$,LETH,CHN01,ADCH2,CXC
2600 CLOSE #1
2620 GOTO 1o2
2700 DML=DMACH*2:DMH=DMACH*2+1
2710 A=INP(8):BL=INP(DML):BH=INP(DML):CL=INP(DMH):CH=INP(DMH)
2720 RETURN
2800 OUT &H114,CHN01
2810 OUT &H110,&H78
2820 OUT &H103,&H14
2830 OUT &H103,&H50
2840 OUT &H100,&H20
2850 OUT &H103,&H14
2860 GOTO 1o90
```

C. **Programs for Frequency Response of HL-160-25 Hydraulic Turbine System**

Frequency Scan

```
      IMPLICIT COMPLEX(Z)
      DIMENSION PZ(3),AL(14),D(14)
      COMMON/AA/ AL,D,FN,Q
      AL(1)=4.65
      AL(2)=2.28
      AL(3)=1.445
      AL(4)=1.725
      AL(5)=1.1
      AL(6)=2.16
      AL(7)=2.3+0.785
      AL(8)=0.4
      AL(9)=1.27+0.785
      AL(10)=5.7
      AL(11)=5.7
      AL(12)=0.5
      AL(13)=0.562
      AL(14)=0.562
      D(1)=0.6
      D(2)=0.4
      D(3)=0.4
      D(4)=0.4
      D(5)=0.4
      D(6)=0.4
      D(7)=0.5
      D(8)=0.5
      D(9)=0.5
      D(10)=1.0
      D(11)=0.4
      D(12)=SQRT(0.1068/0.7854)
      D(13)=SQRT(0.1449/0.7854)
      D(14)=SQRT(0.2036/0.7854)
      FN=0.018

      Q=0.15
      ZS=CMPLX(0.,0.)

      WRITE(*,3)
3     FORMAT(1X,          SIGM          OMG          ABS(Z
     *  D)  )
      K=1
      KL=0
      DO 100 I=1,3
      ZS=ZS+(0.,5.)
      CALL ZD14(ZS,ZD)
      PZ(K)=CABS(ZD)
      K=K+1
100   CONTINUE
```

```
170     IF(PZ(2).LT.PZ(1).AND.PZ(2).LT.PZ(3)) GOTO 150
        IF(PZ(2).GT.PZ(1).AND.PZ(2).GT.PZ(3)) GOTO 150
160     PZ(1)=PZ(2)
        PZ(2)=PZ(3)
        ZS=ZS+(0.,5.)
        CALL ZD14(ZS,ZD)
        PZ(3)=CABS(ZD)
        GOTO 170
150     KL=KL+1
        ZS2=ZS-(0.,5.)
        WRITE(*,'(2F20.10,F20.6)') ZS2,PZ(2)
        IF(KL.GE.10) GOTO 180
        GOTO 160
180     STOP
        END

        SUBROUTINE ZD14(ZS,ZD)
        IMPLICIT COMPLEX(Z)
        DIMENSION AL(14),D(14)
        COMMON/AA/ AL,D,FN,Q
        SAVE /AA/
        HA=11.
        VA=8.64
        ZU1=-1.2*HA/(VA*ZS)
        CALL ZDU(ZU1,AL(1),D(1),FN,Q,ZS,ZD1)
        VR1=53.9
        CALL ZUDA(ZS,ZD1,VR1,ZU2)
        CALL ZDU(ZU2,AL(2),D(2),FN,Q,ZS,ZD2)
        V=Q/(0.7854*0.4*0.4)
        HO=0.07*V*V/(2.*9.81)
        ZU3=ZD2-CMPLX(2.*HO/Q,0.)
        CALL ZDU(ZU3,AL(3),D(3),FN,Q,ZS,ZD3)
        PM=0.176
        ZU4=ZD3+CMPLX(PM,0.)
        CALL ZDU(ZU4,AL(4),D(4),FN,Q,ZS,ZD4)
        ZU5=ZD4-CMPLX(2.*HO/Q,0.)
        CALL ZDU(ZU5,AL(5),D(5),FN,Q,ZS,ZD5)
        H1=2.5*V*V/(2.*9.81)
        ZU6=ZD5-2.*H1/Q
        CALL ZDU(ZU6,AL(6),D(6),FN,Q,ZS,ZD6)
        VR2=53.9
        CALL ZUDA(ZS,ZD6,VR2,ZU7)
        CALL ZDU(ZU7,AL(7),D(7),FN,Q,ZS,ZD7)
        ZU8=ZD7
        CALL ZDU(ZU8,AL(8),D(8),FN,Q,ZS,ZD8)
        ZU9=ZD8
        CALL ZDU(ZU9,AL(9),D(9),FN,Q,ZS,ZD9)
        VR3=9.66
        CALL ZUDA(ZS,ZD9,VR3,ZU10)
        CALL ZDU(ZU10,AL(10),D(10),FN,Q,ZS,ZD10)
        ZU11=ZD10
        CALL ZDU(ZU11,AL(11),D(11),FN,Q,ZS,ZD11)
```

```
TM=20.
ZU12=ZD11-TM
CALL ZDU(ZU12,AL(12),D(12),FN,Q,ZS,ZD12)
CALL ZDU(ZD12,AL(13),D(13),FN,Q,ZS,ZD13)
CALL ZDU(ZD13,AL(14),D(14),FN,Q,ZS,ZD14)
ZD=ZD14
RETURN
END

SUBROUTINE ZDU(ZU,AL,D,F,Q,ZS,ZD)
IMPLICIT COMPLEX(Z),REAL(L)
AF=0.7854*D*D
A1=2.02E9/998.26
A2=2.02E9/(19.6E10*1.5E-2)
A=SQRT(A1/(1.+A2*D))
C=9.81*AF/(A*A)
L=1./(9.81*AF)
R=F*U/(9.81*D*AF*AF)
ZGAM=CSQRT(ZS*CMPLX(C,0.)*(CMPLX(L,0.)*ZS+CMPLX(R,0.)))
ZC=ZGAM/(CMPLX(C,0.)*ZS)
ZEXP=CEXP(ZGAM*CMPLX(AL,0.))
ZTH=(ZEXP-CMPLX(1.,0.)/ZEXP)/(ZEXP+CMPLX(1.,0.)/ZEXP)
ZD=(ZU-ZC*ZTH)/(CMPLX(1.,0.)-ZU*ZTH/ZC)
RETURN
END

SUBROUTINE ZUDA(ZS,ZD,V,ZU)
IMPLICIT COMPLEX(Z)
ZA=CMPLX(-2.02E9,0.)/(CMPLX(9800.,0.)*CMPLX(V,0.)*ZS)
ZU=ZD*ZA/(ZD+ZA)
RETURN
END
```

Newton Iteration and Mode Shape

```
      IMPLICIT COMPLEX(Z)
      DIMENSION ZF(2),AL(14),D(14),ZU(14),ZD(14)
      DIMENSION ZC(20),ZCH(20),ZSH(20)
      DIMENSION ZHU(20),ZDU(20),ZHD(20),ZDD(20)
      DIMENSION NJ(20)
      COMMON/AA/ AL,D,FN,Q
      AL(1)=4.83
      AL(2)=2.26
      AL(3)=1.445
      AL(4)=1.725
      AL(5)=1.1
      AL(6)=2.16
      AL(7)=3.3+0.985
      AL(8)=0.4
      AL(9)=1.27+0.985
      AL(10)=5.3
      AL(11)=3.9
      AL(12)=0.5
      AL(13)=0.562
      AL(14)=0.562
      D(1)=0.8
      D(2)=0.4
      D(3)=0.4
      D(4)=0.4
      D(5)=0.4
      D(6)=1.4
      D(7)=0.5
      D(8)=0.3
      D(9)=1.5
      D(10)=1.0
      D(11)=0.4
      D(12)=SQRT(0.1068/0.7854)
      D(13)=SQRT(0.1449/0.7854)
      D(14)=SQRT(0.2036/0.7854)
      FN=0.018

      Q=0.15
      SIG=-1.01
      OM=80.
      DS=0.01
      DOM=0.01

      ZS=CMPLX(SIG,OM)
      ZEP=CMPLX(DS,DOM)
```

```
      N=0
      TOM=20.
      NIT=15
      TOL=0.0008
      WRITE(*,4) N,ZS
4     FORMAT(1H0, N   IMPEDANCE AT S   IMPED AT S+EPS   CORRECTION TO
     2 S   COMPLEX FREQUENCY'/(I3,3X,F9.4,F9.4)
      KFIN=0
29    K=1
30    CALL ZD1(ZS,ZU,ZD,ZC,ZCH,ZSH,FM,FM,HM,TM)
      ZF(K)=ZD(14)
      IF(KFIN.EQ.1) GOTO 70
      IF(K.EQ.2) GOTO 40
      K=2
      ZSS=ZS
      ZS=ZS+ZEP
      GOTO 30
40    ZDS=-ZEP*ZF(1)   ZF(2)-ZF(1))
      ZS=ZSS+ZDS
      N=N+1
      WRITE(*,5) N,ZF(1),ZF(2),ZDS,ZS
5     FORMAT(I2,4F9.2,4F9.2)
      IF(AIMAG(ZDS).GT.TOM) WRITE(*,7)
7     FORMAT(' CORRECTION TO OMEGA IS EXCESSIVE ')
      IF(N.GT.NIT) WRITE(*,8) N
8     FORMAT(' SOLUTION DID NOT CONVERGE TO ROOT IN',I3, ITERATIONS')
      IF(CABS(ZF(1)).GT.TOL) GOTO 29
      KFIN=1
      GOTO 29
70    HDJJ=1.0
      ZHU(12)=CMPLX(HDJJ,0.)
      ZQU(12)=ZHU(12)*ZU(12)
      DO 100 I=13,14
      ZQU(I)=-ZHU(I-1)*ZSH(I-1)/ZC(I-1)+ZQU(I-1)*ZCH(I-1)
      ZHU(I)=ZQU(I)*ZU(I)
100   CONTINUE
      ZHD(11)=ZHU(12)+TM*ZQU(12)
      ZQD(11)=ZQU(12)
      DO 200 I=1,2
      J=12-I
      ZQU(J)=ZHD(J)*ZSH(J)/ZC(J)+ZQD(J)*ZCH(J)
      ZHU(J)=ZQU(J)*ZU(J)
      ZHD(J-1)=ZHU(J)
      ZQD(J-1)=ZQU(J)
200   CONTINUE
      ZHD(9)=ZHU(10)
      ZQD(9)=ZHD(9)/ZD(9)
      DO 300 I=1,3
      J=10-I
      ZQU(J)=ZHD(J)*ZSH(J)/ZC(J)+ZQD(J)*ZCH(J)
      ZHU(J)=ZQU(J)*ZU(J)
      ZHD(J-1)=ZHU(J)
      ZQD(J-1)=ZQU(J)
300   CONTINUE
```

```
      ZHD(6)=ZHU(7)
      ZOD(6)=ZHD(6)/ZD(6)
      ZOU(6)=ZHD(6)*ZSH(6)/ZC(6)+ZOD(6)*ZCH(6)
      ZHU(6)=ZOU(6)*ZU(6)
      ZZ1=ZOU(6)*PM
      ZHD(5)=ZHU(6)+ZZ1
      ZOD(5)=ZOU(6)
      ZOU(5)=ZHD(5)*ZSH(5)/ZC(5)+ZOD(5)*ZCH(5)
      ZHU(5)=ZOU(5)*ZU(5)
      ZZ2=ZOU(5)*PM
      ZHD(4)=ZHU(5)+ZZ2
      ZOD(4)=ZHD(4)/ZD(4)
      ZOU(4)=ZHD(4)*ZSH(4)/ZC(4)+ZOD(4)*ZCH(4)
      ZHU(4)=ZOU(4)*ZU(4)
      ZZ3=PM*ZOU(4)
      ZHD(3)=ZHU(4)-ZZ3
      ZOD(3)=ZOU(4)
      ZOU(3)=ZHD(3)*ZSH(3)/ZC(3)+ZOD(3)*ZCH(3)
      ZHU(3)=ZOU(3)*ZU(3)
      ZZ4=PM*ZOU(3)
      ZHD(2)=ZHU(3)+ZZ4
      ZOD(2)=ZOU(3)
      DO 500 I=1,2
      J=3-I
      ZOU(J)=ZHD(J)*ZSH(J)/ZC(J)+ZOD(J)*ZCH(J)
      ZHU(J)=ZOU(J)*ZU(J)
      IF(J.EQ.1) GOTO 500
      ZHD(J-1)=ZHU(J)
      ZOD(J-1)=ZHD(J-1)/ZD(J-1)
500   CONTINUE

      DO 110 I=1,14
      NJ(I)=AL(I)/1.0+1
110   CONTINUE

      WRITE(*,9)
9     FORMAT(1H0,    PIPE      X      HEAD     PHIH        Q      PHIQ
     :     ABSZ
      DX=1.0
      DO 120 J=1,14
      ZEXP=ZCH(J)+ZSH(J)
      ZGAM=CLOG(ZEXP)/AL(J)
      N1=NJ(J)
      X=-DX
      DO 120 I=1,N1
      X=X+DX
      ZEXP=CEXP(ZGAM*X)
      ZCHX=0.5*(ZEXP+1./ZEXP)
      ZSHX=0.5*(ZEXP-1./ZEXP)
      ZH=ZHU(J)*ZCHX-ZOU(J)*ZC(J)*ZSHX
      ZQ=-ZHU(J)*ZSHX/ZC(J)+ZOU(J)*ZCHX
      ZZ=ZH/ZQ
      QU=CABS(ZQ)
      HU=CABS(ZH)
      ABSZ=CABS(ZZ)
      PHIQ=ATAN2(AIMAG(ZQ),REAL(ZQ))
      IF(CABS(ZH).EQ.0.) GOTO 120
      PHIH=ATAN2(AIMAG(ZH),REAL(ZH))
120   WRITE(*, '(I5,F9.2,4F9.3,F9.1)')J,X,HU,PHIH,QU,PHIQ,ABSZ
      STOP
      END
```

```
      SUBROUTINE ZD1(ZS,ZU,ZD,ZC,ZCH,ZSH,PM,FM,HM,TM)
      IMPLICIT COMPLEX(Z)
      DIMENSION AL(14),D(14),ZU(14),ZD(14),ZC(14)
      DIMENSION ZCH(20),ZSH(20)
      COMMON/AA/ AL,D,FN,0
      SAVE /AA/
      HA=11.
      VA=0.64
      ZU(1)=-1.2*HA*(VA*ZS)
      CALL ZDU(ZU(1),AL(1),D(1),FN,0,ZS,ZD(1),ZC(1),ZCH(1),ZSH(1))
      VR1=55.9
      CALL ZUDA(ZS,ZD(1),VR1,ZU(2))
      CALL ZDU(ZU(2),AL(2),D(2),FN,0,ZS,ZD(2),ZC(2),ZCH(2),ZSH(2))
      V=0./(0.7854*1.4*0.4)
      H=0.07*V*V/(2.*9.81)
      FM=2.*H0.0
      ZU(3)=ZD(2)-CMPLX(FM,0.)
      CALL ZDU(ZU(3),AL(3),D(3),FN,0,ZS,ZD(3),ZC(3),ZCH(3),ZSH(3))
      HM=0.176
      ZU(4)=ZD(3)+CMPLX(FM,0.)
      CALL ZDU(ZU(4),AL(4),D(4),FN,0,ZS,ZD(4),ZC(4),ZCH(4),ZSH(4))
      ZU(5)=ZD(4)-CMPLX(FM,0.)
      CALL ZDU(ZU(5),AL(5),D(5),FN,0,ZS,ZD(5),ZC(5),ZCH(5),ZSH(5))
      H1=2.5*V*V/(2.*9.81)
      HM=2.*H1/0
      ZU(6)=ZD(5)-CMPLX(HM,0.)
      CALL ZDU(ZU(6),AL(6),D(6),FN,0,ZS,ZD(6),ZC(6),ZCH(6),ZSH(6))
      VR2=53.6
      CALL ZUDA(ZS,ZD(6),VR2,ZU(7))
      CALL ZDU(ZU(7),AL(7),D(7),FN,0,ZS,ZD(7),ZC(7),ZCH(7),ZSH(7))
      ZU(8)=ZD(7)
      CALL ZDU(ZU(8),AL(8),D(8),FN,0,ZS,ZD(8),ZC(8),ZCH(8),ZSH(8))
      ZU(9)=ZD(8)
      CALL ZDU(ZU(9),AL(9),D(9),FN,0,ZS,ZD(9),ZC(9),ZCH(9),ZSH(9))
      VR3=7.6*
      CALL ZUDA(ZS,ZD(9),VR3,ZU(10))
      CALL ZDU(ZU(10),AL(10),D(10),FN,0,ZS,ZD(10),ZC(10),ZCH(10),
     & ZSH(10))
      ZU(11)=ZD(10)
      CALL ZDU(ZU(11),AL(11),D(11),FN,0,ZS,ZD(11),ZC(11),ZCH(11),
     & ZSH(11))
      TM=20.
      ZU(12)=ZD(11)-TM
      DO 130 I=12,14
      CALL ZDU(ZU(I),AL(I),D(I),FN,0,ZS,ZD(I),ZC(I),ZCH(I),ZSH(I))
      IF(I.EQ.14) GOTO 130
      ZU(I+1)=ZD(I)
  130 CONTINUE
      RETURN
      END

      SUBROUTINE ZDU(ZU,AL,D,F,0,ZS,ZD,ZC,ZCH,ZSH)
      IMPLICIT COMPLEX(Z),REAL(L)
      AF=0.7854*D*D
      A1=2.02E9/998.26
      A2=2.02E9/(19.6E10*1.5E-2)
      A=SQRT(A1/(1.+A2*D))
      C=9.81*AF/(A*A)
      L=1./(9.81*AF)
```

```
R=F*D/(9.81*D*AF*AF)
ZGAM=CSQRT(ZS*CMPLX(C,0.)*(CMPLX(L,0.)*ZS+CMPLX(R,0.)))
ZC=ZGAM/(CMPLX(C,0.)*ZS)
ZEXP=CEXP(ZGAM*CMPLX(AL,0.))
ZCH=0.5*(ZEXP+1./ZEXP)
ZSH=0.5*(ZEXP-1./ZEXP)
ZTH=(ZEXP-CMPLX(1.,0.)/ZEXP)/(ZEXP+CMPLX(1.,0.)/ZEXP)
ZD=(ZU-ZC*ZTH)/(CMPLX(1.,0.)-ZU*ZTH/ZC)
RETURN
END

SUBROUTINE ZUDA(ZS,ZD,V,ZU)
IMPLICIT COMPLEX(Z)
ZA=CMPLX(-2.02E9,0.)/(CMPLX(9800.,0.)*CMPLX(V,0.)+ZS)
ZU=ZD*ZA/(ZD+ZA)
RETURN
END
```

D. **Relevant Paper (I. Mech. Engrs. 1986)**

PUBLISHED
PAPERS
TO THE END
NOT
FILMED
FOR
COPYRIGHT
REASONS